Centro de Investigación Científica y de Educación Superior de Ensenada, Baja California

Doctorado en Ciencias
en Óptica con orientación en Óptica física

Transformaciones conformes en fotónica de silicio

Tesis

para cubrir parcialmente los requisitos necesarios para obtener el grado de

Doctor en Ciencias

Presenta:

Verónica Pérez Chávez

Ensenada, Baja California, México

2017

Tesis defendida por

Verónica Pérez Chávez

y aprobada por el siguiente Comité

Dr. Eugenio Rafael Méndez Méndez

Co-director de tesis

Dr. Sylvain Blaize

Co-director de tesis

Dr. Heriberto Márquez Becerra

Dr. Anatoly Khomenko

Dr. Rafael Salas Montiel

Dr. Alexei A. Maradudin

Dr. Pedro Negrete Regagnon

Coordinador del Programa de Posgrado en Óptica

Dra. Rufina Hernández Martínez

Director de Estudios de Posgrado

Resumen de la tesis que presenta Verónica Pérez Chávez como requisito parcial para la obtención del grado de Doctor en Ciencias en Óptica.

Transformaciones conformes en fotónica de silicio

Resumen aprobado por:

Dr. Eugenio Rafael Méndez Méndez	Dr. Sylvain Blaize
Co-director de Tesis	Co-director de Tesis

En este trabajo, se presenta una revisión de la literatura sobre las aplicaciones de la óptica de transformaciones en fotónica de silicio, basadas en el control del índice de refracción efectivo a través de la densidad de nano-pilares de silicio. Después de ilustrar el potencial del método con el diseño de un elemento acoplador, presentamos un estudio teórico y experimental de la respuesta óptica de nano-pilares de silicio a longitudes de onda de telecomunicaciones. El objetivo principal de este estudio es probar las teorías de medio efectivo en el contexto de la fotónica de silicio. Muestras con densidades fijas y variables de pilares de silicio fueron fabricadas para este proyecto y se realizaron mediciones de su reflectividad a una longitud de onda de 1550 *nm*.

Se presentan también cálculos de la reflectividad de muestras con nano-pilares utilizando dos método numéricos rigurosos: un método basado en la ecuación reducida de Rayleigh y el método modal de Fourier llamado de análisis riguroso de modos acoplados (RCWA, por sus siglas en inglés). El método de Rayleigh tiene limitaciones en lo que respecta a las alturas superficiales que es posible considerar con él, pero tiene la ventaja de ser rápido y poco demandante computacionalmente. Por otro lado, el RCWA requiere un poder de cómputo mucho mayor, pero es más apropiado para cálculos que involucran estructuras con pendientes pronunciadas y no sufre de las limitaciones del método de Rayleigh.

Utilizando diferentes teorías de medio efectivo, se estimó el índice de refracción efectivo de la región nanoestructurada de silicio de nuestras muestras y, con base en un modelo de capa homogénea, se estimaron las reflectividades correspondientes y se compararon con las estimaciones experimentales y teóricas. Estos resultados sirvieron de base para probar la validez de las teorías de medio efectivo en el caso particular de las muestras fabricadas. Los resultados muestran que las teorías de medio efectivo consideradas, junto con el modelo de capa homogénea, no resultan adecuadas para calcular la reflectividad de las muestras estudiadas. Por otro lado, los dos métodos numéricos rigurosos producen resultados que concuerdan entre sí y también tienen un buen acuerdo con los resultados experimentales.

Palabras Clave: **fotónica de silicio, teoría de medio efectivo, óptica de transformaciones, dieléctricos de alto índice, esparcimiento de luz.**

Abstract of the thesis presented by Verónica Pérez Chávez as a partial requirement to obtain the PhD in Optics.

Conformal transformations in silicon photonics

Abstract approved by:

Dr. Eugenio Rafael Méndez Méndez	Dr. Sylvain Blaize
Thesis Co-director	Thesis Co-director

In this work, we present a literature review of the applications of transformation optics in silicon photonics, on the basis of the control of the effective refractive index through the density of silicon nano-pillars. After illustrating the potential of the method with the design of a coupling element, we present an experimental and theoretical study of the optical response of silicon nano-pillars at telecommunication wavelengths. The main objective of the study is to test effective medium theories in the context of silicon photonics. Samples with fixed and variable pillar densities were fabricated for this project and their reflectivities were measured for a 1550 *nm*-wavelength.

We also present calculations of the reflectivity of samples with nano-pillars employing two rigorous numerical methods: a method based on the reduced Rayleigh equation and a Fourier modal method, called the rigorous coupled wave analysis (RCWA). The Rayleigh method has limitations with respect to the surface heights that can be considered, but has the advantage of being fast and not very demanding computationally. On the other hand, the RCWA is much more demanding in computer power, but is more appropriate for calculations involving structures with large slopes and does not suffer from the limitations of the Rayleigh method.

Employing different effective medium theories, we have estimated the effective refractive index of the nanostructured silicon region of our samples and, based on a homogeneous layer model, we have estimated the corresponding reflectivities and compared them with the experimental and theoretical estimations. These results were used to test the validity of the effective medium theories in the particular case of the fabricated samples. The results show that the effective medium theories considered, together with the homogeneous layer model, are not adequate to calculate the reflectivity of the studied samples. On the other hand, the two numerical methods produce results that are in good agreement with each other and with the experimental results.

Keywords: **silicon photonics, effective medium theory, transformation optics, high index dielectrics, light scattering.**

Dedication

In loving memory of my dad.

Aknowledgments

To my advisors Eugenio Méndez and Sylvain Blaize for always supporting me, specially during the though times, and showing me the right path.

To Heriberto Marquez, Anatoly Khomenko and Rafael Salas, members of my thesis committee, for their advice during the realization of this thesis.

To Alex A. Maradudin, for his example as a great scientist and human being, for the shared laughs, for always caring.

To Ingve Simonsen, my love, my partner, my friend.

To the administrative staff: Rosario, Olguita, Mary Carmen, Cruz and Marla, for cheering me, for always being there to help with a smile.

To my dear friends at CICESE: Fabian, Raúl, Santiago, Patricia and Liliana, you all mean so much to me.

To José Julio Santibanez, for believing in me, and helping me during my worst moments.

To my friends and family for their unconditional love.

And last but not least, to my daughter Betsy, for being by my side at every step of this work, and for being my daily inspiration and source of strength. I love you so much my pretty one!

To the Centro de Investigación Científica y de Educación Superior de Ensenada.

To the Consejo Nacional de Ciencia y Tecnología (CONACyT) for giving me the economic support to carry out my
PhD studies.

Table of contents

List of figures

List of tables

Chapter 1 Introduction

Transformation optics is an emerging area of optics in which electromagnetically equivalent structures can be found by means of a change in their geometry. Some of the recent proposals in this field have attracted wide attention. Among them, we can mention: design of invisibility or cloaking devices (Pendry *et al.*, 2006; Li and Pendry, 2008; Leonhardt and Philbin, 2010), the fabrication of structures for light focusing (Aubry *et al.*, 2010; Rahm *et al.*, 2008), and the search for structures for field enhancements (Glass *et al.*, 1983).

A particularly interesting approach, due to the simplicity of its consequences in electromagnetic calculations, is based on conformal mappings. Conformal mappings are techniques developed for transformations in the complex plane and they are, essentially, of a two-dimensional nature. The name is due to the fact that, locally, they preserve angles.

The use of conformal mappings in problems of scattering has been a subject of study for several years. Such techniques have been used for some time in calculations for diffraction gratings (Nevière *et al.*, 1973; Depine and Simón, 1982). This kind of transformation can be regarded as a transformation to a space of curvilinear coordinates that is equivalent to modifying the refractive index of the medium in which the electromagnetic wave propagates. The change in the geometry results in an anisotropic medium with refractive index variations.

Let us assume that the problem we are dealing with depends on two Cartesian coordinates (x, y), but is independent of a third one that we call ζ. For harmonic fields the complex amplitude $\varphi(x, y)$ obeys the Helmholtz equation

$$\nabla^2\varphi(x, y) \pm k^2\varphi(x, y) = 0, \tag{1}$$

where the wavenumber $k=\sqrt{\varepsilon\mu}\frac{\omega}{c}$. Here, ε and μ represent the electric permittivity and the magnetic permeability of the medium, ω is the angular frequency, c is the speed of light in vacuum, and $n_z = \sqrt{\epsilon\mu}$ is the refractive index. Depending on the sign that we choose, and on the value of k^2, this equation can also represent the Laplace equation or the diffusion equation (Born and Wolf, 1970).

Consider the conformal transformation $w = f(z)$ that takes points $z = x + iy$ from the complex plane Z to points $w = u + iv$ in the complex plane W. As we show in Chapt. 2, the Helmholtz Equation (1) can be written in the transformed space as

$$\nabla^2\varphi(u,v) + K^2\varphi(u,v) = 0, \tag{2}$$

where

$$K^2 = h^2k^2 = h^2\varepsilon\mu\left(\frac{\omega}{c}\right)^2. \tag{3}$$

In this equation, h represents the local change of scale of the transformation which, in general, is a function of position in the (u,v) plane. It can be expressed in terms of the transformation as $h = |dz/dw|$. We see that, apart from the changes in the boundaries associated with the transformation, the transformation has modified the refractive index from $\sqrt{\varepsilon\mu}$ to a position dependent refractive index $n_w = hn_z$.

These results illustrate the fact that one can change the geometry or boundaries of a system (perhaps simplifying them) by a suitable conformal mapping, and end up with an electromagnetically equivalent system in which one has introduced additional refractive index variations. It is not surprising, then, that conformal mappings find applications in the design of integrated photonic devices (see, e.g. García-Meca et al., 2011).

Geometry has always played a distinguished role in optics. Electromagnetic devices inspired by conformal mapping, require the implementation of custom geometries through specially designed inhomogeneous materials, which must be precisely controlled on the scale of the wavelength. To date, one of the most commonly used approaches for this is the one based on metamaterials. Metamaterials obtain their properties not only from their composition but also from their structure, and achieve important changes in the optical variables by means of resonances. Several authors have reported the fabrication of metamaterials in the microwave region (Schurig *et al.*, 2006) and in the infrared (Xiaofei *et al.*, 2009). Nonetheless, despite their interesting characteristics, metamaterials cannot yet be well-controlled in the optical range. In this range, due to the difference in the optical properties of materials, the structures are conceptually very different from their counterparts in the microwave region. The intricate designs that are used in microwaves are simply

inappropriate for optical frequencies. Thus, metamaterials are potentially very versatile, but the possibilities are limited by the available natural materials.

In a simple and basic approach to this issue, one can obtain the desired variations in the transformed structures by means of the effective medium theory (EMT), in which the most important feature for the average properties of the medium is the composition of the material. In this theory, the description of an equivalent (composite) medium is based on the properties and the relative fractions of its components. There are many different effective medium approximations, each of them being more or less accurate under distinct conditions. Nevertheless, they all assume that the macroscopic system is homogeneous.

Two EMTs that are especially popular are those developed by Maxwell Garnett (1904) and Bruggeman (1935). The Maxwell Garnett theory applies to mixtures that contain distinguishable inclusions, or grains with dielectric function ϵ embedded in an otherwise homogeneous matrix with a dielectric function ϵ_m, whereas the Bruggeman theory applies to mixtures in which such a distinction is not possible (Choy, 1999).

In accordance with both the Maxwell Garnett (1904) and the Bruggeman (1935) theories, the effective dielectric function of a mixture of two components will depend only on the dielectric functions of both components and their volume fractions. By means of an effective material theory approach, a continuous refractive index map can be translated into a volume fraction and, through a dithering algorithm, into a discretized binary version with features of size smaller than the wavelength (Gabrielli and Lipson, 2011) that can be fabricated in silicon using nano-lithography. Silicon has a high refractive index contrast relative to both air and SiO_2, which allows for a reasonably wide range of achievable effective material parameters.

Integrated optical circuits are devices that contain miniaturized optical elements that perform different photonic functions on a common substrate. Channel waveguides are the fundamental building blocks of optical integrated circuits. These optical waveguides can be made by depositing material on top of a substrate and etching unwanted portions away.

Passive optical elements in photonic circuits include branches, expanders, directional couplers, and filters. Branches are used to divide a beam into two or more channels.

Losses in branches are always significant and, for this reason, directional couplers are often used for this purpose. Expanders are used to change the width of the waveguide, an operation that usually changes the modal characteristics of the guide.

Circuits of integrated optics on a silicon platform constitute an excellent candidate to prove concepts of transformation optics and to orchestrate new devices. This is due to the possibility of having a refractive index that can be directly controlled by the density of nano-metric silicon pillar structures on a slab (Gabrielli and Lipson, 2011). On the other hand, it is also possible to modify the propagation constant in waveguides by changing the dimensions of the guide. Several authors have reported the utilization of transformation optics and nano-structured silicon to fabricate cloaking devices in the optical domain (Gabrielli *et al.*, 2009) and for focusing light in the near infrared (Spadoti *et al.*, 2010).

1.1 Motivation

The purpose of the present project is to explore the possibility of using conformal mapping techniques in silicon photonics. The main idea is to design optical elements and devices with controlled geometries and variations of the refractive index, introduced by means of the use of nano-structured silicon. We are particularly interested in the design of low loss expanders/compressors to couple two optical waveguides of different refractive indices and widths, while maintaining the modal characteristics; this is one of the most important problems in integrated optics.

Beside the possible applications that we have mentioned, there are other aspects that make transformation optics an attractive area of research. We can mention, for example, the analogies with problems in quantum mechanics (Marte and Stenholm, 1997) and the observation of optical Bloch oscillations (Lenz *et al.*, 1999).

In the following subsections we discuss some of these motivations.

1.1.1 Analogies with problems in quantum mechanics

To illustrate the existence of analogies with problems in quantum mechanics, we will now consider the paraxial approximation of the Helmholtz equation. The paraxial approximation is precisely defined by the slow variation envelope condition, which means that the longitudinal variation in the derivative of the modulation function is very small over a distance comparable to the nominal wavelength of the beam. In this approximation we neglect the second term of Eq.(1) to obtain the equation

$$\nabla_T^2 \varphi(x, y, z) + i2k \frac{\partial}{\partial z} \varphi(x, y, z) \approx 0, \tag{4}$$

which is called the paraxial approximation of the wave equation and where

$$\nabla_T^2 = \nabla^2 - \frac{\partial^2}{\partial z^2} = \frac{\partial^2}{\partial x^2} + \frac{\partial^2}{\partial y^2} \tag{5}$$

is the transverse Laplace operator, shown here in Cartesian coordinates. This is also the form of the time dependent Schrodinger equation used in quantum mechanics. In the

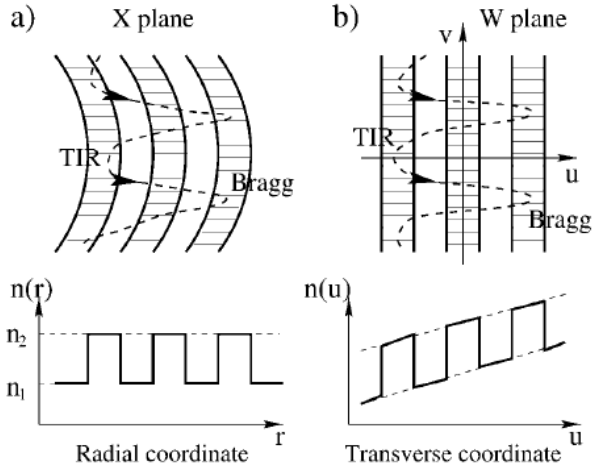

Figure 1: Top: Schematic of (a) a curved waveguide array and (b) its conformal transformation. The dashed arrows illustrate the light confinement mechanisms—Bragg reflection on one side of the structure and total internal reflection on another side. Bottom: (a) Refractive index in the curved array, and (b) the transformed refractive index. The refractive indices of the guides and the surrounding material are n2 and n1, respectively. The Figure was taken from Lentz et al. (1999).

Schrodinger equation the first order derivative is a time derivative.

An interesting application of transformation optics is given by the observation of Bloch oscillations in an array of curved guide waves, an optical approach to a classical problem of solid state physics (Lenz *et al.*, 1999). In the beginning of the last century, Bloch predicted that a charge carrier in an ideal crystal placed in a uniform electric field exhibits periodic oscillations ("Bloch oscillations"). The carrier is accelerated by the electric field until its momentum satisfies the Bragg condition associated with the periodic potential and is reflected. The carrier is then decelerated by the field until it stops, completing one Bloch cycle (Lenz *et al.*, 1999). This periodic motion is related to a periodic potential in a linear ramp.

In the optical approach, imposing a linear variation in the refractive index is challenging. With a structure that consists of an array of periodically spaced, curved optical waveguides (Fig. 1), the curvature can effectively lead to a linear ramp in the refractive index distribution by means of a conformal transformation (Lenz *et al.*, 1999).

1.1.2 Field enhancements in plasmonic systems by means of transformation optics

The search for an electric field enhancement in complex plasmonic geometries, due to the localization of surface plasmon polaritons (SPPs), is another application that has been investigated with a transformation optics approach.

To illustrate the potential of this method, we now consider the example by Luo et al. (2011) in which, by means of transformation optics, they study the interaction of an EM wave with concave and convex surfaces that are shown to exhibit a dramatic increase of the electric field that is also highly localized in the vicinity of their apexes.

In their proposal, they present a system of periodic metallic slabs excited by a line dipole array, such as the ones shown in the panels (a_1) and (a_2) of Fig.2. Using the transformation

$$w = \frac{a}{exp\{2\pi z/d\} - 1} + \frac{a}{2}, \tag{6}$$

with d corresponding to the period between slabs, this structure is mapped into the profile illustrated in panels (b_1) and (b_2) of this figure. Thus, in the transformed space, we have a concave structure with a diameter a, engraved onto a planar metal surface, where the line dipole is mapped into a uniform electric field (panel b_1). Depending on the parameters, convex structures embedded in a metal surface can also be obtained (panel b_2).

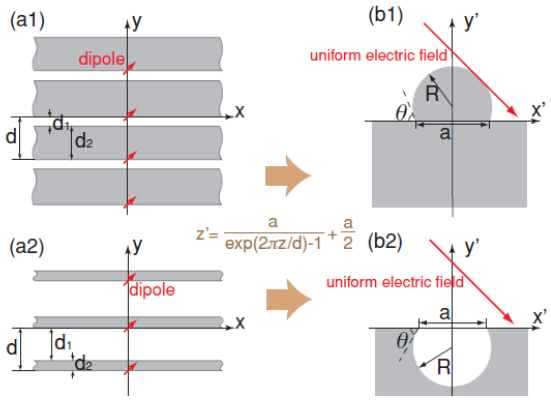

Figure 2: The schematic of transformation. (a1) and (a2) Periodic metallic slabs excited by a line dipole array, transporting SPPs to $x \to \pm\infty$. The thicknesses of each dielectric media and metallic slab are d_1 and d_2, respectively. In (a1) $d_1 < d_2$, while in (a2) $d_1 > d_2$. Under a conformal transformation described by Eq.(6), the convex (b1) and concave (b2) rough surfaces are obtained, and the line dipole array in (a1)/(a2) is mapped to a uniform electric field Einc in (b1)/(b2). The Figure was taken from Luo et al. (2011).

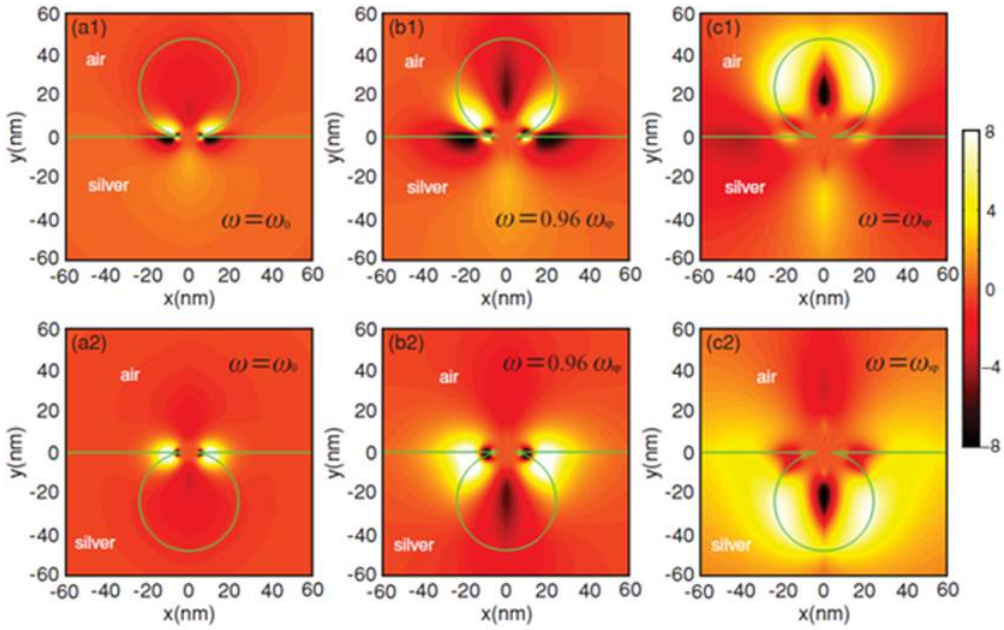

Figure 3: Electrical field in the transformed space. The Figure was taken from Luo et al. (2011).

By means of a conformal mapping approach, an analytic relationship has been established between both structures. The EM problem of finding the frequencies that lead to the resonances of the system is easier to deal with in the Z space. The critical surface plasmon frequency for which we have a dramatic increase of the electric field is found in this space, but geometrically at a value of x that tends to infinity.

The electrical near field behavior in the transformed space is illustrated in Fig. 3. From this Figure, we can see that the increase of the electric field is highly localized in the vicinities of the apexes for the same critical surface plasmon frequency calculated in the original space.

1.2 Objectives

The main objective of this thesis is to explore the design and fabrication of optical elements for integrated optics based on conformal transformations and nanostructured silicon. A central issue here is how a structure with the prescribed refractive index variations can be fabricated using nanostructured silicon.

Our strategy, then, included activities on the following aspects of the problem:

- The design of optical elements for integrated optics using conformal mapping techniques.

- The fabrication of nanostructured silicon samples by means of e-beam lithography and reactive ion etching.

- The implementation of a dithering algorithm to discretize a continuously varying function (volume density of silicon) into a binary map.

- The evaluation of the accuracy of effective medium theories through experiments with the fabricated samples.

- The development of computer codes for electromagnetic calculations for testing EMTs and comparisons with experimental results.

These studies are described in the following Chapters.

1.3 Thesis structure

The thesis is structured as follows:

In Chapter 2, we briefly outline the general properties of conformal mappings and their consequences in electromagnetic calculations. Particularly important are the consequences of the transformation on the differential operators, which lead to important changes in the optical properties. Some examples that illustrate the potential of conformal transformations in optics are also presented.

Chapter 3 contains a review of silicon photonics (SP), as well as a literature review on the design of photonic devices on the basis of effective medium and transformation optics. As an example of the capabilities and limitations of conformal mapping transformations in silicon photonics, we present the design of a compressor/expander to couple glass and silicon waveguides. We are particularly interested in low loss compressor/expanders that maintain the modal characteristics.

In Chapter 4 we present a brief review of the effective medium theories that were used in our comparison with the experimental results. The tests carried out to find an adequate procedure for the fabrication of the nanostructured silicon samples of interest are presented in Chapter 5. We also describe the reflectivity measurements carried out with the fabricated samples.

Chapter 6 is devoted to the theoretical approaches considered to test the EMT. These are a method based on the reduce Rayleigh equation (RRE), and a Fourier modal method. The developed computer codes are used to calculate the reflectivity of the samples and these results are compared with both, the experimentally obtained values and the values predicted by different EMTs. The results are presented in Chapter 7, together with a discussion and, finally, in Chapter 8 we present the conclusions reached in this thesis.

Chapter 2 Transformations in optics and conformal mappings

It is our aim in this Chapter to present the general properties of conformal mappings. As we have mentioned, the change in the Helmholtz equation after a conformal transformation can be interpreted as a modification in the refractive index of the medium. This allows us to link both, the structural properties of surfaces and waveguides with equivalent problems in which the structure and the optical properties change. Examples of some basic conformal transformations are presented, and the limitations of the method discussed.

2.1 Historical context

The history of conformal mappings is usually traced back to the stereographic projection used in ancient times, and to the projection ideas of Mercator developed in the sixteenth century; both are early examples of conformal or angle-preserving projections (Heine, 2004).

The stereographic projection, or planisphere, may have been known in ancient Egypt (Heine, 2004). Ptolemy's Planisphaerum describes its use, but in astronomy, not geography; in fact this projection seems to have been used exclusively for star charts until the Renaissance. During the 16th century, the stereographic function began to be widely used and popular for geographic maps or map projections (Porter, 2005). These were the first attempts to portray the surface of the earth, or a portion of the earth, on a flat surface. A map projection is conformal if the angles in the original features are preserved in the image on the chart. Over small areas, the shapes of objects will be preserved. Consistent with Ptolemy's projection, Mercator developed his conformal projection in 1569 as an aid to navigation (Heine, 2004).

Some time later, in 1772, Lambert published an original work that has been considered as the foundation of modern mathematical cartography (Porter, 2005). Lagrange gives Lambert credit as the first to characterize the problem of mapping from a sphere to a

plane, in terms of nonlinear partial differential equations. The technique was very fruitful, for he invented several whole families of conformal projections, some of which are still in widespread use today. It was on the basis of this technique that Lagrange combined a pair of differential equations of two real variables in a complex equation of a single variable. These results were later on completed by Gauss (1822), who generalized the theorem of Lagrange to a conformal mapping of an arbitrary surface on the plane.

Many classical applications of conformal mapping deal with the solution of Laplace's equation, which remains invariant if the original plane is subject to a conformal transformation. As a result, this kind of transformation can be effectively used for constructing solutions to the Laplace equation on complicated planar domains that appear in a wide range of physical problems, including fluid mechanics,thermomechanics, and electrostatics.

Conformal mapping has many successful applications in modern technology. These involve not only new transformation algorithms, but the use of classical methods in new technologies. In particular, we will direct our efforts towards the use of this kind of transformations in silicon photonics, which is the study and application of photonic systems that use silicon as an optical medium. These operate in the infrared, commonly at the 1.55 micrometer wavelength used by most fiber optic telecommunication systems.

Other new applications of conformal maps include a wide range of problems in waveguide analysis. We can mention, for example, the seminal contribution of Meinke (Meinke *et al.*, 1963), which involves trading boundary shapes for uniformity of the medium, followed by the original work on anisotropic media by several authors (Leonhardt, 2006; Gabrielli and Lipson, 2011).

2.2 Theory

Usually, a conformal mapping acts in the domain of the complex plane and is a powerful analysis tool that uses complex valued functions depending on a single variable to transform complicated borders into simpler ones, so that the basic equation of the problem can be resolved in the new space.

We will consider a complex function $f(z)$ that can be uniquely written as the complex combination of two real functions $f(z) = f(x + iy) = u(x, y) + iv(x, y)$, each depending on the two real variables x, y: its real part $u(x, y) = \mathrm{Re}\, f(z)$, and its imaginary part $v(x, y) = \mathrm{Im}\, f(z)$.

A series of points in the complex plane Z will be mapped by $f(z)$ to a series of points in the transformed plane W. The function $f(z)$ may be then said to map the point $z = x + iy$ to the point $w = u + iv$. The particular form of the function $f(z)$ depends on the specific boundaries and the application with which we are working. If the function is well behaved, adjacent points in the plane Z are mapped to adjacent points in the plane W (i.e., a line in the plane Z is mapped to a line in the plane W).

If the mapping is conformal, then the relative proportions of neighboring line segments and angles of line segment intersections will be preserved during the transformation. Therefore, any orthogonal set of lines in the original field Z plane appears as another set of orthogonal lines in the trasformed plane. The settings in both planes are images of each other. In the Euclidean norm, the angle between two vectors is defined by their dot product. However, most analytic maps are nonlinear, and so will not map vectors to vectors since they will typically map straight lines to curves. Nevertheless, if we interpret 'angle' to mean the angle between two curves, as illustrated in Fig. 4, then we can make sense of the conformality requirement. The mapping will be one to one if $f(z)$ is linear or bilinear.

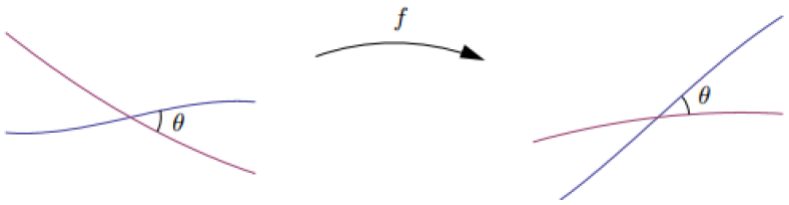

Figure 4: Angle between two curves.

The properties that are needed for a conformal map, are the properties of analytic functions. That is, the function is single-valued (on a Riemann surface) to have a one to one mapping, and differentiable angles do not change under the transformation (isogonal-

ity). These features also serve to ensure continuity. It is such well-behaved functions or mappings that we will consider.

A function $f(z)$ is said to be analytic at a point z if its derivative, defined by

$$\frac{df}{dz} = \lim_{\Delta z \to 0} \frac{f(z+\Delta z) - f(z)}{\Delta z}, \tag{7}$$

exists and is single-valued in some neighborhood of z.

Taking Δz along the real axis results in

$$\begin{aligned} \frac{df}{dz} &= \lim_{\Delta x \to 0} \frac{u(x+\Delta x, y) - u(x,y) + i\left(v(x+\Delta x, y) - v(x,y)\right)}{\Delta x} && (8) \\ &= \frac{\partial u}{\partial x} + i\frac{\partial v}{\partial x}, && (9) \end{aligned}$$

whereas taking the derivative in the imaginary direction results in

$$\begin{aligned} \frac{df}{dz} &= \lim_{\Delta y \to 0} \frac{u(x, y+\Delta y) - u(x,y) + i\left(v(x, y+\Delta y) - v(x,y)\right)}{i\Delta y} && (10) \\ &= -i\frac{\partial u}{\partial x} + \frac{\partial v}{\partial y}. && (11) \end{aligned}$$

On comparing these two expressions, we find that the real and imaginary parts of an analytic function are not arbitrary but must be related by

$$\frac{\partial u}{\partial x} = \frac{\partial v}{\partial y}\,, \tag{12a}$$

and

$$\frac{\partial u}{\partial y} = -\frac{\partial v}{\partial x}. \tag{12b}$$

These two equalities are known as the Cauchy-Riemann equations. The satisfaction of the Cauchy-Riemann equations is both a necessary and sufficient condition for $f(z)$ to be analytic. These can also be expressed as

$$\frac{\partial x}{\partial u} = \frac{\partial y}{\partial v}\,, \tag{13a}$$

and

$$\frac{\partial x}{\partial v} = -\frac{\partial y}{\partial u}. \tag{13b}$$

In a similar fashion, in polar coordinates we can write

$$\frac{\partial u}{\partial r} = \frac{1}{r}\frac{\partial v}{\partial \theta}, \tag{14a}$$

and

$$\frac{\partial v}{\partial r} = -\frac{1}{r}\frac{\partial u}{\partial \theta}. \tag{14b}$$

Summarizing, if the four partial derivatives $\partial u/\partial x$, $\partial u/\partial y$, $\partial v/\partial x$ and $\partial v/\partial y$ of $f(z) = u(x,y) + iv(x,y)$ exist, are continuous over a region, and satisfy Eq.((12)), then the derivative $f'(z)$ exists in the entire region.

An analytic function is a differentiable function. The points at which $f(z)$ is not analytic are called singularities. These usually occur at isolated spots where they can be avoided. The transformation $f(z)$ cannot be conformal at points where the derivative is zero or infinite. These points are called critical points.

If $f(z)$ and $g(z)$ are analytic functions, then so are the functions

$$f(z) \pm g(z) \tag{15}$$

$$f(z)\, g(z) \tag{16}$$

$$f(z)\,/\,g(z) \tag{17}$$

$$f\{g(z)\}. \tag{18}$$

Polynomials and power series within their circles of convergence are also analytic functions.

The inverse of an analytic function, $w = f(z)$, which can also be expressed as $z = f^{-1}(w)$, is also analytic if $f(z)$ is analytic, and its derivative is the reciprocal of the derivative

of $f(z)$. That is

$$\frac{dz}{dw} = \frac{1}{dw/dz}. \tag{19}$$

The differentials of x and y are given by

$$dx = \frac{\partial x}{\partial u}du + \frac{\partial x}{\partial v}dv, \tag{20a}$$

$$dy = \frac{\partial y}{\partial u}du + \frac{\partial y}{\partial v}dv. \tag{20b}$$

Using the Pythagorean theorem to obtain the square of the distance between two neighboring points, we have

$$ds^2 = dx^2 + dy^2. \tag{21}$$

Substituting (20a) and (20b) into (21) we obtain the expression for the square of the distance in the transformed space

$$ds^2 = \left(\frac{\partial x}{\partial u}du + \frac{\partial x}{\partial v}dv\right)^2 + \left(\frac{\partial y}{\partial u}du + \frac{\partial y}{\partial v}dv\right)^2. \tag{22}$$

By developing the above expression and using the Cauchy-Riemman conditions (13), we obtain

$$ds^2 = \left(\frac{\partial x}{\partial u}\right)^2 du^2 + \left(\frac{\partial x}{\partial v}\right)^2 dv^2 + \left(\frac{\partial y}{\partial u}\right)^2 du^2 + \left(\frac{\partial y}{\partial v}\right)^2 dv^2 \tag{23}$$

.

Then we find that

$$ds^2 = \left[\left(\frac{\partial x}{\partial u}\right)^2 + \left(\frac{\partial y}{\partial u}\right)^2\right] du^2 + \left[\left(\frac{\partial x}{\partial v}\right)^2 + \left(\frac{\partial y}{\partial v}\right)^2\right] dv^2. \tag{24}$$

We can then write a compact expression that helps us define the scale factor h of the transformation:

$$ds^2 = (hdu)^2 + (hdv)^2. \tag{25}$$

By means of the Cauchy-Riemann equations, we can see that

$$\left[\left(\frac{\partial x}{\partial u}\right)^2 + \left(\frac{\partial y}{\partial u}\right)^2\right]^{1/2} = \left[\left(\frac{\partial x}{\partial v}\right)^2 + \left(\frac{\partial y}{\partial v}\right)^2\right]^{1/2} = h. \tag{26}$$

Then, the elements of length in the transformed space are

$$ds_u = hdu, \tag{27}$$

$$ds_v = hdv. \tag{28}$$

We then see that locally, a conformal map can be viewed as a transformation to a space of curvilinear coordinates. It is important to emphasize that the scale factor is a function of the coordinates in the transformed space.

Since conformal mappings preserve angles, they are particularly useful in electromagnetic problems specified in terms of boundary conditions involving normal derivatives. As we have already mentioned, an interesting property of conformal mappings is that the Laplace equation is invariant under such transformations. The Helmholtz equation, on the other hand, is only slightly modified and in some cases the advantage obtained by simplifying the border is greater than the problems that such modification can bring (Schinzinger and Laura, 2003). In the complex plane $Z(x, y)$ we can write the Helmholtz equation as

$$\nabla^2\psi(x, y) + n^2k^2\psi(x, y) = 0, \tag{29}$$

where $k = \omega/c$, and $n = \sqrt{\epsilon\mu}$ represents the refractive index.

By considering the effect of the transformation in the differential operations, the Lapplacian can be written as

$$\nabla^2\varphi = \frac{1}{h^2}\left[\frac{\partial^2\varphi}{\partial u^2} + \frac{\partial^2\varphi}{\partial v^2}\right] \tag{30}$$

thus, the Helmholtz equation in the transformed space is given by (**?**)

$$\nabla^2\psi(u, v) + h^2(u, v)n^2k^2\psi(u, v) = 0, \tag{31}$$

where

$$h = \left| \frac{dz}{dw} \right|, \tag{32}$$

and it is assumed that the derivative of the function $f(z)$ is nonzero. We observe that in the transformed space the factor $h(u, v)$ multiples the original refractive index and thus, in the transformed space, the refractive index $n_w(u, v)$ is given by

$$n_w(u, v) = h(u, v) n_z. \tag{33}$$

In this equation, h represents the local change of scale of the transformation and is a function of position in the (u, v) plane. We see that apart from the changes in the boundaries associated with the transformation, the transformation has modified the refractive index from $\sqrt{\varepsilon\mu}$ to an equivalent refractive index $h\sqrt{\varepsilon\mu}$.

2.3 Examples of conformal transformations

We now present a couple of examples of conformal transformations that illustrate some of the possibilities offered by the approach for applications in surface optics and silicon photonics.

2.3.1 The logarithmic transformation

By means of this transformation it is possible to map a close region that is fan-shaped and limited by two circular arcs into a rectangle whose cross section is geometrically constant. The transformation may be written in the form

$$bw = \ln(az) \tag{34}$$

where a and b are constants with appropriate units. Writing

$$z = x + iy = r \exp(i\theta), \tag{35}$$

where $r = \sqrt{x^2 + y^2}$. We find that

$$u = \frac{1}{b}\ln(ar) \tag{36}$$

$$v = \frac{\theta}{b} \tag{37}$$

The situation is illustrated in Fig. 5. The shaded factor shown on the Z plane is mapped into the shaded rectangle shown on the W plane. Circles on the Z plane centered at 0 are mapped to vertical segments on the W plane connecting $u - i\pi$ to $u + i\pi$, where u is the horizontal coordinate in the transformed space given by Eq.(36). Thus, if a circle has an initial radius of $1/a$ in the Z plane as in the Fig. 5, it will map to a vertical segment at $u = 0$ in the W plane by means of Eq. (36). Rays emanating from 0 on the Z plane are mapped to horizontal lines on the W plane. In the example, we considered rays that go from an angle of $\pi/4$ to an angle of $\pi/2$.

Each circle and ray on the Z plane coincide at a right angle. Their images under the transformation are a vertical segment and a horizontal line (respectively) on the W plane that coincide too at a right angle.

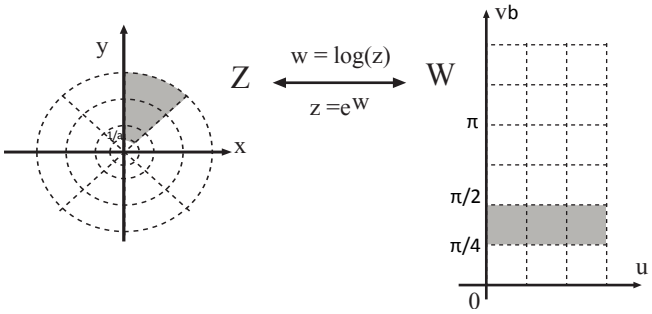

Figure 5: Logarithmic transformation.

From equation (34), we see that

$$\frac{dw}{dz} = \frac{1}{b}\frac{a}{az} = \frac{1}{bz}, \tag{38}$$

and assuming b to be real and positive, we can write the scale factor

$$h = \left|\frac{dw}{dz}\right| = \frac{1}{br}. \tag{39}$$

As we will discuss in Chapter 3, this transformation can lead us to the design of a taper with a gradually varying refractive index to couple a glass waveguide and a high index silicon waveguide while maintaining the modal characteristics of the guides, which is one of the most challenging tasks in the field of silicon photonics. Such a taper waveguide should find applications for sensing (infiltration in the porosity of the silicon), end-fire coupling with fibers and/or 2D sampling interferometry and spectroscopy (M. Renault et al., 2010).

2.3.2 The cycloid

In this section, we present the transformation for a cycloid. The conformal mapping family that we use can be expressed as (Schinzinger and Laura, 2003)

$$z = Aw + i \sum_n b_n \exp\left(inqW\right), \tag{40}$$

where $w = u + iv$ and $z = x + iy$. The constants A and q have units of 1/length. The latter represents a fundamental angular frequency which is related to the period d of the function by $q = 2\pi/d$. To illustrate this family of mappings, we consider the case of the

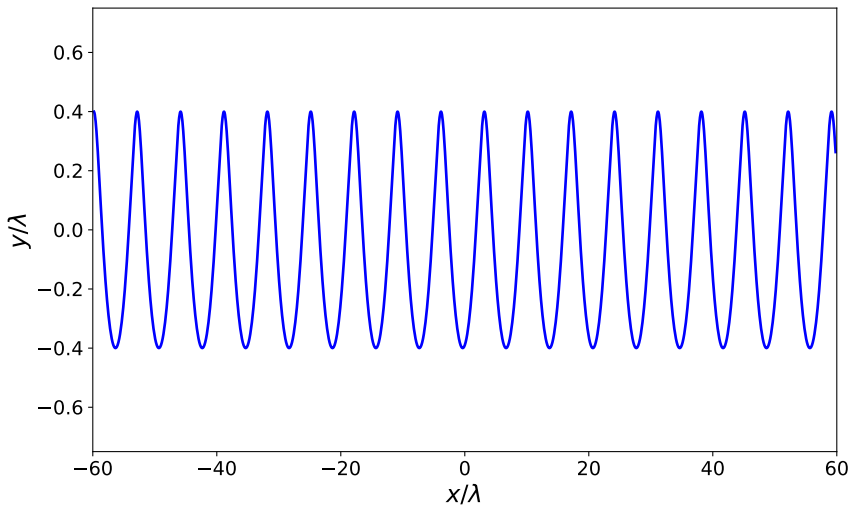

Figure 6: Cycloidal surface with a period of 7λ in the *xy* space.

cycloid, which is the simplest example of it. From Eq. (6), by putting $b_n = 0$ for all $n \neq 1$,

we obtain

$$z = Aw + ib_1 \exp(iqw), \tag{41}$$

or

$$x + iy = Au + iAv + ib_1 \exp(iqu) \exp(-qv). \tag{42}$$

From this expression, we obtain the equations

$$x = Au - b_1 \exp(-qv) \sin qu \tag{43}$$

and

$$y = Av + b_1 \exp(-qv) \cos qu. \tag{44}$$

These equations represent the relationship between the planes (x, y) and (u, v). When $v = 0$, the same equations reduce to the parametric equations

$$x = Au - b_1 \sin qu \tag{45}$$

$$y = b_1 \cos qu \tag{46}$$

These parametric equations describe a surface such as the one depicted in Fig. 6. The constants A and b_1 allow one to change the characteristics of the profile, while q represents an angular frequency that determines the period. A cycloid is obtained when $\frac{2b_1}{A} < 0.31831$. Higher values of this parameter in the profile should be avoided, as the curve would exhibit loops. Examining Eqs.(43) and (44) we observe that the oscillations tend to dissapear as v increases. Considering the horizontal plane defined by $v = \delta$ with $q\delta \gg 1$, one finds that Eqs.(43) and (44) reduce to the expressions

$$x = Au, \tag{47}$$

$$y = Av, \tag{48}$$

which describe a uniform expansion (or compression) transformation. Thus, setting $A = 1$ would not modify the space in the far field of the surface.

From Eq.(6), we have

$$\frac{dw}{dz} = \frac{1}{A - b_1 q \exp(iqw)}, \tag{49}$$

which leads to the $h(u, v)$ factor in the transformed space

$$h(u, v)^2 = \left|\frac{dw}{dz}\right|^2 = \frac{1}{A^2 + b_1^2 q^2 \exp(-2qv) - 2Ab_1 q \exp(-qv)\cos qu}. \tag{50}$$

From Eq. (33), we find that the equivalent refractive index for a cycloid cloak (Fig. 7) will be given by

$$n_w(u, v) = \left[\frac{\epsilon\mu}{A^2 + b_1^2 q^2 \exp(-2qv) - 2Ab_1 q \exp(-qv)\cos qu}\right]^{1/2} n_z. \tag{51}$$

Using this expression, we have calculated numerically the geometry, the scaling factor, and the refractive index distribution for the cycloid that is shown in Fig. 7 Thus, with this transformation, we start with a flat surface in the W space and end up in the Z space with a cycloid surface that has refractive index variations.

On the basis of this result, a cycloid cloak in the optical range could be designed. Such a device will conceal an object under the curved reflecting surface by manipulating

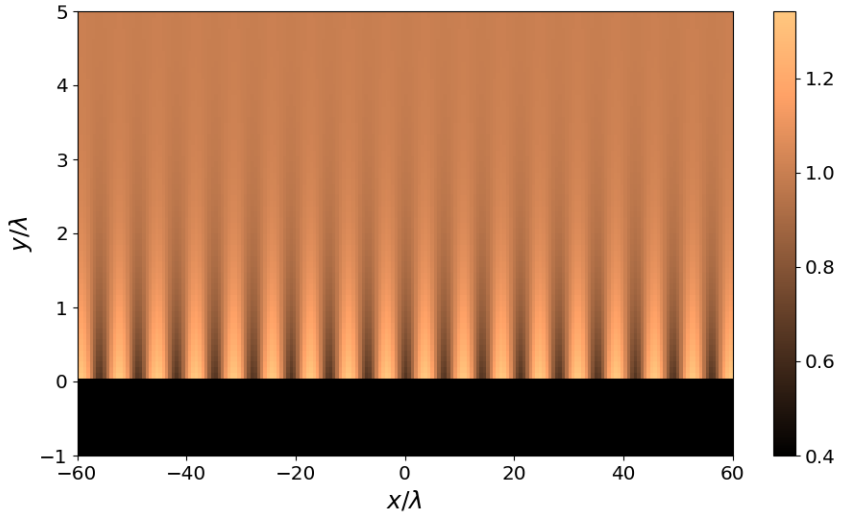

Figure 7: Map of the factor $h(u; v)$ that multiplies the refractive index in transformed space. The calculation was done for a cycloid with a period of 7λ.

the trajectory of light after interacting with it, using refractive index variations obtained by means of the conformal map, and imitating the reflection from a flat surface. Thus, the trajectory will be the same as that in a flat surface, without the cloak or the object underneath. One could then hide objects under those deformations without revealing their existence.

2.3.3 The Joukowski transformation

For a specific mapping, we consider the Joukowski transformation (Schinzinger and Laura, 2003), which is a conformal map historically used to understand some principles of airfoil design. We write

$$w = z + \frac{g^2}{z}. \tag{52}$$

With this transformation, the circular cross section of our cylinder (Fig.8) is transformed

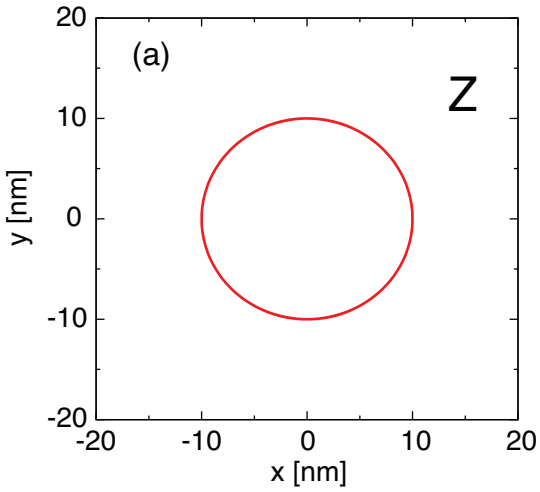

Figure 8: Cross section of the cylinder in the original space.

into an ellipse (Fig.9), provided that the radius $a^2 > g^2$. So, the circle $x^2 + y^2 = a^2$ transforms into an ellipse with major and minor semi-axes $A = a(1 + g^2/a^2)$ and $B = a(1 - g^2/a^2)$. For our particular example, we choose $a = 10\,\text{nm}$ and $g = 2\,\text{nm}$.

$$z = \frac{w}{2} + \sqrt{\left(\frac{w}{2}\right)^2 - g^2}. \tag{53}$$

This results in the following expressions for the (u, v) pair of coordinates

$$u = \left(1 + \frac{g^2}{r^2}\right) x, \tag{54}$$

$$v = \left(1 + \frac{g^2}{r^2}\right) y, \tag{55}$$

with $r^2 = x^2 + y^2$.

The function can then be used to transform a circle into an ellipse.

The transformation results in the following expression for the factor that multiplies the

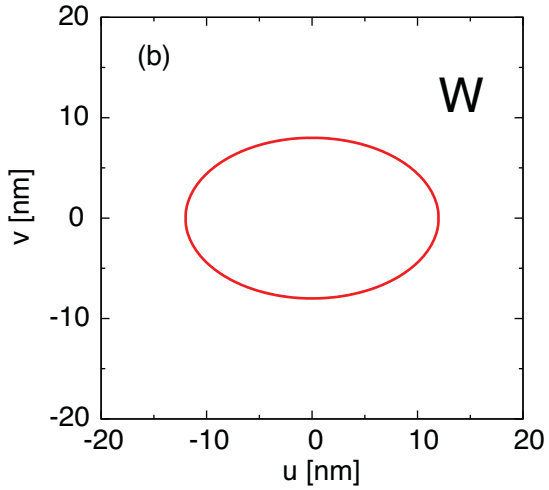

Figure 9: Ellipse in the transformed space.

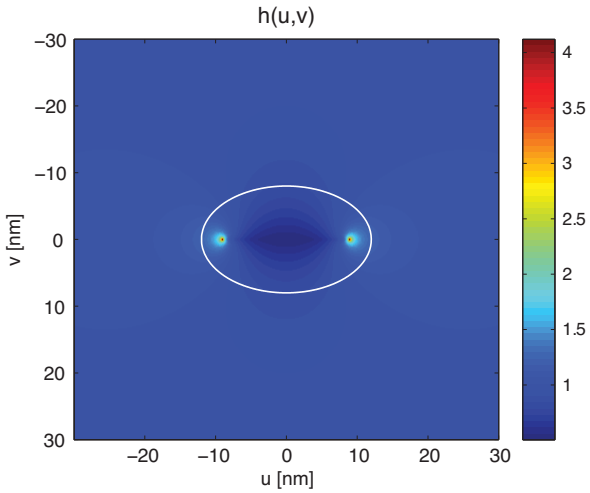

Figure 10: Map of the factor $h(u; v)$ that multiplies the refractive index in transformed space.

original refractive index (Fig. 10)

$$h(u,v) = \left|\frac{dz}{dw}\right| = \frac{1}{2}\left|1 + \frac{1}{\sqrt{1-(2g/w)^2}}\right| \tag{56}$$

Conformal mapping has been used to study 2D optical problems in transformed space that are equivalent situations in real space in which localized surface plasmons are excited. A localized surface plasmon is a non-propagation excitation of the conduction electrons of metallic nano-particles coupled to the electromagnetic field. Starting with a well know problem, like the one that has been discussed in this section from the Joukowski transformation, people have looked at the consequences in transformed space to study problems that are much more difficult to treat analytically and even numerically (Schinzinger and Laura, 2003).

Chapter 3 Nanostructures in silicon photonics

In this Chapter, we first present a brief review of silicon photonics and discuss the schemes reported in the literature for implementing transformation optics concepts in such a platform. Using effective medium ideas, we discuss a procedure to create a binary map of silicon pillars that can mimic a prescribed refractive index variation. The ideas are similar to those employed in the printing industry to create gray scale images with binary pixels. Finally, as an example of the possibilities, we present the design of an optical element based on a conformal transformation that can connect a monomode glass waveguide to a monomode silicon waveguide.

3.1 Silicon photonics

Silicon photonics is the technology for producing optical devices and circuits using silicon as the core material. It permits the integration of optical and electronic components on a single chip using standard CMOS (complementary metal oxide semiconductor) fabrication process. The transparency of silicon at wavelengths (1270 nm to 1625 nm) suggests applications in optical communications, and the adoption of standard silicon-on-insulator (SOI) wafers provides a route for designing waveguide circuits and manipulating light on integrated optical devices. Integrated optical circuits are devices that contain miniaturized optical elements that perform different photonic functions on a common substrate.

It is not surprisingly then, that silicon and in particular SOI wafer have found many applications in photonics. Circuits of integrated optics in a silicon platform constitute an excellent candidate to orchestrate new devices.

Passive optical elements in photonic circuits include branches, expanders, directional couplers and filters. Branches are used to divide a beam into two or more channels. Losses in branches are always significant and, for this reason, directional couplers are often used for these purposes. Expanders are used to change the width of the waveguide, operation that tends to be lossy and usually changes the modal characteristics of the guide.

The fundamental passive device in photonics is the waveguide, through which optical signals can be transferred from one point to another. In the evaluation of the performance of a specific kind of waveguide, both size and propagation loss should be considered. There are two sources of loss that contribute to the propagation loss: intrinsic loss (for ex-

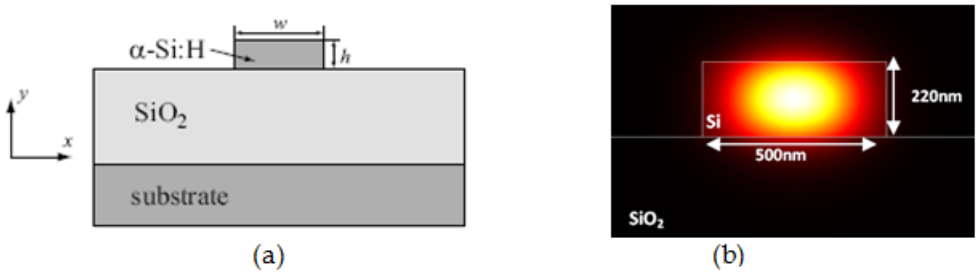

Figure 11: Schematic of a low loss waveguide in a SOI technology.

ample, due to carrier absorption) and extrinsic loss (for example, due to sidewall scattering and radiation into the substrate) The former one is the main source of loss in doping-based waveguides, while the later one becomes significant when the sizes of waveguides are relatively small. The latter is the case of SOI waveguides (Fig. 11), due to the field density at the silicon surface and the roughness at the interface.

SOI is a wafer technology for electronic circuits with two silicon layers. An isolating material (SiO_2) layer is placed between a silicon layer of typically 340 nm or 200 nm, and a substrate of about 500 µm thickness (Fig. 13).

Among the many kinds of Si-related materials that can be used to make waveguides, the most popular is silica. By doping III/V ions into the silica, the refractive index of the core will change with respect of that of the surrouinding glass (cladding) providing the means for waveguiding light In a silica waveguide, the refractive index contrast is low but can be adjusted flexibly by changing the doping density (Fang and Zhao, 2012). However, the low refractive index contrast means that the confinement is weak, which results in both, thick cladding layers (typically of 50 µm) and wide spacing between waveguides. The resulting dimensions make this kind of technology not very compatible with electronic IC technology.

The adoption of silicon-on-insulator (SOI) technology, with the large refractive index

contrast between Si (n = 3.45) and SiO2 (n = 1.45) has some evident advantages in this respect. The strong confinement of the light within the waveguides makes it possible to scale down the size of the waveguides mode to approximately 0.1 μm^2 (Fang and Zhao, 2012). Such lateral and vertical dimensions agree with the requirement for economic compatibility with CMOS technology today (Fig. 12).

Waveguides can be fabricated on SOI wafers using electron beam lithography. For this, the wafer is coated with a thin layer of positive (or negative) electron-beam resist, a material that becomes insoluble (soluble) in developing solutions after exposure to an electron beam. The exposed (unexposed) areas can then be dissolved in a specific solvent. Photonic structures and patterns are then defined by the electron-beam lithography process. The resist is developed leaving the resist mask. The resist pattern is transferred to the top silicon layer, by etching the silicon in the unprotected area down to the buried oxide (BOX) layer, using reactive ion etching (RIE). In Chapter 5 we discuss in more detail the procedures involved.

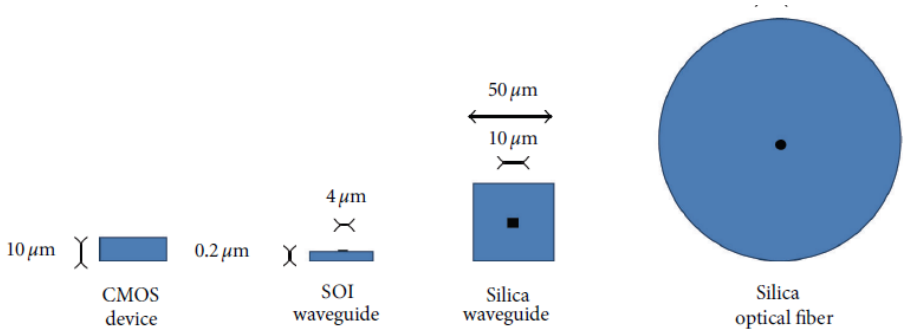

Figure 12: Comparison of the cross-sections of a CMOS chip, a typical SOI waveguide, a silica waveguide, and a silica monomode optical fibre. The Figure was taken from Fang, 2011.

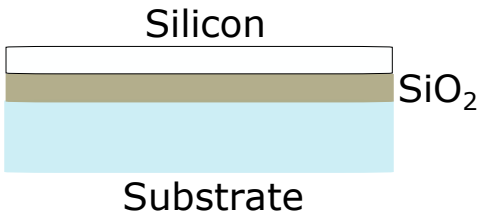

Figure 13: Schematic of the structure of an SOI wafer.

The problem of coupling light efficiently between a single-mode optical fiber (SMF) and a silicon waveguide represents an important challenge, whose solution would allow the intercommunication between the two most prominent technologies for optical communications and signal processing. Since the dimensions of silicon photonics waveguides are much smaller than those of the SMFs, a considerable mode size mismatch appears between the two devices. Thus, the coupling loss will be very large if directly coupling the waveguides with SMFs. One common solution is using surface grating (Fig. 14) to butt-couple light from a SMF, perpendicular to the surface, into planner waveguides.

Another promising alternative is coupling light between fibers and waveguides by combining a Si inverse taper and a medium index contrast waveguide, made by polymer or SiN for example, (Fig. 15). This technique is based on the gradual expansion from the core-guided mode to a much larger cladding-guided mode.

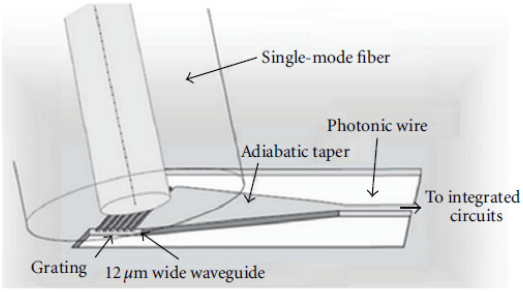

Figure 14: Grating coupler for coupling between photonic wire waveguide and fibre. The Figure was taken from Fang, 2011.

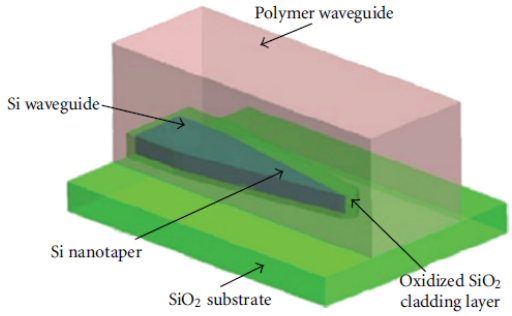

Figure 15: Schematic diagram of the nanotaper coupler. The Figure was taken from Fang, 2011.

3.2 Nanostructured silicon as an effective medium

The 2D nature of integrated optics circuits suggests the use of conformal mapping techniques (Leonhardt, 2006) in the design of novel photonic elements. Conformal mappings constitute a class of two-dimensional transformations that have proved useful in the past for solving diffraction problems (Nevière *et al.*, 1973; Depine and Simón, 1982). Implementing transformation optics concepts in silicon photonics is interesting from both, the conceptual and the applications points of view (Gabrielli and Lipson, 2011). Gabrielli explored the possibility of designing structures by controlling the effective refractive index through the density of nanometric silicon pillar structures. There are, for instance, reports of the use of transformation optics and nano-structured silicon to fabricate a cloaking device in the optical domain (Gabrielli et. al, 2009), and a device for focusing light in the near infrared (Spadoti et. al, 2010, Gabrielli and Lipson, 2010).

Their central idea is to vary the filling fraction f of pillars (volumetric fraction of Si in relation to air) at each point of a slab. Regions essentially formed by a low filling fraction of Si pillars surrounded by air will then result in a low refractive index value, while the maximum effective refractive index available will be obtained by a slab completely filled with Si. Gabrielli et al., (2011), used a simple effective medium theory, the 1D Maxwell Garnett (slabs) in *s* polarization, to relate the layer of air and silicon pillars to an equivalent layer with effective medium properties using the following relation

$$\epsilon_{\text{eff}} = 1 + f(\epsilon_s - 1), \tag{57}$$

where ϵ_s is the permittivity of silicon, we are assuming that the pillars are in air, and ϵ_{eff} is the effective permittivity that one wishes to achieve. In Chapter 4, we shall see that this expression corresponds to the 1D Maxwell Garnett formula for the case of *s* polarization. According to them, the effective material theory will hold if the pillar size is smaller than the wavelength. Using this method they fabricated several devices for the optical regime such as an invisibility cloak, a light concentrator and a perfect imaging planar lens. Figure 16 shows a SEM image of their fabricated cloaking device. Once this device was introduced in front of a deformed mirror, its reflection was similar to the one coming from a flat mirror. A

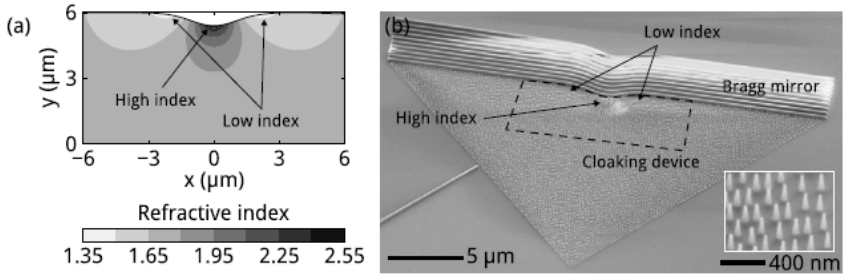

Figure 16: Cloaking device. (a) Initial refractive index map of the cloaking device. (b) SEM image of the fabricated device. The map (a) corresponds to the main cloaking device (dashed area). The inset is a zoomed-in view of the Si nano-structures that compose the device. The Figure was taken from Gabrielli and Lipson, 2012.

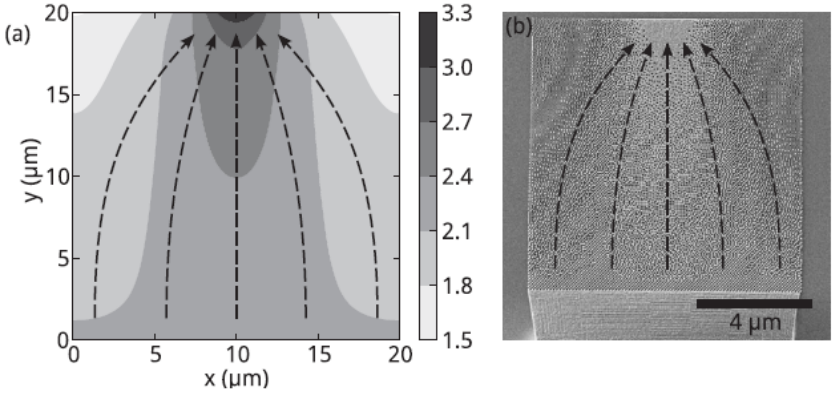

Figure 17: Light concentrator. (a) Refractive index map of the device. Light from the bottom is concentrated towards a tighter spot on the centre of the top edge where the refractive index is higher. (b) SEM image of the fabricated device corresponding to the dithered version of the designed index gradient. The arrows indicate how light travels in the device and concentrates towards the top edge. Light concentrator. (a) Refractive index map of the device. Light from the bottom is concentrated towards a tighter spot on the centre of the top edge where the refractive index is higher. (b) SEM image of the fabricated device corresponding to the dithered version of the designed index gradient. The arrows indicate how light travels in the device and concentrates towards the top edge. The Figure was taken from Gabrielli and Lipson, 2012.

SEM image of their light concentrator is shown in Fig. 17. This device is able to compress light incident on the input boundary to a small area on the opposite side. Finally, with a design based on the conformal mapping of a spherical surface into a plane, they fabricated a lens in which any source point on the surface produces a perfect image of itself on the opposite side of the lens.

To our knowledge, however, the accuracy of the EMT used in these works has not been tested for the kinds of structures and refractive index contrasts encountered in silicon photonics.

3.2.1 Dithering algorithms

The conversion of a given refractive index map into a density of pillars is based on concepts of effective medium theory. By means of an EMT one can obtain a continuous density function of position that needs to be converted into a specific recipe of where to put the pillars. This is accomplished through a dithering algorithm. The idea is similar to the conversion of grey-scale images into binary maps that is used in printing and display technologies. With such algorithms, one can express the exposure map as a matrix of ones (silicon) and zeroes (air). An example of the use of a dithering algorithm to display a gray

Figure 18: Original image in shades of grey (left) and dithered image (right).

scale image in terms of black and white pixels is shown in Fig. 18. The photography on the

left is the original and the one in the right is the processed one (actually, the photography on the left is also displayed in terms of black and white dots, but on a much finer scale). One of the most popular dithering algorithms is the Floyd-Steinberg algorithm, which is based on error dispersion (Floyd and Steinberg, 1976). With this technique one needs to find if the shade of gray of each point in an image is closer to black or to white, set it to the closest value and distribute the error over the neighboring pixels. Thus if, for example, the first pixel in an image is dark gray, and has a value of 96 on a scale from 0 to 255 (zero being black and 255 being white), it is set to zero and the difference between o and 96 is distributed over the neighboring pixels that have not been visited yet, accordingly to the following distribution

$$\begin{bmatrix} & & & & \\ & & * & \frac{7}{16} & \cdots \\ \cdots & \frac{3}{16} & \frac{5}{16} & \frac{1}{16} & \cdots \end{bmatrix}, \tag{58}$$

where the matrix represents a map of neighboring pixels. The cell with a star (*) indicates the pixel currently being scanned, and the blank cells are the pixels that have been already visited. The weights represent the proportion of the error distributed to the neighboring pixels. Here, the pixel immediately to the right of the scanned one gets $7/16$ of the error (the divisor is 16 because the weights add to 16), the pixel directly below gets $5/16$ of the error, and the diagonally adjacent pixels get $3/16$ and $1/16$. With the use of error dispersion algorithm, for an image that has only one shade of gray, represented by the number 128, we would end up with an image of black and white pixels in a pattern similar to that of a chess board.

The variant of the algorithm that we used in this thesis is the simplest, since we were not interested in any artistic detail of the dithered image. On this variant, the image is scanned from left to right, but there are also other options: scanning right-to-left, an alternating left-to-right, where the scan is alternated between lines, etc.

3.2.2 Design of an expander/compressor for integrated optics

Once we have discussed the posibility of converting refractive index regions into pillar density maps and specific recipes of where to put or not to put pillars, we focus our at-

tention on the design of an optical element that would be useful in integrated optics with silicon waveguides. Specifically, we present the design of a taper to couple light from a monomode glass waveguide into a silicon waveguide. The ability to compress and expand light has many applications in optics, ranging from beam collimation to nanolithography, optical data storage, imaging quality enhancement and efficient coupling to nanoscale structures (Renault *et al.*, 2010; Delacour *et al.*, 2010). Transformation optics offers a new way to achieve these effects, since it provides the necessary medium to force electromagnetic fields to undergo the spatial distortion introduced by a certain coordinate transformation (Leonhardt and Philbin, 2009). Conformal mapping transformations enable us to compensate for geometrical alterations, such as bends or shifts, using materials with a spatially dependent refractive index. So, CM techniques represent an attractive possibility for the design of expander/compressor structures. In contrast with previously proposed tapers based on transformation optics, where more complex materials are needed, or where the electromagnetic consequences of the selected transformation are not clear (García-Meca *et al.*, 2011), our proposal presents the important advantage of having a refractive index map constrained to the range of values that can be achieved using nano-lithography on a silicon platform.

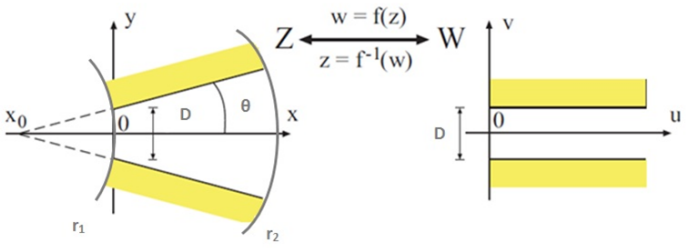

Figure 19: Waveguide with a constant cross-section in the *Z* space transformed in a fan-shape waveguide in the *W* space by means of a logarithmic conformal map.

To demonstrate the feasibility of conformal mapping techniques in integrated optics, we used the inverse of the logarithmic transformation of Section 2.3.1, to convert a rectangular region into an angular section with a gradually varying refractive index that can connect a

silicon waveguide with a glass waveguide. This transformation is given by

$$z = \exp(w), \tag{59}$$

where $w = u + iv$, and $z = x + iy$. Writing $z = r\exp(i\theta)$, we find

$$x = r\cos\theta = \exp(u)\cos v, \tag{60a}$$

and

$$y = r\sin\theta = \exp(u)\sin v. \tag{60b}$$

We observe that a line that corresponds to constant θ is mapped into a line with constant v. Thus, the pie-shaped sector delimited by the shaded region in Z-space is mapped into the rectangular region in W-space.

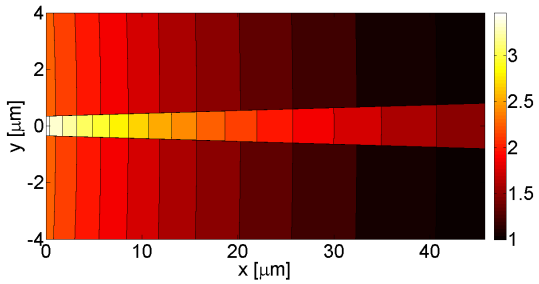

Figure 20: Map of the refractive index variations in the transformed space for the designed expander/compressor.

In our design, we started with a 2D silicon waveguide with a constant cross-section in air in the space W (see Fig. 19), and ended up with a waveguide that is fan-shaped in the Z space. The waveguide in the transformed space starts from the plane $x = 0$, has an initial aperture D with a vertical dimension y_{min}, and a growth angle θ considered as positive. The initial aperture will couple with the silicon waveguide, while the the opposite end in y_{max} will couple with the glass waveguide. The vertical dimension of y_{max} is approximately 800 *nm*. This value was chosen in order to experimentally allow a single mode operation at the desired operation wavelength of $\lambda = 1.55$. The refractive index map must be constrained

to the range of values from $n_{si} = 3.5$ to $n_g = 1.5$, to connect both waveguides. This relation change can be expressed in the form

$$\frac{n_{si}}{n_g} = \frac{3.5}{1.5} = 2.33. \tag{61}$$

From Eq. (33), the refractive index in the transformed space varies as

$$n(x, y) = h(u, v)n_{si}, \tag{62}$$

where from Eq. (32) and Eq. (59), we have

$$h(u, v) = \frac{dz}{dw} = \exp(w). \tag{63}$$

By physical considerations, the refractive index decreases as a function of x, that is, as the waveguide cross section increases. We then rewrite the expression (62) for the refractive index along our device as

$$n(x, y) = n_{si} \exp(-w). \tag{64}$$

By keeping the factor (61) for the relation change of y, we have

$$\frac{y_{max}}{y_{min}} = 2.33, \tag{65}$$

from where the geometrical parameter y_{min} is determined. A schematic of the refractive index distribution in the design can be seen in Fig. 20.

Chapter 4 Effective medium theories

In optics, effective medium theories (EMTs) can be used to calculate the optical constants of a mixture of materials in terms of the optical constants of the components and their volume fractions. In these approaches, it is presumed that an inhomogeneous material possesses macroscopic uniformity on a scale comparable with the wavelength. In this Chapter we present a brief review of the classical theories of Maxwell Garnett (1904) and Bruggeman (1935). These approaches will be used in later chapters where we discuss their application in the context of silicon pillars in air.

4.1 Introduction

For some years now, a field of research has been developed that focuses on composite materials, different from those occurring naturally. The properties of these artificial materials are primarily due to the inclusion of small structures made specifically to achieve these properties. Theories to treat such materials are known as EMTs, and apply when their inclusions are large enough so that every point can be described by a single dielectric function, but small enough compared to the wavelength of the field that illuminates them.

These theories are based on the observation that when heterogeneities in an inhomogeneous medium are much smaller than the wavelength, the medium behaves as a homogeneous medium with optical properties that differ from those of its constituents. In cases in which the artificial material presents both electrical and magnetic properties, due to its structure rather than its composition, we can say that we are talking about a metamaterial. As more and more composite microstructures are being developed on smaller and smaller length scales, it is clear that this type of approach will become even more valuable in the future than it has been in the recent past.

There have been several attempts to develop EMTs. The classical approaches are the Maxwell Garnett (1904) and Bruggeman (1935) theories that describe the optical properties of a heterogeneous dielectric mixture as a function of the dielectric function of its components and their volume fractions. Both theories assume spherical inclusions and

consider only dipole interactions. However, they differ in the treatment of the two components of the composite system. The microstructure described by Maxwell Garnett consists of grains of one component embedded in a matrix of the other component, whereas in Bruggeman's case, the two components are treated in an equivalent manner.

4.2 Maxwell Garnett theory

4.2.1 A dielectric sphere in a uniform electric field

The Maxwell Garnett approximation starts from the macroscopic Maxwell's equations, which are assumed to be valid on a fine scale inside a composite. The initial system considered in this derivation (see Fig.21) is a dielectric sphere of radius a with permittivity ϵ_s in vacuum or air (permittivity 1), placed at the origin of our system of coordinates in an initially uniform electric field which, at large distances from the sphere, is directed along the z axis. In the absence of the sphere, the electric field $\mathbf{E}_0$ is

$$\mathbf{E}_0 = E_0\,\widehat{\mathbf{z}} = E_0\left(\widehat{\mathbf{r}}\cos\theta - \widehat{\boldsymbol{\theta}}\sin\theta\right). \tag{66}$$

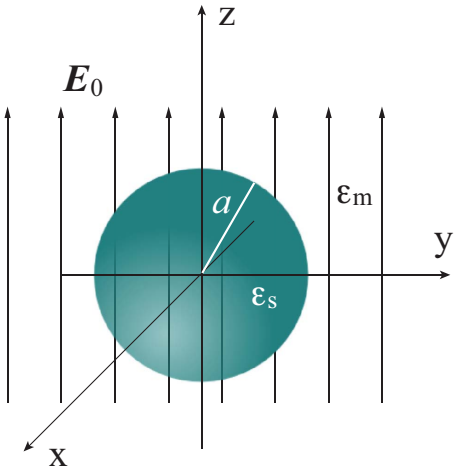

Figure 21: Dielectric sphere of radius a in a uniform electric field of magnitude E_0 along the z-direction. The sphere has permittivity ϵ_s and is in a medium with $\epsilon_m = 1$.

The applied field and induces a polarization field in the sphere that modifies the original one. An elementary electrostatics calculation (Jackson, 2007) reveals that the field inside

the sphere is uniform and given by the expression

$$\mathbf{E}_{\text{in}} = \frac{3}{\epsilon_s + 2}\,\mathbf{E}_0. \tag{67}$$

Similarly, the field outside the sphere can then be written as the sum of the original external field and the polarization field:

$$\mathbf{E}_{\text{out}} = \mathbf{E}_0 + \frac{\epsilon_s - 1}{\epsilon_s + 2}\left(\frac{a}{r}\right)^3 E_0\left(\widehat{\mathbf{r}}\,2\cos\theta + \widehat{\boldsymbol{\theta}}\sin\theta\right). \tag{68}$$

The polarization field, represented by the second term, has the form of the field produced by an electric dipole at the origin of coordinates, which in cgs units has the expression:

$$\mathbf{E}_{\text{dipole}} = \frac{p}{r^3}\left(\widehat{\mathbf{r}}\,2\cos\theta + \widehat{\boldsymbol{\theta}}\sin\theta\right), \tag{69}$$

where p represents the magnitude of the dipole moment.

Comparing the second term of Eq. (68) with Eq. (69), we find that the induced dipole moment can be written as

$$\mathbf{p} = \frac{\epsilon_s - 1}{\epsilon_s + 2}\,a^3\,\mathbf{E}_0 = \alpha\,\mathbf{E}_0, \tag{70}$$

where we have introduced the polarizability of the sphere

$$\alpha = \frac{\epsilon_s - 1}{\epsilon_s + 2}\,a^3. \tag{71}$$

4.2.2 A collection of dielectric spheres

Let us now consider, a cubic array of dielectric spheres in a dielectric medium under a uniform electric field. The macroscopic electric field $\mathbf{E}_{\text{mac}}$ is the sum of the external field and the polarization field, and let us further assume that we know the macroscopic field inside this medium.

The dipole moment induced on the spheres can be calculated if one knows the field

acting upon them. The usual assumption (Lorentz, 2011) is that the local field experienced by a sphere is not the macroscopic field but, instead, a local field that is produced by all the sources and polarized dipoles in the system, except for the sphere on the site in question (see Fig. 22). To calculate the local field we draw a sphere of radius L (Lorentz sphere) centered on the point of interest. The dimensions of the Lorentz sphere must be greater than the distance between particles but smaller than the wavelength. The contributions to the microscopic field in this cavity can be divided in two parts:

1. Contributions due to the induced dipoles inside the Lorentz sphere.
2. Contributions due to the induced dipoles outside the Lorentz sphere.

The first contribution depends on the crystal structure, but Lorentz (1916) showed that it vanishes for the case of a cubic lattices. It is also expected to vanish for completely random arrangements (Jackson, 2007).

To calculate the second contribution it is convenient to adopt a macroscopic approach, treating the medium outside the Lorentz sphere as a continuum with polarization $\mathbf{P}$ (electric dipole moment per unit volume). It is not difficult to show (Jackson, 2007) that this contribution to the field inside the Lorentz sphere is $\mathbf{E}_2 = (4\pi/3)\mathbf{P}$. Then, the local field can be written as

$$\mathbf{E}_{\text{loc}} = \mathbf{E}_{\text{mac}} + \frac{4\pi}{3}\mathbf{P}\,, \tag{72}$$

We denote the number of spheres per unit volume by n_0, so that the Lorentz sphere of volume $V = (4\pi/3)L^3$ contains N spheres and $n_0 = N/V$. In the continuum approximation, the polarization inside the Lorentz sphere can be written as

$$\mathbf{P} = n_0\mathbf{p} = n_0\alpha\mathbf{E}_{\text{loc}}. \tag{73}$$

Using Eq. (72), we can write

$$\mathbf{P} = n_0\alpha\left[\mathbf{E}_{\text{mac}} + \frac{4\pi}{3}\mathbf{P}\right], \tag{74}$$

and solving for **P**, we find

$$\mathbf{P} = \frac{n_0\alpha}{\left[1 - \frac{4\pi}{3}n_0\alpha\right]}\mathbf{E}_{\text{mac}}. \tag{75}$$

The electric displacement vector is

$$\mathbf{D} = [\mathbf{E}_{\text{mac}} + 4\pi\mathbf{P}] = \epsilon_{\text{eff}}\mathbf{E}_{\text{mac}}, \tag{76}$$

and using Eq. (75), the effective permittivity of the system ϵ_{eff} may be written as

$$\epsilon_{\text{eff}} = \left[1 + \frac{4\pi n_0\alpha}{1 - \frac{4\pi}{3}n_0\alpha}\right]. \tag{77}$$

We recall that the volume filling fraction of spheres is

$$f = n_0\left(\frac{4\pi}{3}a^3\right), \tag{78}$$

and using also the definition of α [Eq. (71)], we can write

$$4\pi n_0\alpha = 3f\alpha^*, \tag{79}$$

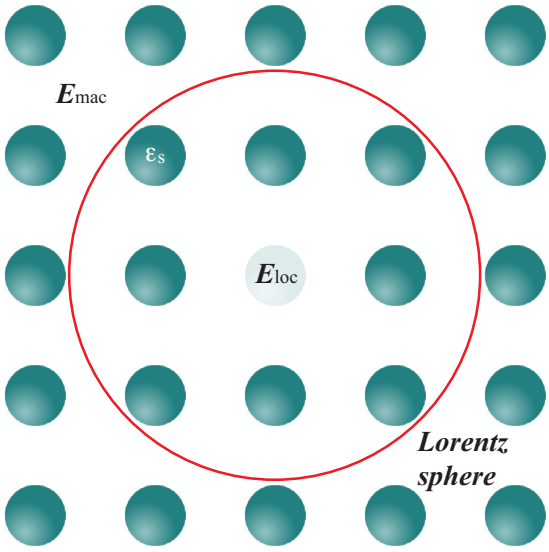

Figure 22: A collection of dielectric spheres embedded in a dielectric medium as considered in the Maxwell Garnett model.

where

$$\alpha^* = \frac{\epsilon_s - 1}{\epsilon_s + 2} \tag{80}$$

represents the polarization factor of the sphere.

Then, Eq. (77) can be written as

$$\epsilon_{\text{eff}} = \frac{1 + 2f\alpha^*}{1 - f\alpha^*}. \tag{81}$$

This is the Maxwell Garnett mixing formula for a host of dielectric materials that contain inclusions of permittivity ϵ_s, where f_s is the volume fraction of the inclusions. It is useful to write this expression in the more symmetric form

$$\frac{\epsilon_{\text{eff}} - 1}{\epsilon_{\text{eff}} + 2} = f\frac{\epsilon_s - 1}{\epsilon_s + 2}. \tag{82}$$

Similar procedures can be carried out for system of one (slabs) and two dimensions (cylinders). Defining d as the dimensionality of the problem (d = 3 in the present case), the generalized form of Eq. (82) for spheres in a medium with permittivity ϵ_m is given by (Bergman, 1978)

$$\frac{\epsilon_{\text{eff}} - \epsilon_m}{\epsilon_{\text{eff}} + (d-1)\epsilon_m} = f\frac{\epsilon_s - \epsilon_m}{\epsilon_s + (d-1)\epsilon_m}. \tag{83}$$

This expression applies for the case in which the polarization vector is perpendicular to the cylinder axis or to the slabs. Solving for ϵ_{eff}, one finds

$$\epsilon_{\text{eff}} = \epsilon_m\frac{1 + (d-1)f\alpha^*}{1 - f\alpha^*}, \tag{84}$$

where $\alpha^* = (\epsilon_s - \epsilon_m) / [\epsilon_s + (d-1)\epsilon_m]$.

4.2.3 the 1D case

When using effective medium theory in the 3D approach, we are considering spheres immersed in a host medium in such a way that the orientation of the incoming light is not important. However, when considering the 2D and 1D cases, we are no longer dealing

with spheres but with cylinders and thus, it is necessary to distinguish between the two different polarizations, *s* and *p*, in the effective medium equations.

An expression for the MG solution in the *p* polarization (electric field perpendicular to the *z* axis) is obtained from Eq. (83) by putting $d = 2$ or $d = 1$. For $d = 1$, we obtain

$$\epsilon_{eff}^{p} = \frac{\epsilon_s \epsilon_m}{+\epsilon_s - f\left(\epsilon_m - \epsilon_s\right)} \tag{85}$$

A close form for the MG solution but for the *s* (electric field parallel to the *z* axis) polarization has been used by Gabrielli (2011) when dealing with silicon structures of nanopillars. This expression can be written as

$$\epsilon_{eff}^{s} = f\left(\epsilon_m - \epsilon_s\right) + \epsilon_s \tag{86}$$

As recalled in the work of Nakamura et al., (2004), for the case of slabs of permittivity ϵ_s in a medium with permittivity ϵ_m, the effective permittivities for the case of *s* and *p* polarization are given by the same Eqs. (85) and (86).

4.3 Bruggeman theory

The Maxwell Garnett result is only valid in the dilute limit. As the filling factor increases, the difference between the host material and the inclusions becomes less clear and the theory is expected to fail. Motivated by the need for an effective medium approximation that treats the components in a symmetric fashion, Bruggeman developed the approach that today bears his name (Bruggeman, 1935; Choy, 1999). It also has the advantage that it can straightforwardly be generalized to more than two components (Fig.23).

Considering now spherical particles of two different materials (ϵ_1, ϵ_2) that are dispersed in a host medium of permittivity ϵ_h, and volume filling factors of the two inclusions given by f_1 and f_2. For this case, Eq. (82) should be modified to

$$\frac{\epsilon_{eff} - \epsilon_h}{\epsilon_{eff} + 2\epsilon_h} = f_1 \frac{\epsilon_1 - \epsilon_h}{\epsilon_1 + 2\epsilon_h} + f_2 \frac{\epsilon_2 - \epsilon_h}{\epsilon_2 + 2\epsilon_h}, \tag{87}$$

where the two inclusions have been introduced in a symmetric manner. For a two-phase composite where $f_1 + f_2 = 1$, each constituent should be regarded as an inclusion and the host medium is the composite itself. Therefore, in Eq. (87) we set $\epsilon_{eff} = \epsilon_h$. Thus, we have

$$f_1 \frac{\epsilon_1 - \epsilon_{eff}}{\epsilon_1 + 2\epsilon_{eff}} + f_2 \frac{\epsilon_2 - \epsilon_{eff}}{\epsilon_2 + 2\epsilon_{eff}} = 0 \tag{88}$$

This is the effective medium expression first developed by Bruggeman (1935). We generalize this expression by replacing the term $(\epsilon_i + 2\epsilon_{eff})$ in the denominator by $[\epsilon_i + (d-1)\,\epsilon_{eff}]$. Equation (88) then becomes (Bergman, 1978; Zhang, 2007)

$$f_1 \left(\frac{\epsilon_1 - \epsilon_{\text{eff}}}{\epsilon_1 + (d-1)\epsilon_{\text{eff}}} \right) + f_2 \left(\frac{\epsilon_2 - \epsilon_{\text{eff}}}{\epsilon_2 + (d-1)\epsilon_{\text{eff}}} \right) = 0. \tag{89}$$

This equation is quadratic in ϵ_{eff} and its (physically acceptable) solution is

$$\epsilon_{\text{eff}} = \frac{1}{2(d-1)} \left(\gamma + \sqrt{\gamma^2 + 4(d-1)\epsilon_1\epsilon_2} \right), \tag{90}$$

where $\gamma = d\,\bar{\epsilon} - \epsilon_1 - \epsilon_2$ and $\bar{\epsilon} = f_1\epsilon_1 + f_2\epsilon_2$. In writing Eqs. (89) and (90), we have assumed that, within the unit cell of sides a, the probability of having a material with dielectric constant ϵ_1 is f_1, and the probability of having material with ϵ_2 is f_2. In contrast with the model of Maxwell Garnett, the model of Bruggeman allows for an arbitrary concentration of the inclusions.

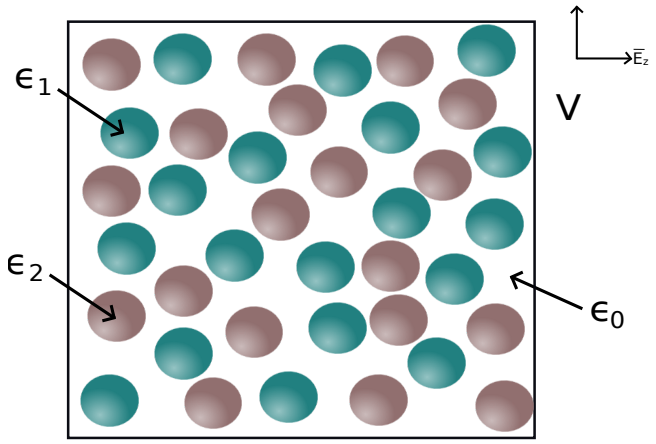

Figure 23: A collection of dielectric spheres embedded in a dielectric medium as considered in the Bruggeman mixed material model.

Chapter 5 Experimental techniques

In this Chapter we describe the fabrication of nanostructured Si samples, purposely designed to study the concepts described in Chapts. 3 and 4, as well as some practical considerations for their implementation. Our aim was to fabricate samples with variable densities of Si pillars with the smallest feature size achievable with our system and the materials employed. We also present measurements of the reflectivity of random and periodic samples with a uniform filling fraction, and compare the results with those of a simple three-layer model in which we assume that the nanostructured layer behaves as a homogeneous effective medium layer.

5.1 Fabrication procedure

The fine structure in the silicon samples was produced using electron beam lithography (EBL) techniques. EBL is a specialized technique in which a beam of electrons is scanned across a surface covered with a resist film sensitive to those electrons, thus exposing the film to a desired pattern.

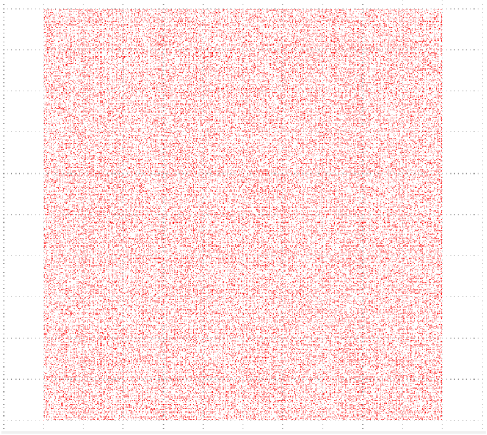

Figure 24: Binary elements displayed in the GDS format.

Conventionally, in EBL, the pattern that one wants to transfer to the sample is defined in a Graphic Database System (GDS) (Griesmann, 2013) file. The GDS library or database

format is a binary file format representing planar geometric shapes in hierarchical form. This database is fed into an electron scanning microscope in a writing mode, where a software converter translates the GDS data into a file which contains all the instructions needed by the pattern generator to direct and scan the e-beam as required. When the file is loaded into the control software of the microscope, the elements are displayed in binary form, as shown in Figure 24.

The basic idea behind EBL is similar to that in other kinds of lithography. A substrate is coated with a thin layer of resist, which is chemically changed under exposure to the electron beam. Then, the exposed (positive lithography) or non-exposed (negative lithography) areas can be dissolved in a specific solvent. The fabrication process is normally carried out on with a silicon-on-insulator (SOI) wafer with a 340 *nm* layer of Si over a 2 μm SiO_2 substrate. These two layers are supported by a thicker silicon substrate.

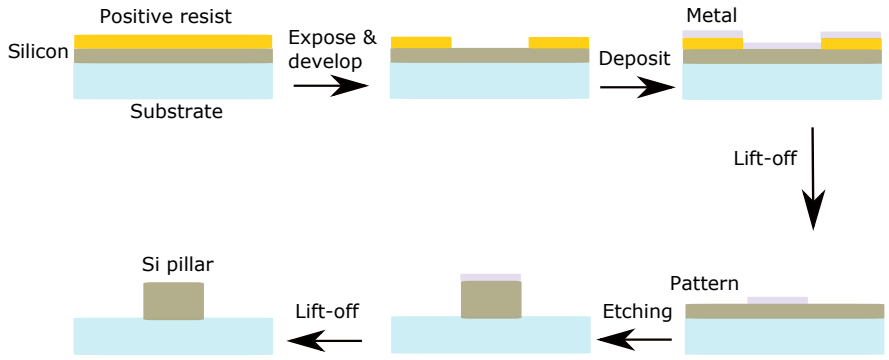

Figure 25: Schematic image of the fabrication process using a positive resist.

Figure 25 shows a schematic diagram of the fabrication process for cases in which a positive resist like polymethyl methacrylate (PMMA) is used. The wafer is first spin-coated with a layer of PMMA, rinsed in isopropanol, blown dry under nitrogen flux, and baked on a hot plate for a few minutes. After this, a espacer (or charge dissipation liquid polymer) layer is spin-coated on the wafer, and rinsed with deionised water. The thin layer of espacer is highly conductive, and helps to avoid charging problems during the writing processes. The exposure to the electron beam changes the solubility of the resist, enabling selective removal of the exposed or regions of the resist by immersing it in a solvent (developing). In the case of PMMA resist, the sample is developed in a solution

of Methyl isobutyl ketone (MIBK) for a few seconds, rinsed in isopropanol and blown dry under nitrogen flux. After exposure and development an inverse or negative pattern is then created in the PMMA layer. Following the development, a metal layer is deposited over the wafer, which includes the bared areas of the substrate (exposed regions) and the top of the PMMA layer in the unexposed regions. After a lift-off process consisting of immersion of the sample in acetone, the PMMA and the metal layer above it are removed, leaving only a metal layer with the exposure patter over the silicon substrate. Finally, a reactive ion etching (RIE) process using oxygen (O_2) is performed, so that the silicon remains only in regions protected by the metal coating. In RIE the plasma is generated under low pressure (vacuum) by an electromagnetic field that ionizes gas molecules. High-energy ions from the plasma attack the silicon on the wafer surface and remove material.

In negative lithography, the wafer is spin-coated with a thin layer of negative resist, like hydrogen silsesquioxane (HSQ), rinsed in isopropanol, blown dry under nitrogen flux, and baked on a hot plate for a few minutes. After this, a espacer layer is spin-coated on the wafer and rinsed with deionised water. During the EBL, the resist is chemically changed under exposure to the electron beam, so that the non-exposed areas can be dissolved leaving regions covered by HSQ. After exposure the sample is developed in a solution of MF-319 for a time that is normally under a minute, rinsed in deionised water, and blown dry under a nitrogen flux. The patterns are then defined by a two step RIE process using first O_2, and then O_2 and sulfur hexafluoride (SF_6). The fabrication process is shown schematically in Fig. 26.

Figure 26: Schematic image of the fabrication process using a negative resist.

5.1.1 First tests

Some tests were carried out in order to gain expertise in the fabrication method. We fabricated six samples with periodic arrays of pillars. Each sample contained four zones of

80 µm $\times$ 80 µm with a 100 nm diameter pillars and periods of 150 , 200 , 300 and 400 nm, and another four zones of the same with periodic arrays of pillars with a 200 nm period and pillar diameters of 50 , 75 , 100 and 150 nm. The maximum SEM working area is 100 µm $\times$ 100 µm, thus, by choosing a smaller working area for the exposed areas we avoided the use of stitching techniques. The fabrication of periodic samples of pillars with different diameters and periods was helpful to determine the limits of resolution of our system and fabrication process.

Of the six samples, two were fabricated using one layer of positive resist (PMMA), for two other samples we used one layer of negative resist (HSQ) and for two more, we used two layers of the same HSQ negative resist. The negative HSQ resist has been investigated widely due to its high resolution capability, etch resistance and good stability under SEM inspection. On the other hand, PMMA is a conventional electron beam resist that is known for its good lift-off properties. Lift-off is applied in cases where a direct etching of structural material would have undesirable effects on the layer below. Positive and a negative resist, were used in order to determine the best option for the fabrication of the structures. Samples of one and two resist layers were fabricated to find an adequate resist thickness for fabrication. This parameter is important since a thicker resist layer allows a longer etch time for better-defined pillars, but also reduces the achievable resolution. A negative resist was preferred for the tests because it requires exposure of smaller areas and consumes less EBL time.

For the two samples fabricated with positive resist, the process started by spin-coating a 200 nm layer of PMMA. The coated wafers were then rinsed in isopropanol, blow-dried under a nitrogen flux and baked on a hot plate at 180 °C for four minutes. After this, a 300Z espacer layer was spin-coated on both samples and rinsed with deionised water. The EBL was carried out in a Raith system with an exposure dose of $140 \mu C/cm^2$. After exposure, the samples were developed in a MIBK solution for 60 seconds, rinsed in isopropanol for 15 seconds and blow-dried under a nitrogen flux. Following the development, a 50 nm layer of aluminum (Al) was deposited on one of the samples, while a layer of chromium (Cr) of a 40 nm thickness was deposited on the other one. A lift-off process was performed in both samples before the O_2 RIE process, which was carried out with a Plassys MEB400

at a 2 mTorr pressure and a 100 W power for 5 (Al) and 60 (Cr) seconds.

In Fig. 27 we show SEM images of the PMMA sample after the e-beam lithography (left), and after the etching process (right). We see that by the use of the PMMA resist, we obtained a good definition of the pillars once the etching process was performed.

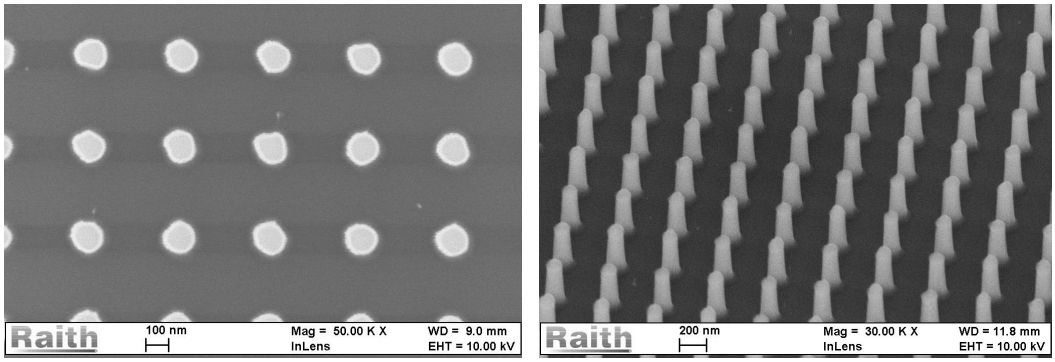

Figure 27: SEM images of a fabricated sample using PMMA resist and 50 *nm* thick Al deposition in the zone with a 100 *nm* pillar diameter and 300 *nm* period. After performing the EBL (left), and after the etching process (right).

The fabrication process with the negative resist started by spin-coating a 200 nm HSQ layer on each of the four remaining wafers. They were all then rinsed in isopropanol, blow-dried under nitrogen flux and baked on a hot plate at 150 °C for two minutes. This process was repeated with two of the samples, so they ended up with a 400 nm layer of HSQ. After this, a 300Z espacer layer was spin-coated on all the samples and rinsed with deionised water. With the single layer samples, the EBL was carried out in a Raith system using a dose of $200\mu C/cm^2$ in one sample and $300\mu C/cm^2$ in the other one. For the two layer samples, a dose of $500\mu C/cm^2$ was used in one sample and $1000\mu C/cm^2$ in the other. After exposure, all samples were developed in a MF-319 solution for 60 seconds, rinsed in deionised water for another 60 seconds and blow-dried under a nitrogen flux. The RIE process was then performed using O_2 in a Plassys MEB400 at 20 mTorr and 100 W for two minutes in the first step, and then using O_2 and SF_6 at 4 mTorr and 80 W for two minutes in the second step.

We also observe that the nominal diameter of the pillars is slightly increased but that the period is mainteined. Although both, Al and Cr, could be use as etching masks, it was the latter one which allowed a longer etch time and better-defined features.

In Fig. 28 we present SEM images of a fabricated single layer sample using HSQ after the e-beam lithography (left), and after the etching process (right). We observe that after etching, the exposure pattern has been lost due to over etching.

In out attempts to correct this problem, we investigated the use of tetrafluoromethane (CF_4) gas instead of Sf_6 in the RIE process. We also found that the problem of under etching remained. For the bilayer samples, two different doses were used for the EBL. With the lower dose, we were unable to achieve a good pattern definition in the EBL exposure, presumable due to the resist thickness. We found that the pattern definition improved with the increase of the dose, but this resulted in other issues caused by the scattering of electrons in the layer such as an electron backscattering effect.

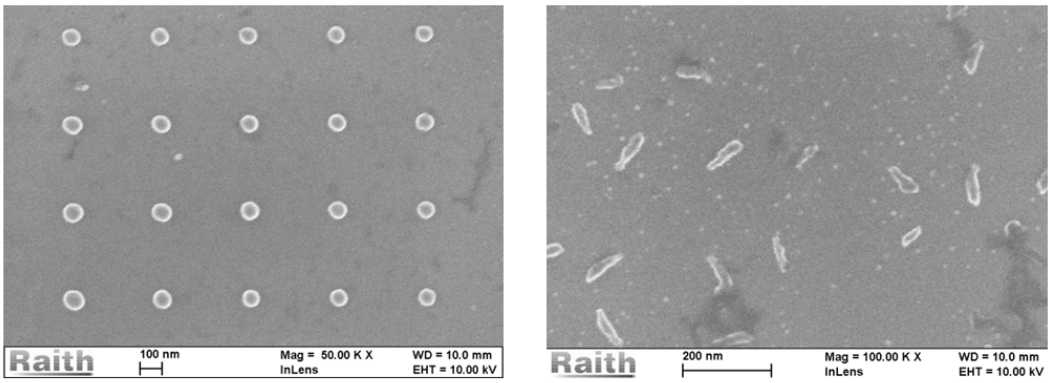

Figure 28: SEM images of a fabricated sample using HSQ single layer resist in the zone with a 100 nm **pillar diameter and** 400 nm **period. After the EBL (left), and after the etching process (right).**

5.1.2 Samples with a variable density of pillars

After these tests, it seemed that the best option was to use PMMA resist. Once we had determined the minimum period and feature size that we could reach, we focused our attention on the fabrication of samples with a variable density of pillars. Our aim was to determine the achievable range of pillar densities in nano-structured silicon. We present results for three samples:

- a slab waveguide of Si;
- a sample with a linear variation of pillar density;

- a sample with an exponential variation of pillar density.

To design the linear and the exponential samples, we first considered an area of the same size as the delimited region of the slab waveguide sample, and divided it into a square lattice whose period equals the pillar diameter. We fixed a density value of one to all the cells located at the edge of the sample that is connected with the integrated silicon waveguide, and a value of zero to the cells at the opposite edge of the sample, with one being the corresponding value for silicon and zero for air. The density variation along the samples was then numerically calculated as either linear or exponential. The discrete version of the calculated density map, and thus the specific recipe of where to put the pillars, was determined by means of the dithering algorithm explained in Sec. 3.2.1.

From the results obtained in our first tests, we decided to fabricate the samples with a 150 nm diameter pillars using a PMMA resist and a Cr mask. The periods range from 500 nm in the regions with a low pillar density, to contiguous pillars with periods of 200 nm in the higher density region. The three samples were designed with an integrated waveguide to illuminate them for further characterization (Fig.29). The homogeneous Si sample was proposed to explore the possibility of producing a design that could be the basis of an experimental integrated optics setup.

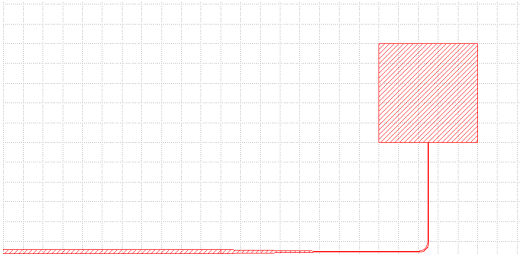

Figure 29: Image of the GDS file for the homogeneous silicon sample.

The fabrication process started by spin-coating a 200 nm PMMA layer on the wafers, rinsing them in isopropanol, blow-drying then under nitrogen flux and baking them on a hot plate at 180 °C for four minutes. After this, a 300Z espacer layer was spin-coated and rinsed with deionised water. For the homogeneous sample, an exposure dose of $140 \mu C/cm^2$ was used to defined its structure on the wafer. The EBL process for the samples with a density gradient was carried out in the same wafer, with the difference that

the electron dose was varied as a function of the local density of pillars. The subsequent SEM analysis reveled that the patterned features had a diameter of δ = 150 $\pm$ 15 nm in the zones of the samples with pillar densities ranging from medium to low. For the zones with a higher density of pillars, the definition was lost. After exposure, the samples were developed in a MIBK solution for 60 seconds, rinsed in isopropanol for 15 seconds and blow-dried under nitrogen flux. Following the development, a 40 nm layer of Cr was deposited on the samples. A lift-off process was performed by immersing the samples in acetone for two hours, and then placing them in an ultrasonic bath for ten minutes. No problems were observed in the homogeneous sample. However, after the lift-off, we observed that the samples with the density gradient of pillars had Cr residues. In our attempts to improve the situation, a second lift-off was carried out, in which the samples were immersed in acetone for two days, and placed later in an ultrasonic bath for ten minutes. We performed the etching process in a Plassys MEB400 using O_2 at a 2 mTorr pressure and a 100 W power for 60 seconds. Finally, since there were still many Cr residues in the density gradient samples, we placed them into a mixture made of four tablets of potassium hydroxide (KOH) dissolved in 40 ml of deionised water for several hours. However, the Cr residues remained in the zones of the samples with a higher density of pillars.

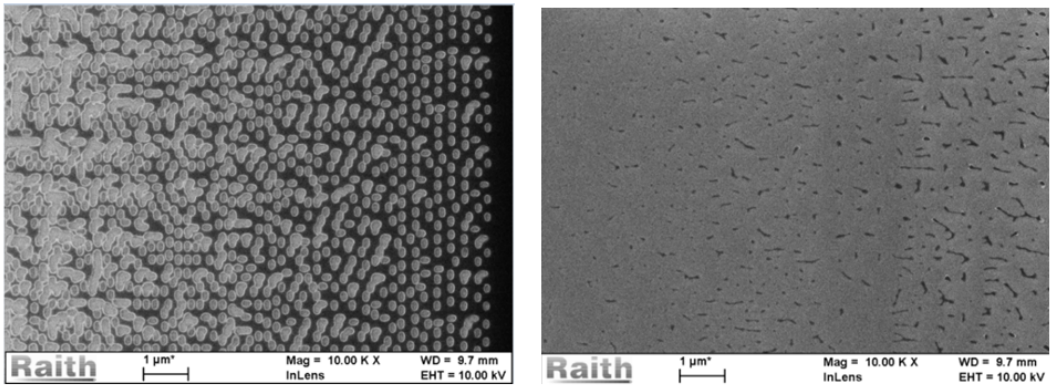

Figure 30: SEM images of the sample with an exponential variation of density after lithography. Zone with a low density of pillars (left). Zone with a high density of pillars (right).

Figure 31 shows the slab waveguide of silicon. In Fig. 30, a zoomed SEM image taken from the sample with the linear density gradient after the lithography step, shows the lack of definition in the zones with pillar densities ranging from medium to high. This appears

to be due to an exposure dose that was not well calibrated in its variation as a function of the density of pillars.

Figure 32 shows SEM images of the same fabricated sample after the chromium mask

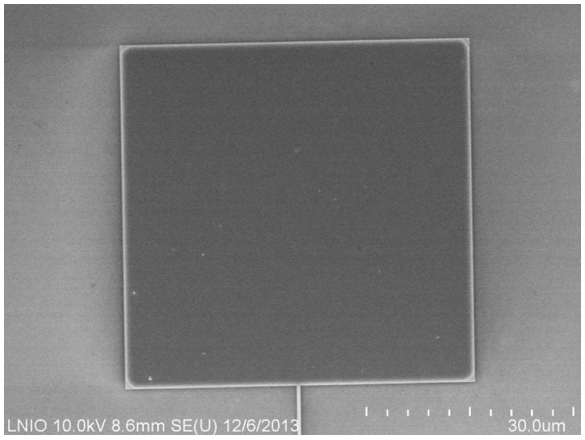

Figure 31: SEM image of the slab waveguide of silicon.

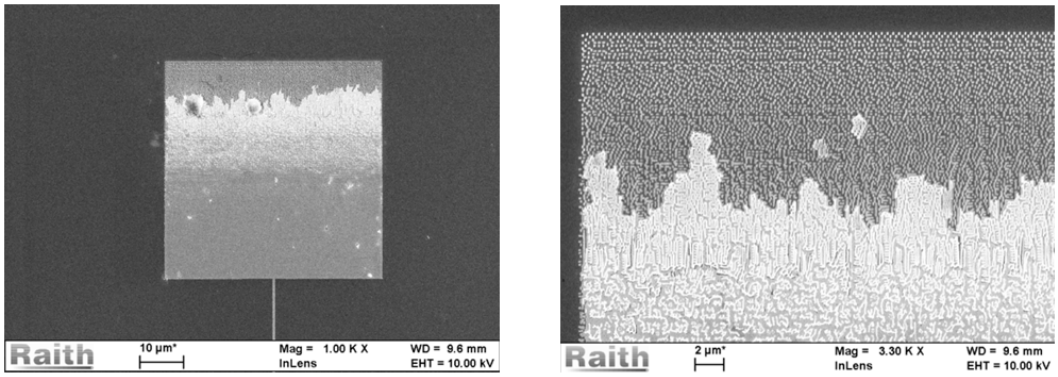

Figure 32: SEM images of the sample with a linear variation of density after the lift-off.

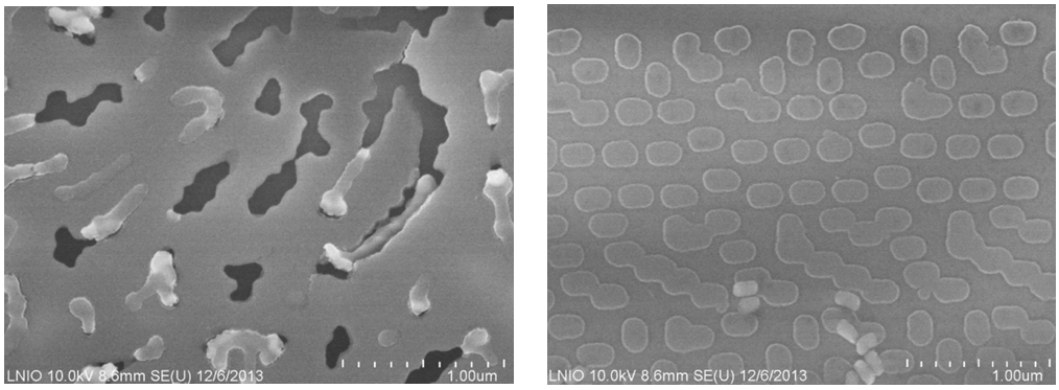

Figure 33: SEM images of the sample with an exponential variation of density after the RIE process. Zone with a low density of pillars (right). Zone with a high density of pillars (left).

deposition and lift-off. We observe that the zone with a low density of pillars (upper part of the sample) had a better feature definition compared to the one with a higher density (middle part). In the latter one, we see that the chromium mask was not removed.

In Fig. 33 we see the SEM images of the same sample as that of Fig. 30 after the RIE process. We observe that the exposure pattern has been deformed in the medium and high density zones, and that there is no silicon at the lower density zone. In some areas of the low pillar density region (upper part of the sample), it is observed that the silicon has been completely etched. We then assume that the chromium mask has been lifted-off in some of the resist holes, as a result of the increase in the time of the lift-off process, and thus it did not played its role protecting the samples during the RIE.

The experiments described were designed to investigate the achievable pillar density range in the samples fabricated with EBL with PMMA resist and a Cr mask. It was found that for the desired range, we could not control the exposure dose that will leaded to a good feature definition. In addition, the lift-off process was problematic and even after a secondary process, the majority of the area of our samples with medium or high density of pillars ended up with Cr residues.

Given the difficulties encountered with the HSQ resist in our first experiments, and the lift-off problems just described when the PMMA resist is used, we decided to try another negative resist (ma-N 2403). The ma-N 2400 resist has an excellent etch resistance and a high pattern resolution, and can be removed residue-free after the fabrication process. However, this resist requires special precautions like using yellow light and being allow to cool and stabilize when deposited, and a longer sample preparation. Next, besides optimizing the etching conditions, we proposed to limit ourselves to the fabrication of samples with a density of pillars that ensured a minimum center-to-center separation between neighboring pillars of two pillar diameters.

5.1.3 Fabrication of samples used for the optical experiments

After the described tests, we decided to fabricate three samples with simple structures that will allow us to test the accuracy of simple EMTs in the context of silicon nano-

structured layers at telecommunications wavelengths. The samples were fabricated in bulk silicon waffers using ma-N 2403 negative resist and have the following characteristics:

- A periodic sample with a uniform density of pillars, referred to as Sample A.
- A random sample with a uniform density of pillars, referred to as Sample B.
- A sample with isolated silicon pillars, referred to as Sample C.

The fabrication process started with three 1 cm $\times$ 1 cm squares of bulk silicon with a 500 µm height. The bulk silicon samples were immersed in acetone in an ultrasonic bath for 15 minutes, rinsed in isopropanol, blow-dried under a nitrogen flux, baked on a hot plate at 300 for 15 minutes, and allowed to cool and stabilize overnight. An hexamethyldisilazane (HMDS) primer layer was spin-coated on the samples under yellow light. We then deposited a ma-N 2400 resist layer and baked the samples in an oven at 80 °C for two minutes. After this, a 300Z espacer layer was spin-coated on them, and rinsed with deionised water.

The EBL was carried out in a 100 µm $\times$ 100 µm area in a Raith system using a $26\mu C/cm^2$ dose in Sample A and Sample B, and a $175\mu C/cm^2$ dose in Sample C. After exposure, all samples were developed in a solution made by combining equal quantities of ma-D 525 developer and deionised water for 60 seconds, rinsed in deionised water for another three minutes, and blow-dried under a nitrogen flux. Following the development, the samples were baked in a oven at 100 °C for ten minutes. The final RIE process was performed in a Plassys MEB400 using O_2 and SF_6 at $2x10^{-}5$ Torr and 90 W for three minutes in the first step, and O_2 with the same parameters for one minute in the second step.

In all cases, the pillars were designed to have a nominal pillar diameter of 150 nm. For the Sample A, we chose a period of 450 nm, and for Sample C a period of 3450 nm. On the basis of our previous experiments, the desired parameters should be achievable with the procedures described and the available system.

To design the random sample (Sample B) we first considered an area of the same size as the structured region of the periodic sample, and divided it into a square lattice whose period equals the pillar diameter. Then, two uncorrelated random integers ξ_i were

drawn from a uniform distribution on the interval $[1, \mathcal{N}]$ where $\mathcal{N}$ is the number of cells in each direction of the lattice. If the cell labeled (ξ_1, ξ_2) was not occupied and neither are their nearest neighbors, then a pillar was placed at the center of the cell (ξ_1, ξ_2). This procedure was repeated until the number of pillars placed equaled the numbers of pillars in the periodic sample. Note that for samples produced in this way the minimum center-to-center separation between neighboring pillars is two pillar diameters (or 300 nm for the radius assumed here).

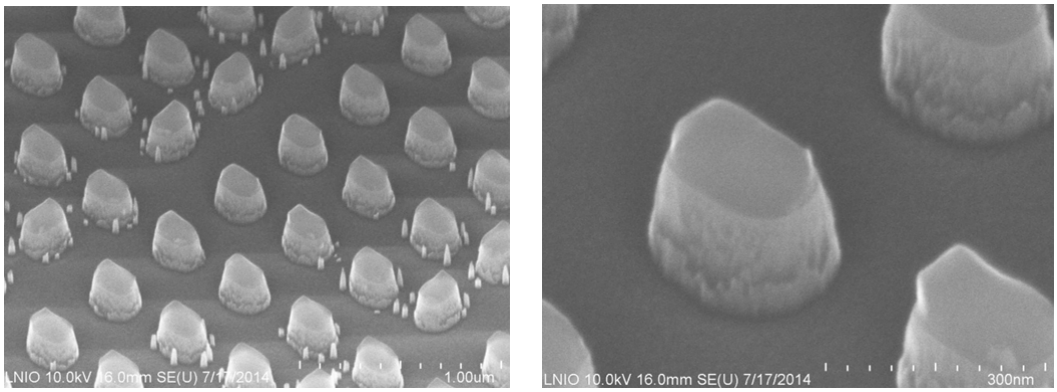

Figure 34: SEM images of the Sample A after the etching process from far (left), and in zoom (right).

Figures 34, 35 and 36 present SEM images of Samples A, B and C, respectively. One observes that the fabricated nanopillars have a lager cross section area at the base than at the top (Fig. 34).

By analyzing SEM images of Sample A, (those in Fig. 34 and other images taken from different angles and magnifications) it was found that the pillars have a shape that can be approximated by a truncated cone with approximate top and base radii $\rho_t = 85 \pm 5$ nm and $\rho_b = 105 \pm 10$ nm, respectively. The structure was measured to have a nominal period of $a = 450 \pm 5$ nm, and the height of the pillars was found to be $\zeta_0 = 190 \pm 5$ nm. It should be mentioned that due to the discretization of the ideal positions, Sample A showed some undesired features; the distance between pillars ended up having periodic variations and the cross section of the pillars was not quite circular. These issues are visible in the SEM image presented on the left of Fig. 34.

For Sample B, the SEM images revealed that the top and base radii were, respectively,

$\rho_t = 85 \pm 5$ nm and $\rho_b = 110 \pm 10$ nm, while their height was found to be $\zeta_0 = 165 \pm 5$ nm. The measured minimum distance between neighboring pillars was about 300 nm, which is in good agreement with the design parameters.

For Sample C, on the other hand, the SEM images revealed that the top and base radii were, respectively, $\rho_t = 75 \pm 5$ nm and $\rho_b = 90 \pm 10$ nm, while their height was found to be $\zeta_0 = 165 \pm 5$ nm. The measured period was about 3450 nm, which is in good agreement with the design parameters.

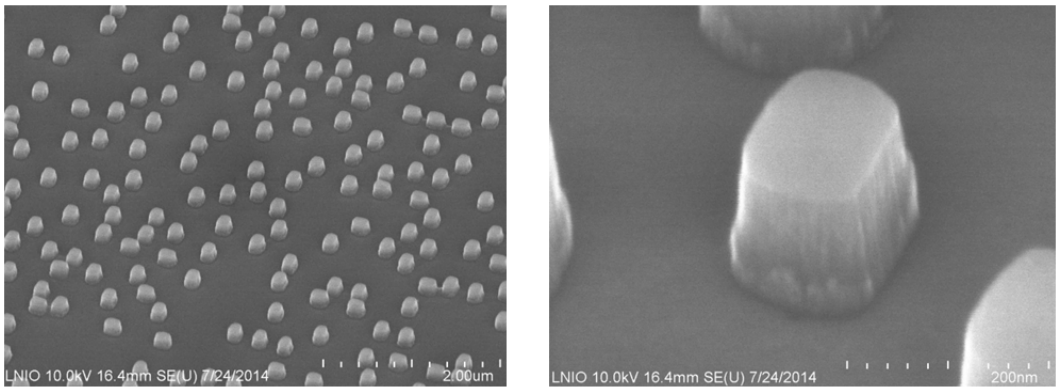

Figure 35: SEM images of the Sample B in the zone after the etching process. Wide field view (left), and zoomed image showing a pillar (right).

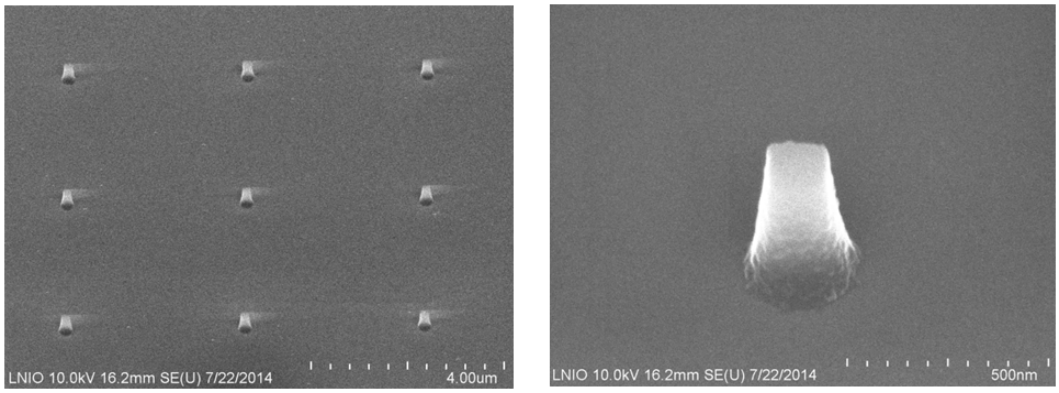

Figure 36: SEM images of the Sample C in the zone after the etching process. Wide field view (left), and zoomed image showing a pillar (right).

5.2 Reflectivity measurements

To explore the effective medium properties of nanostructured silicon layers at telecommunication wavelengths, we decided to carry out reflectivity measurements focusing on two of Sample A and Sample B.

A schematic diagram of the optical setup employed to carry out the measurements is shown in Fig.37. A Thorlabs IR laser diode with a (λ = 1.55 µm) wavelength and a 5 mW power was used to generate a beam that passed through a linear polarizer and then through a chopper. After this, the beam was focused with a lens onto a mirror that reflected the light at near normal incidence to illuminate the sample. The light reflected by the sample was then collected by a lens and focused to a Thorlabs detector (883 nm - IR).

The samples were illuminated at near normal incidence [$\theta_0 \approx 2$ mrad $\approx 1.15^\circ$] by a linearly polarized beam of light from a laser of wavelength λ = 1.55 µm (Thorlabs LDM1550). A small angle of incidence was used to avoid the use of a beamsplitter in the measurements. The beam was focussed on the sample with a low power lens, and the reflected light was measured in the specular direction using a collecting lens and an InGaAs detector (Thorlabs DET20C). The contribution from the back surface of the sample was reduced by roughening it slightly and putting it in optical contact with an absorbing paste. Several readings of the optical power reflected from a given spot of the sample were averaged to obtain a measurement, that was later normalized by the signal produced by the flat areas of the sample (the reflectivity of these flat regions was in good agreement with that expected for a flat silicon surface).

The reflectivities of Samples A and B were measured to be $R_A = 0.2227 \pm 0.0032$ and $R_B = 0.2350 \pm 0.0049$, respectively. These estimated reflectivity values represent the mean and standard deviation calculated from ten measurements that correspond to different areas of the structured region of the samples.

Taking the value of the dielectric constant of silicon at the wavelength of the incident light to be ϵ = 12.25, the Fresnel reflectivity for the planar silicon substrate is $R_0 \approx 0.3086$. These reflectivities are both significantly smaller than what is expected for a planar silicon substrate.

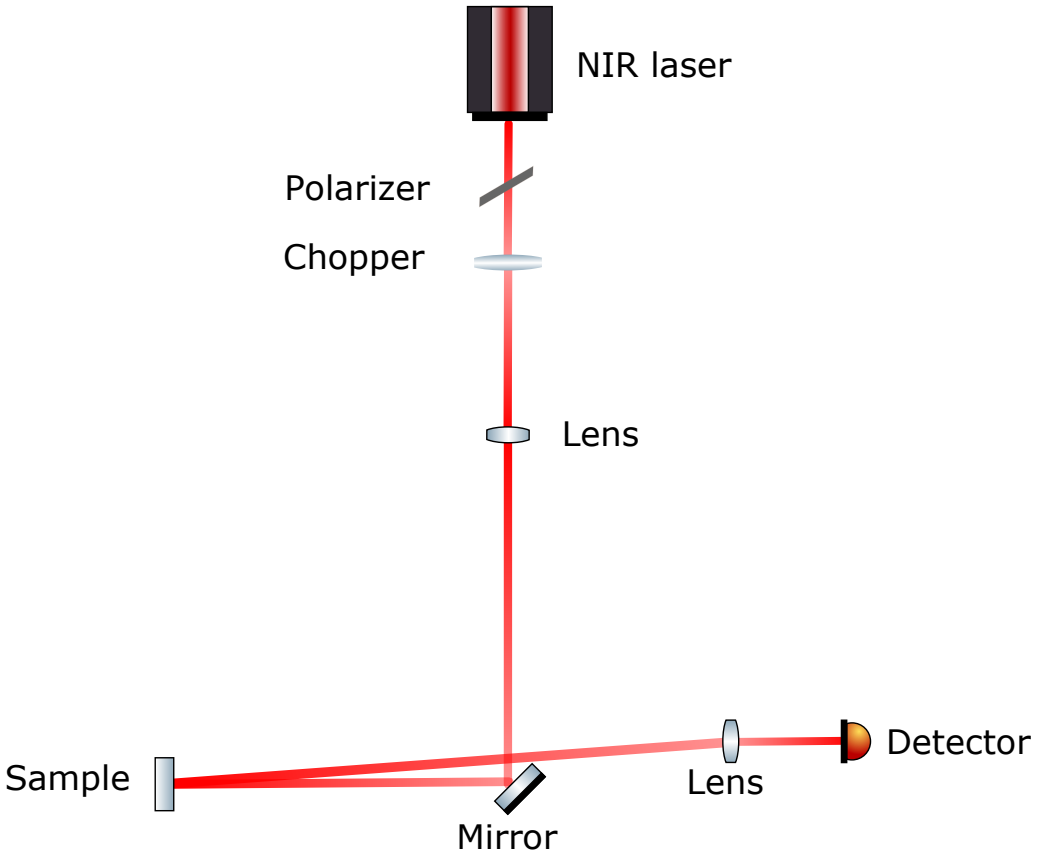

Figure 37: Schematic image of the experimental setup.

5.3 Three-layer model

Since the structures that we consider have lateral dimensions that are much smaller than the wavelength of the incident light, it is natural to assume that, in this long wavelength limit, the layer containing the surface irregularities can be modeled as a homogeneous film of thickness $h = \zeta_0$ with an *effective* dielectric constant $\epsilon_{\rm eff}$ (Choy, 1999). The reflectivity of the system can then be calculated using the reflection coefficient of a layered system (Fig.(38)). For the the case of a thin film over a substrate (three-media or three-layer

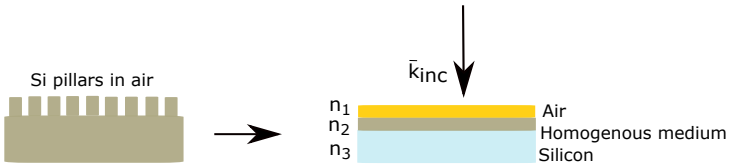

Figure 38: Schematic of the three layer model applied to our fabricated structures.

system), one has (Born and Wolf, 1970)

$$r = \frac{r_{12} + r_{23}\exp(2i\beta)}{1 + r_{12}r_{23}\exp(2i\beta)}, \tag{91}$$

where the subscripts 1, 2 and 3 refer to vacuum, the thin film of the effective medium, and the substrate, respectively; r_{ij} (with $i, j = 1, 2, 3$) represents the reflection amplitude of the interface between medium i and j; and β denotes the optical path length for the light in the film. For the case of normal incidence, we can write

$$r_{ij} = \frac{n_i - n_j}{n_i + n_j}, \tag{92}$$

and

$$\beta = n_2 \frac{\omega}{c} h, \tag{93}$$

where $n_i = \sqrt{\epsilon_i}$ represents the refractive index of medium i. The reflectivity of the system is therefore given by

$$R = |r|^2 = \frac{r_{12}^2 + r_{23}^2 + 2r_{12}r_{23}\cos 2\beta}{1 + r_{12}^2 r_{23}^2 + 2r_{12}r_{23}\cos 2\beta}. \tag{94}$$

The effective refractive index of the film, $n_{eff} = \sqrt{\epsilon_{\rm eff}}$, may then be estimated assuming

a three-media model, to invert the reflectivity data obtained experimentally, or through rigorous computer simulations. The result obtained in this way can be compared with estimations based on the effective medium theories, like the Maxwell Garnett theory, which has been used previously in the context of silicon photonics systems (Gabrielli and Lipson, 2011). This permits the evaluation of the validity of effective medium theories for the estimation of the effective refractive index of a layer of supported silicon nanopillars.

For the samples that we study the host medium is air, which has a permittivity $\epsilon_1 = 1$, and the inclusions are silicon, for which $\epsilon_2 = 12.25$. The filling fraction, defined as the ratio of the volume of inclusion to the volume of host material, was found to be $f = 0.14$ for the parameters of Sample A given in the preceding Section. To calculate the filling fraction of the periodic sample, we considered a unit cell of sides a, the period of our structures, with an embedded truncated cone of base radius ρ_b and top radius ρ_t. The volume filling fraction is then given by the ratio of the volume of the truncated cone to the volume of the cell. Since the average density of the pillars is the same in the two samples, the filling fraction of Sample B is the same as the filling fraction of Sample A.

With these values for ϵ_1, ϵ_2 and f, the 3D Maxwell Garnett (MG) approach from Eq. (85) predicts that the effective medium should have a dielectric constant $\epsilon_{\text{eff}} = 1.374$. Using this value of ϵ_{eff}, and assuming that the wavelength of the incident light is $\lambda = 1.55\,\mu\text{m}$, on the basis of Eq. (94), we estimate that the reflectivities of Samples A and B are 0.2626 and 0.2721, respectively. These values are considerably larger than those obtained experimentally.

We can try to fit the experimental findings using other effective medium theories (EMTs), like those described in Chapter 4. For the 2D MG approach, the calculated effective permittivity is $\epsilon_{\text{eff}} = 1.27$ for the same filling fraction of $f = 0.14$ and the estimated values for the reflectivities of samples A and B are 0.2346 and 0.2499, respectively. Although these values are closer, they still differ from the experimental ones.

Under the 3D Bruggeman approach, the calculated effective permittivity is $\epsilon_{\text{eff}} = 1.17$ for the same filling fraction $f = 0.14$ that we used with the MG theory, and the estimated values for the reflectivities are 0.2758 and 0.2825 for samples A and B, respectively. With

the 2D approach, the effective permittivity is $\epsilon_{\text{eff}} = 1.30$, and the corresponding reflectivities for samples A and B are 0.2514 and 0.2631.

Thus, we have found that the reflectivity estimated for our structures by means of the EMTs overestimates the values obtained experimentally. We now turn to more accurate ways for calculating the reflectivity of our samples, namely the reduced Rayleigh equation (RRE) and the Fourier modal method (FMM). In the next Chapter we describe these approaches.

Chapter 6 Theoretical methods

Despite the possibilities offered by transformation optics in combination with silicon photonics, a literature survey reveals that the practical success of the approach has been limited by the challenging fabrication requirements and the difficult theoretical modeling, among other things. The accuracy of the effective refractive index theories employed by some authors to deal with nanostructured silicon (Gabrielli and Lipson, 2011) had not been tested for the kind of geometries and refractive index contrast of the samples fabricated in this work.

In the preceding section, it was found that the reflectivity estimated for our structures, by means of effective medium theories (EMTs), did not agree with the reflectivity obtained experimentally. Thus, in this Chapter we turned to more accurate ways of calculating the reflectivity of our samples as a function of the height of the pillars, namely (i) the reduced Rayleigh equation (RRE) and (ii) the Fourier modal method (FMM). We did two sets of simulations based on these methods. The simulations performed with the former method used an in-house developed code. The FMM/RCWA simulations used the publicly available code called S^4 (*Stanford Stratified Structure Solver*) (Liu and Fan, 2012). These approaches will now be described.

6.1 The reduced Rayleigh equation

An estimation of the effective refractive index of nanostructured surfaces, with an emphasis on the case of silicon nanopillars on a substrate, can be given theoretically and experimentally by the scattering of light from them. The scattering of electromagnetic waves from such a surface can be calculated by the Rayleigh method. By means of the Rayleigh hypothesis (Maradudin, 2007) and the use of the boundary conditions satisfied by the electromagnetic fields on the interface (Jackson, 2007), it is possible to obtain a coupled set of inhomogenious integral equations for the scattering and transmission amplitudes. This equation is know as the Rayleigh equation and it depends on the surface profile function that the scattering geometry consists of. The Rayleigh equation is rigorous as long as the Rayleigh hypothesis is satisfied, but the validity of this hypothesis is only known for

a few periodic surface structures (Millar, 1971; Hill and Celli, 1978). For a general rough surface it is not known for which roughness parameters the Rayleigh hypothesis is valid. In such cases, a method based on the Rayleigh equation should therefore be considered as an approximate method.

In the fist half of the 1980s, it was demonstrated that some of the Rayleigh equations can be eliminated, resulting in a smaller set of modified integral equations known nowadays as the *reduced Rayleigh equation* (RRE) (Brown *et al.*, 1984). The RRE is a single inhomogenious matrix integral equation for either the scattering amplitude or the transmission amplitude, but not both. This equation allows for the calculation of the field scattered from rough or periodic surfaces. The RRE for such scattering geometries can not be solved analytically so numerical technique has to be applied to obtain its solution. The first purely numerical solution of the RRE for a two dimensionally randomly rough interface was recently performed (Nordam *et al.*, 2013). Other works based on the RRE for two dimensional geometries include those of Soubret and coworkers for a film of finite thickness on top of an infinitely thick substrate with one rough interface (Soubret *et al.*, 2001), the one of Nordam and coworkers for reflection from perfectly conducting two dimensional randomly rough surfaces (Nordam *et al.*, 2014), and that of Hetland et al. for transmission through clean penetrable two dimensional surfaces (Hetland *et al.*, 2016).

It ought to be mentioned that most of the perturbative approaches to the scattering and transmission of light through rough surfaces can be derived starting from the RRE. However, a non-perturbative numerical solution of the RREs naturally includes the effect of multiple scattering processes underlying, for instance, the enhanced backscattering phenomenon (Simonsen, 2010).

The system we consider consists of vacuum in the region $x_3 > \zeta\left(\mathbf{x}_{\|}\right)$ and a scattering medium, characterized by a dielectric function $\epsilon(\omega)$, in the region $x_3 < \zeta\left(\mathbf{x}_{\|}\right)$. The vector $\mathbf{x}_{\|} = (x_1, x_2, 0)$ is an arbitrary position vector in the plane $x_3 = 0$. The surface profile function, $\zeta(\mathbf{x}_{\|})$, is assumed to be a single-valued function of $\mathbf{x}_{\|}$ that is differentiable with respect to x_1 and x_2. If the dielectric function $\epsilon(\omega)$ is independent of the (angular) frequency ω and is real and positive, the scattering medium is a dielectric. On the other hand, if the function $\epsilon(\omega)$ is frequency dependent and complex, with a negative real part and a positive

imaginary part, the scattering medium is a lossy metal.

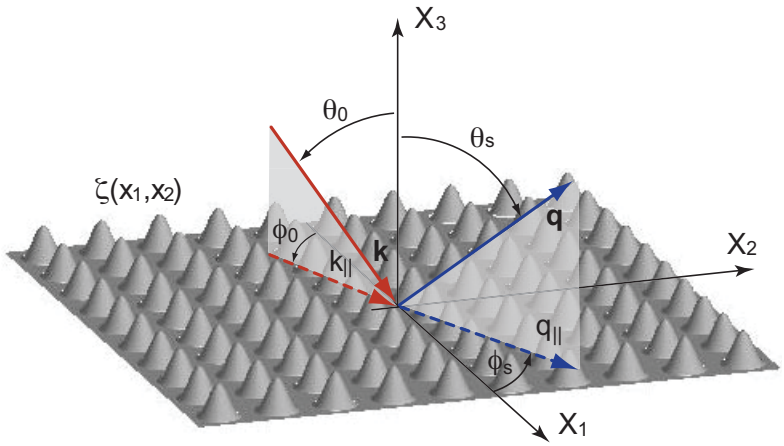

Figure 39: Schematic illustration of the considered scattering geometry. The angles of incidence (θ_0, ϕ_0) and angles of scattering (θ_s, ϕ_s) are defined explicitly. The corresponding lateral wave vectors of incidence and scattering are denoted $\mathbf{k}_\parallel$ and $\mathbf{q}_\parallel$, respectively, and indicated in the figure.

The interface $x_3 = \zeta\left(\mathbf{x}_\parallel\right)$ is illuminated from the vacuum by a plane wave of frequency ω. The total electric field in the vacuum region $x_3 > \max\zeta\left(\mathbf{x}_\parallel\right)$ can then be written as the sum of an incident and a scattered field, $\mathbf{E}\left(\mathbf{x};t\right) = \left[\mathbf{E}^{(i)}\left(\mathbf{x}|\omega\right) + \mathbf{E}^{(s)}\left(\mathbf{x}|\omega\right)\right]\exp\left(-i\omega t\right)$ where

$$\mathbf{E}^{(i)}\left(\mathbf{x}|\omega\right) = \left\{\frac{c}{\omega}\left[\alpha_0\left(k_\parallel\right)\widehat{\mathbf{k}}_\parallel + k_\parallel\widehat{\mathbf{x}}_3\right]E_{0p}(\mathbf{k}_\parallel) + \left[\widehat{\mathbf{k}}_\parallel \times \widehat{\mathbf{x}}_3\right]E_{0s}(\mathbf{k}_\parallel)\right\} \times \exp\left[i\mathbf{k}_\parallel\cdot\mathbf{x}_\parallel - i\alpha_0(k_\parallel)x_3\right] \tag{95a}$$

and

$$\mathbf{E}^{(s)}\left(\mathbf{x}|\omega\right) = \int\frac{d^2q_\parallel}{(2\pi)^2}\left\{\frac{c}{\omega}\left[-\alpha_0(q_\parallel)\widehat{\mathbf{q}}_\parallel + q_\parallel\widehat{\mathbf{x}}_3\right]A_p(\mathbf{q}_\parallel) + \left[\widehat{\mathbf{q}}_\parallel \times \widehat{\mathbf{x}}_3\right]A_s(\mathbf{q}_\parallel)\right\} \times \exp\left[i\mathbf{q}_\parallel\cdot\mathbf{x}_\parallel + i\alpha_0(q_\parallel)x_3\right]. \tag{95b}$$

In these expressions $\mathbf{q}_\parallel = (q_1, q_2, 0)$ is a two-dimensional wave vector, a caret over a vector indicates that it is a unit vector, and

$$\alpha_0(q_\parallel) = \left[\left(\frac{\omega}{c}\right)^2 - q_\parallel^2\right]^{\frac{1}{2}}, \qquad \mathrm{Re}\,\alpha_0(q_\parallel) > 0,\ \mathrm{Im}\,\alpha_0(q_\parallel) > 0. \tag{96}$$

Moreover, $E_{0p}(\mathbf{k}_\parallel)$ and $E_{0s}(\mathbf{k}_\parallel)$ are the amplitudes of the p- and s- polarized components of the incident electric field with respect to the plane of incidence, while $A_p(\mathbf{q}_\parallel)$ and $A_s(\mathbf{q}_\parallel)$

are the amplitudes of the p- and s- polarized components of the scattered electric field with respect to the local plane of scattering, respectively.

The expressions for the magnetic fields are obtained from the expressions for the corresponding electric field by the use of Faraday's law $\boldsymbol{\nabla} \times \mathbf{E} = i(\omega/c)\mathbf{H}(\mathbf{x}|\omega)$, here assuming Gaussian-cgs units and a non-magnetic medium. In this way, with Eq. (95), we obtain the expression for the incident magnetic field

$$\mathbf{H}^{(i)}(\mathbf{x}|\omega) = \left\{\frac{c}{\omega}\left[\mathbf{k}_{\parallel} - \alpha_0(k_{\parallel})\widehat{\mathbf{x}}_3\right]\right\} \times \left\{\frac{c}{\omega}\left[\alpha_0(k_{\parallel})\widehat{\mathbf{k}}_{\parallel} + k_{\parallel}\widehat{\mathbf{x}}_3\right] E_{0p}(\mathbf{k}_{\parallel}) + \left[\widehat{\mathbf{k}}_{\parallel} \times \widehat{\mathbf{x}}_3\right] E_{0s}(\mathbf{k}_{\parallel})\right\} \times \exp\left[i\mathbf{k}_{\parallel} \cdot \mathbf{x}_{\parallel} - i\alpha_0(k_{\parallel})x_3\right], \tag{97a}$$

and the magnetic scattered field

$$\mathbf{H}^{(s)}(\mathbf{x}|\omega) = \int \frac{d^2q_{\parallel}}{(2\pi)^2} \left\{\frac{c}{\omega}\left[\mathbf{q}_{\parallel} + \alpha_0(q_{\parallel})\widehat{\mathbf{x}}_3\right]\right\} \times \left\{\frac{c}{\omega}\left[-\alpha_0(q_{\parallel})\widehat{\mathbf{q}}_{\parallel} + q_{\parallel}\widehat{\mathbf{x}}_3\right] A_p(\mathbf{q}_{\parallel}) + \left[\widehat{\mathbf{q}}_{\parallel} \times \widehat{\mathbf{x}}_3\right] A_s(\mathbf{q}_{\parallel})\right\} \times \exp\left[i\mathbf{q}_{\parallel} \cdot \mathbf{x}_{\parallel} + i\alpha_0(q_{\parallel})x_3\right]. \tag{97b}$$

These magnetic fields, like the corresponding electric fields, are valid for $x_3 > \max \zeta(\mathbf{x}_{\parallel})$.

One may also write down expressions for the transmitted electric and magnetic fields, $\mathbf{E}^{(t)}(\mathbf{x}|\omega)$ and $\mathbf{H}^{(t)}(\mathbf{x}|\omega)$, respectively, that are valid for $x_3 < \min \zeta(\mathbf{x}_{\parallel})$. Such expressions will not be given here but they can be found in *e.g.* Ref. (Hetland *et al.*, 2016).

By imposing the Rayleigh hypothesis (Rayleigh, 1907), the forms of the fields given by Eqs. (95) and (97) in the vacuum region and the corresponding expressions for the transmitted fields in the region below the rough interface, can be used to satisfy the usual boundary condition on $x_3 = \zeta(\mathbf{x}_{\parallel})$ (Jackson, 2007). This will result in the *Rayleigh equation* which represents a coupled set of inhomogeneous integral equations where the unknowns are the amplitudes $A_p(\mathbf{q}_{\parallel})$ and $A_s(\mathbf{q}_{\parallel})$ of the scattered electric field and the similar amplitudes for the transmitted electric field. In 1984, Brown *et al.* (Brown *et al.*, 1984) showed that one set of field amplitudes can be eliminated to produce the *reduced Rayleigh equation* for either reflection or transmission. The former of these equations can be written in

the form (Nordam *et al.*, 2013; Hetland *et al.*, 2016)

$$\int \frac{d^2q_\parallel}{(2\pi)^2}\, \frac{I\left(\alpha(p_\parallel)-\alpha_0(q_\parallel)|\mathbf{p}_\parallel-\mathbf{q}_\parallel\right)}{\alpha(p_\parallel)-\alpha_0(q_\parallel)}\mathbf{M}(\mathbf{p}_\parallel|\mathbf{q}_\parallel)\mathbf{A}(\mathbf{q}_\parallel) = -\frac{I\left(\alpha(p_\parallel)+\alpha_0(k_\parallel)|\mathbf{p}_\parallel-\mathbf{k}_\parallel\right)}{\alpha(p_\parallel)+\alpha_0(k_\parallel)}\mathbf{N}(\mathbf{p}_\parallel|\mathbf{k}_\parallel)\mathbf{E}_0(\mathbf{k}_\parallel), \tag{98}$$

where $\mathbf{p}_\parallel$ denotes an arbitrary lateral wave vector, and

$$\mathbf{A}(\mathbf{q}_\parallel) = \begin{bmatrix} A_p(\mathbf{q}_\parallel) \\ A_s(\mathbf{q}_\parallel) \end{bmatrix} \qquad \mathbf{E}_0(\mathbf{q}_\parallel) = \begin{bmatrix} E_{0p}(\mathbf{q}_\parallel) \\ E_{0s}(\mathbf{q}_\parallel) \end{bmatrix}. \tag{99}$$

In writing Eq. (98) we have defined the functions

$$I\left(\gamma|\mathbf{Q}_\parallel\right) = \int d^2x_\parallel\, \exp\left(-i\mathbf{Q}_\parallel\cdot\mathbf{x}_\parallel\right)\exp\left[-i\gamma\zeta(\mathbf{x}_\parallel)\right], \tag{100}$$

$$\alpha(q_\parallel) = \left[\epsilon(\omega)\left(\frac{\omega}{c}\right)^2 - q_\parallel^2\right]^{\frac{1}{2}}, \qquad \operatorname{Re}\alpha(q_\parallel) > 0,\ \operatorname{Im}\alpha(q_\parallel) > 0, \tag{101}$$

and the matrix elements

$$\mathbf{M}(\mathbf{p}_\parallel|\mathbf{q}_\parallel) = \begin{bmatrix} p_\parallel q_\parallel + \alpha(p_\parallel)\,\widehat{\mathbf{p}}_\parallel\cdot\widehat{\mathbf{q}}_\parallel\,\alpha_0(q_\parallel) & -\left(\frac{\omega}{c}\right)\alpha(p_\parallel)\left[\widehat{\mathbf{p}}_\parallel\times\widehat{\mathbf{q}}_\parallel\right]_3 \\ \left(\frac{\omega}{c}\right)\left[\widehat{\mathbf{p}}_\parallel\times\widehat{\mathbf{q}}_\parallel\right]_3\alpha_0(q_\parallel) & \left(\frac{\omega}{c}\right)^2\widehat{\mathbf{p}}_\parallel\cdot\widehat{\mathbf{q}}_\parallel \end{bmatrix} \tag{102a}$$

and

$$\mathbf{N}(\mathbf{p}_\parallel|\mathbf{q}_\parallel) = \begin{bmatrix} p_\parallel q_\parallel - \alpha(p_\parallel)\,\widehat{\mathbf{p}}_\parallel\cdot\widehat{\mathbf{q}}_\parallel\,\alpha_0(q_\parallel) & -\left(\frac{\omega}{c}\right)\alpha(p_\parallel)\left[\widehat{\mathbf{p}}_\parallel\times\widehat{\mathbf{q}}_\parallel\right]_3 \\ -\left(\frac{\omega}{c}\right)\left[\widehat{\mathbf{p}}_\parallel\times\widehat{\mathbf{q}}_\parallel\right]_3\alpha_0(q_\parallel) & \left(\frac{\omega}{c}\right)^2\widehat{\mathbf{p}}_\parallel\cdot\widehat{\mathbf{q}}_\parallel \end{bmatrix}. \tag{102b}$$

Equation (98) is the reduced Rayleigh equation (for reflection) that relates the amplitudes $A_\nu(\mathbf{q}_\parallel)$ of the scattered field to the amplitudes $E_{0\nu'}(\mathbf{k}_\parallel)$ of the incident field for $\nu, \nu' = p, s$. It is worth noticing from Eqs. (98)–(102) that the surface profile function $\zeta(\mathbf{x}_\parallel)$ only enters in the expression for $I\left(\gamma|\mathbf{Q}_\parallel\right)$. Hence, it is this function that encodes the form of the surface profile function that is assumed.

In the following, our main concerned will be surface profile functions $\zeta(\mathbf{x}_\parallel)$ that are doubly periodic functions of $\mathbf{x}_\parallel$ and characterized by the lattice parameter a. We express

this by writing

$$\zeta\left(\mathbf{x}_{\parallel}+\mathbf{x}_{\parallel}(\ell)\right)=\zeta\left(\mathbf{x}_{\parallel}\right), \tag{103}$$

where $\{\mathbf{x}_{\parallel}(\ell)\}$ are the translation vectors of a two-dimensional Bravais lattice. They are expressed by

$$\mathbf{x}_{\parallel}(\ell)=\ell_1\mathbf{a}_1+\ell_2\mathbf{a}_2, \tag{104}$$

where $\mathbf{a}_1$ and $\mathbf{a}_2$ are the two noncollinear primitive translation vectors of the lattice, while ℓ_1 and ℓ_2 are any positive or negative integers, or zero, which we denote collectively by $\ell=(\ell_1,\ell_2)$. The area of a primitive unit cell of this lattice is $a_c=|\mathbf{a}_1\times\mathbf{a}_2|$. In this work our main concern will be a square lattice for which $\mathbf{a}_1=a\,\widehat{\mathbf{x}}_1$ and $\mathbf{a}_2=a\,\widehat{\mathbf{x}}_2$.

It will be convenient for what follows to introduce the lattice that is reciprocal to the one defined by Eq. (104). Its lattice sites are given by

$$\mathbf{G}_{\parallel}(\mathbf{h})=h_1\mathbf{b}_1+h_2\mathbf{b}_2, \tag{105}$$

where the primitive translation vectors of this lattice are defined by the equations

$$\mathbf{a}_i\cdot\mathbf{b}_j=2\pi\delta_{ij}\qquad i,j=1,2, \tag{106}$$

with δ_{ij} denoting the Kronecker symbol. In Eq. (105), h_1 and h_2 are any positive or negative integers, or zero, which we denote collectively by $\mathbf{h}$. For a square lattice of parameter a the primitive reciprocal lattice vectors are $\mathbf{b}_1=(2\pi/a)\,\widehat{\mathbf{x}}_1$ and $\mathbf{b}_2=(2\pi/a)\,\widehat{\mathbf{x}}_2$.

Due to the periodicity of the surface profile function (Fig. 39), $\zeta(\mathbf{x}_{\parallel})$ the electric field in the vacuum must satisfy the Floquet-Bloch condition (Russell, 1985), *i.e.*

$$\mathbf{E}\left(\mathbf{x}_{\parallel}+\mathbf{x}_{\parallel}(\ell),x_3|\omega\right)=\exp\left[i\mathbf{k}_{\parallel}\cdot\mathbf{x}_{\parallel}(\ell)\right]\mathbf{E}\left(\mathbf{x}_{\parallel},x_3|\omega\right). \tag{107}$$

Consequently, we rewrite the amplitudes $A_\nu(\mathbf{q}_\parallel)$ of the scattered electric field in the form

$$A_\nu(\mathbf{q}_\parallel) = \sum_{\mathbf{G}_\parallel} (2\pi)^2\, \delta\left(\mathbf{q}_\parallel - \mathbf{k}_\parallel - \mathbf{G}_\parallel\right) a_\nu(\mathbf{k}_\parallel + \mathbf{G}_\parallel), \qquad \nu = p, s. \tag{108}$$

In writing Eq. (108) we have replaced summation over $\mathbf{h}$ by summation over $\mathbf{G}_\parallel$. For a periodic surface, we write Eq. (100) in the form

$$I\left(\gamma|\mathbf{Q}_\parallel\right) = \sum_{\ell} \int\limits_{a_c(\ell)} d^2x_\parallel \, \exp\left(-i\mathbf{Q}_\parallel \cdot \mathbf{x}_\parallel\right) \exp\left[-i\gamma\zeta(\mathbf{x}_\parallel)\right], \tag{109}$$

make the change of variable $\mathbf{x}_\parallel = \mathbf{x}_\parallel(\ell) + \mathbf{u}_\parallel$ and use the the periodicity property (103) of the surface to obtain

$$\begin{aligned} I\left(\gamma|\mathbf{Q}_\parallel\right) &= \sum_{\ell} \int\limits_{a_c} d^2x_\parallel \, \exp\left[-i\mathbf{Q}_\parallel \cdot \left(\mathbf{x}_\parallel(\ell) + \mathbf{u}_\parallel\right)\right] \exp\left[-i\gamma\zeta(\mathbf{u}_\parallel + \mathbf{x}_\parallel(\ell))\right] \\ &= \sum_{\ell} \exp\left[-i\mathbf{Q}_\parallel \cdot \mathbf{x}_\parallel(\ell)\right] \int\limits_{a_c} d^2u_\parallel \, \exp\left(-i\mathbf{Q}_\parallel \cdot \mathbf{u}_\parallel\right) \exp\left[-i\gamma\zeta(\mathbf{u}_\parallel)\right]. \end{aligned} \tag{110}$$

Now, taking advantage of the relation

$$\sum_{\ell} \exp\left[-i\mathbf{Q}_\parallel \cdot \mathbf{x}_\parallel(\ell)\right] = \sum_{\mathbf{G}_\parallel} \frac{(2\pi)^2}{a_c} \delta\left(\mathbf{Q}_\parallel - \mathbf{G}_\parallel\right), \tag{111}$$

enables us to write Eq. (110) in the form

$$I\left(\gamma|\mathbf{Q}_\parallel\right) = \sum_{\mathbf{G}_\parallel} (2\pi)^2\, \delta\left(\mathbf{Q}_\parallel - \mathbf{G}_\parallel\right) \widehat{I}\left(\gamma|\mathbf{G}_\parallel\right), \tag{112}$$

with

$$\widehat{I}\left(\gamma \mid \mathbf{G}_\parallel\right) = \frac{1}{a_c} \int\limits_{a_c} d^2x_\parallel \, \exp\left(-i\mathbf{G}_\parallel \cdot \mathbf{x}_\parallel\right) \exp\left[-i\gamma\zeta(\mathbf{x}_\parallel)\right]. \tag{113}$$

When the expansions (108) and (112) are substituted into Eq. (98), the equation satis-

fied by the amplitudes $\left\{a_{p,s}(\mathbf{k}_\parallel + \mathbf{G}_\parallel)\right\}$ is

$$\sum_{\mathbf{K}_\parallel} (2\pi)^2 \delta\left(\mathbf{p}_\parallel - \mathbf{K}_\parallel\right) \sum_{\mathbf{K}'_\parallel} \frac{\widehat{I}\left(\alpha(K_\parallel) - \alpha_0(K'_\parallel)\middle|\mathbf{K}_\parallel - \mathbf{K}'_\parallel\right)}{\alpha(K_\parallel) - \alpha_0(K'_\parallel)} \mathbf{M}\left(\mathbf{K}_\parallel|\mathbf{K}'_\parallel\right) \mathbf{a}(\mathbf{K}'_\parallel)$$
$$= -\sum_{\mathbf{K}_\parallel} (2\pi)^2 \delta\left(\mathbf{p}_\parallel - \mathbf{K}_\parallel\right) \frac{\widehat{I}\left(\alpha(K_\parallel) + \alpha_0(k_\parallel)\middle|\mathbf{K}_\parallel - \mathbf{k}_\parallel\right)}{\alpha(K_\parallel) + \alpha_0(k_\parallel)} \mathbf{N}\left(\mathbf{K}_\parallel|\mathbf{k}_\parallel\right) \mathbf{E}_0(\mathbf{k}_\parallel). \quad (114)$$

In writing this equation, we have defined the two lateral wave vectors

$$\mathbf{K}_\parallel = \mathbf{k}_\parallel + \mathbf{G}_\parallel \qquad \mathbf{K}'_\parallel = \mathbf{k}_\parallel + \mathbf{G}'_\parallel, \quad (115)$$

and summations over $\mathbf{G}_\parallel$ and $\mathbf{G}'_\parallel$ have been replaced by summations over $\mathbf{K}_\parallel$ and $\mathbf{K}'_\parallel$. Equating coefficients of delta functions on both sides of Eq. (114) gives

$$\sum_{\mathbf{K}'_\parallel} \frac{\widehat{I}\left(\alpha(K_\parallel) - \alpha_0(K'_\parallel)\middle|\mathbf{K}_\parallel - \mathbf{K}'_\parallel\right)}{\alpha(K_\parallel) - \alpha_0(K'_\parallel)} \mathbf{M}\left(\mathbf{K}_\parallel|\mathbf{K}'_\parallel\right) \mathbf{a}(\mathbf{K}'_\parallel)$$
$$= -\frac{\widehat{I}\left(\alpha(K_\parallel) + \alpha_0(k_\parallel)\middle|\mathbf{K}_\parallel - \mathbf{k}_\parallel\right)}{\alpha(K_\parallel) + \alpha_0(k_\parallel)} \mathbf{N}\left(\mathbf{K}_\parallel|\mathbf{k}_\parallel\right) \mathbf{E}_0(\mathbf{k}_\parallel). \quad (116)$$

Equation (116) implies a linear relation between $a_\alpha(\mathbf{K}'_\parallel)$ [$\alpha = p, s$] and $E_{0\beta}(\mathbf{k}_\parallel)$ [$\beta = p, s$] which we write as

$$a_\alpha\left(\mathbf{K}'_\parallel\right) = \sum_\beta R_{\alpha\beta}\left(\mathbf{K}'_\parallel\middle|\mathbf{k}_\parallel\right) E_{0\beta}\left(\mathbf{k}_\parallel\right). \quad (117)$$

Combining Eqs. (116) and (117) results in the final form of the *reduced Rayleigh equation* for a periodic surface in reflection that we write as

$$\sum_{\mathbf{K}'_\parallel} \frac{\widehat{I}\left(\alpha(K_\parallel) - \alpha_0(K'_\parallel)\middle|\mathbf{K}_\parallel - \mathbf{K}'_\parallel\right)}{\alpha(K_\parallel) - \alpha_0(K'_\parallel)} \mathbf{M}\left(\mathbf{K}_\parallel|\mathbf{K}'_\parallel\right) \mathbf{R}\left(\mathbf{K}'_\parallel\middle|\mathbf{k}_\parallel\right)$$
$$= -\frac{\widehat{I}\left(\alpha(K_\parallel) + \alpha_0(k_\parallel)\middle|\mathbf{K}_\parallel - \mathbf{k}_\parallel\right)}{\alpha(K_\parallel) + \alpha_0(k_\parallel)} \mathbf{N}\left(\mathbf{K}_\parallel|\mathbf{k}_\parallel\right), \quad (118)$$

where

$$\mathbf{R}\left(\mathbf{K}'_{\parallel}\middle|\mathbf{k}_{\parallel}\right) = \begin{bmatrix} R_{pp}(\mathbf{K}'_{\parallel}|\mathbf{k}_{\parallel}) & R_{ps}(\mathbf{K}'_{\parallel}|\mathbf{k}_{\parallel}) \\ R_{sp}(\mathbf{K}'_{\parallel}|\mathbf{k}_{\parallel}) & R_{ss}(\mathbf{K}'_{\parallel}|\mathbf{k}_{\parallel}) \end{bmatrix}. \tag{119}$$

The set of solutions of this equation $\{R_{\alpha\beta}(\mathbf{K}'_{\parallel}|\mathbf{k}_{\parallel})\}$ describes the reflection of incident light of polarization β and lateral wave vector $\mathbf{k}_{\parallel}$ that is scattered by the periodic surface $\zeta(\mathbf{x}_{\parallel})$ into reflected α-polarized light characterized by the lateral wave vector $\mathbf{K}'_{\parallel} = \mathbf{k}_{\parallel} + \mathbf{G}'_{\parallel}$.

6.1.1 The I-integral

In order to completely define the RRE for a periodic surface, Eq. (118), the $\widehat{I}$-integrals that appear in this equation have to be calculated. From the definitions of these integrals, Eq. (113), it should be apparent that to do so one is required to assume a specific form for the periodic surface profile function that we write as

$$\zeta(\mathbf{x}_{\parallel}) = \sum_{\ell} S\left(\mathbf{x}_{\parallel} - \mathbf{x}_{\parallel}(\ell)\right). \tag{120}$$

Here $S(\mathbf{x}_{\parallel})$ represents the part of the surface profile that is repeated inside each unit cell. In this work we will carry our numerical calculations assuming two forms of this function, both which are rotational symmetric about the x_3-axis, and these forms are depicted in Fig. 40.

The first form of $S(\mathbf{x}_{\parallel})$ that we will consider is the *truncated cone* of in-plane circular cross-section characterized by top and base radii ρ_t and ρ_b (see Fig. 40). Mathematically this function can be defined as

$$S(\mathbf{x}_{\parallel}) = \begin{cases} \zeta_0 & 0 \leq x_{\parallel} < \rho_t \\ \zeta_0 \frac{\rho_b - x_{\parallel}}{\rho_b - \rho_t} & \rho_t \leq x_{\parallel} < \rho_b \\ 0 & \rho_b \leq x_{\parallel} \end{cases}, \tag{121}$$

where $0 \leq \rho_t \leq \rho_b$, the amplitude $\zeta_0 \geq 0$ and $x_{\parallel} = |\mathbf{x}_{\parallel}|$.

Instead of calculating directly the $\widehat{I}$-integral associated with the truncated cone, we will start with a simpler calculation for which the surface profile function is a the circular pillar of height ζ_0 and radius ρ_0. The corresponding profile function is defined as a special case of a Eq. (121) obtained when $\rho_t = \rho_b = \rho_0$. In this case and with Eq. (113), a direct calculation leads to

$$\begin{aligned}\widehat{I}\left(\gamma|\mathbf{G}_{\parallel}\right) &= \frac{1}{a_c}\int_{a_c} d^2x_{\parallel}\ \left\{1+\exp\left[-i\gamma\zeta(\mathbf{x}_{\parallel})\right]-1\right\}\exp\left(-i\mathbf{G}_{\parallel}\cdot\mathbf{x}_{\parallel}\right)\\ &= \delta_{\mathbf{G}_{\parallel},\mathbf{0}}+\frac{1}{a_c}\int_0^{\rho_0} dx_{\parallel}\ x_{\parallel}\int_{-\pi}^{\pi} d\phi\ \left[\exp\left(-i\gamma\zeta_0\right)-1\right]\exp\left(-iG_{\parallel}x_{\parallel}\cos\phi\right)\\ &= \delta_{\mathbf{G}_{\parallel},\mathbf{0}}+\frac{2\pi}{a_c}\left[\exp\left(-i\gamma\zeta_0\right)-1\right]\int_0^{\rho_0} dx_{\parallel}\ x_{\parallel}J_0(G_{\parallel}x_{\parallel})\end{aligned} \tag{122}$$

where $\delta_{\mathbf{G}_{\parallel},\mathbf{0}}$ denotes a Kronecker delta function. In obtaining this result, a factor of one has been added and subtracted from the exponential function containing the surface profile function so that the function $\exp\left[-i\gamma\zeta(\mathbf{x}_{\parallel})\right]-1$ vanishes whenever the surface profile function $\zeta(\mathbf{x}_{\parallel})$ vanishes. Moreover, in arriving at Eq. (122) polar coordinates has been introduced and we have used that the Bessel function of the first kind and order zero has

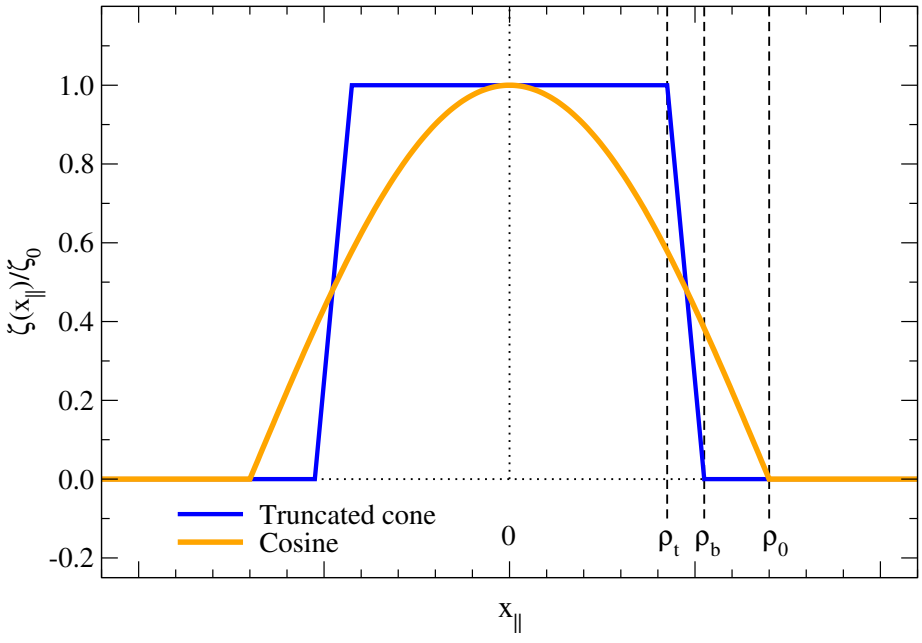

Figure 40: The truncated cone and cosine forms assumed for the surface profile in the modeling.

the integral representation (Olver *et al.*, 2010)

$$J_0(z) = \frac{1}{2\pi}\int_{-\pi}^{\pi} d\theta \ \exp\left(ix\cos\theta\right). \tag{123}$$

This function enters into the expressions for $\widehat{I}\left(\gamma|\mathbf{G}_{\parallel}\right)$ due to the rotational symmetry of the profile function $S(\mathbf{x}_{\parallel}) = S(x_{\parallel})$. The integral that appears in Eq. (122) can be evaluated analytically with the results that (Gradshteyn and Ryzhik, 2007)

$$\widehat{I}\left(\gamma|\mathbf{G}_{\parallel}\right) = \delta_{\mathbf{G}_{\parallel},\mathbf{0}} + 2\pi\frac{\rho_0^2}{a^2}\left[\exp\left(-i\gamma\zeta_0\right) - 1\right]\frac{J_1(G_{\parallel}\rho_0)}{G_{\parallel}\rho_0}, \tag{124}$$

where $J_1(\cdot)$ denotes the Bessel function of the first kind and order one and we have used that $a_c = a^2$ for a square lattice. We note that when $G_{\parallel}\rho_0 = 0$ in Eq. (124) then $J_1(G_{\parallel}\rho_0)/(G_{\parallel}\rho_0) = 1/2$.

We are now prepared to calculate the $\widehat{I}$-integral for the truncated cone; the procedure that we will follow mimics how the result in Eq. (124) was obtained. By introducing Eq. (121) into Eq. (113) and using Eq. (123) one obtains

$$\begin{aligned}
\widehat{I}\left(\gamma|\mathbf{G}_{\parallel}\right) &= \delta_{\mathbf{G}_{\parallel},\mathbf{0}} + \frac{2\pi}{a_c}\int_0^{\rho_b} dx_{\parallel}\ x_{\parallel}J_0(G_{\parallel}x_{\parallel})\left[\exp\left\{-i\gamma\zeta(x_{\parallel})\right\} - 1\right] \\
&= \delta_{\mathbf{G}_{\parallel},\mathbf{0}} + \frac{2\pi}{a^2}\left[\exp\left(-i\gamma\zeta_0\right) - 1\right]\int_0^{\rho_t} dx_{\parallel}\ x_{\parallel}J_0(G_{\parallel}x_{\parallel}) \\
&\quad + \frac{2\pi}{a^2}\int_{\rho_t}^{\rho_b} dx_{\parallel}\ x_{\parallel}J_0(G_{\parallel}x_{\parallel})\left[\exp\left(-i\gamma\zeta_0\frac{\rho_b - x_{\parallel}}{\rho_b - \rho_t}\right) - 1\right].
\end{aligned} \tag{125}$$

The two first terms on the right-hand-side of Eq. (125) are given by the right-hand-side of Eq. (124) if ρ_0 is replaced in this expression by ρ_t. To calculate the last integral of Eq. (125), we Taylor expand the exponential function that appears in the integrand and integrate the

resulting expression term-by-term to obtain

$$\widehat{I}\left(\gamma|\mathbf{G}_{\parallel}\right) = \delta_{\mathbf{G}_{\parallel},\mathbf{0}} + 2\pi\frac{\rho_t^2}{a^2}\left[\exp\left(-i\gamma\zeta_0\right) - 1\right]\frac{J_1(G_{\parallel}\rho_t)}{G_{\parallel}\rho_t} + \frac{2\pi}{a^2}\sum_{n=1}^{\infty}\frac{(-i\gamma\zeta_0)^n}{n!}\int_{\rho_t}^{\rho_b} dx_{\parallel}\; x_{\parallel}J_0(G_{\parallel}x_{\parallel})\left(\frac{\rho_b - x_{\parallel}}{\rho_b - \rho_t}\right)^n. \tag{126}$$

If now the change of variable

$$u_{\parallel} = \frac{\rho_b - x_{\parallel}}{\rho_b - \rho_t} \tag{127}$$

is made in the last term in Eq. (126) one obtains after some rewriting

$$\widehat{I}\left(\gamma|\mathbf{G}_{\parallel}\right) = \delta_{\mathbf{G}_{\parallel},\mathbf{0}} + 2\pi\frac{\rho_t^2}{a^2}\left[\exp\left(-i\gamma\zeta_0\right) - 1\right]\frac{J_1(G_{\parallel}\rho_t)}{G_{\parallel}\rho_t} + 2\pi\frac{\rho_b - \rho_t}{a^2}\sum_{n=1}^{\infty}\frac{(-i\gamma\zeta_0)^n}{n!}\int_{0}^{1} du_{\parallel}\;\left[\rho_b - (\rho_b - \rho_t)u_{\parallel}\right]\; J_0\left(G_{\parallel}\left[\rho_b - (\rho_b - \rho_t)u_{\parallel}\right]\right)u_{\parallel}^n. \tag{128}$$

The integrals that appear in this equation have to be evaluated numerically, and in most cases, only a few terms were needed in the sum to obtain convergent results. It is readily checked that the expression in Eq. (128) in the limit $\rho_t \to \rho_b$ reduces to that of Eq. (124), as it should.

The second form of the surface profile function for which we will perform calculations is the cosine surface profile (see Fig. 40) defined as

$$S(\mathbf{x}_{\parallel}) = \begin{cases} \zeta_0 \cos\left(\dfrac{\pi x_{\parallel}}{2\rho_0}\right) & 0 < x_{\parallel} < \rho_0 \\ 0 & x_{\parallel} > \rho_0 \end{cases}. \tag{129}$$

We now use this expression in Eq. (113) in order to obtain the corresponding expression

for the integral $\widehat{I}$. The result is

$$\begin{aligned}\widehat{I}\left(\gamma|\mathbf{G}_{\parallel}\right) &= \delta_{\mathbf{G}_{\parallel},\mathbf{0}} + \frac{1}{a_c}\int_0^{\rho_0} dx_{\parallel}\; x_{\parallel}\int_{-\pi}^{\pi} d\phi\;\left\{\exp\left[-i\gamma\zeta(x_{\parallel})\right]-1\right\}\exp\left(-iG_{\parallel}x_{\parallel}\cos\phi\right)\\ &= \delta_{\mathbf{G}_{\parallel},\mathbf{0}} + \frac{2\pi}{a^2}\int_0^{\rho_0} dx_{\parallel}\; x_{\parallel}J_0(G_{\parallel}x_{\parallel})\left\{\exp\left[-i\gamma\zeta(x_{\parallel})\right]-1\right\}\\ &= \delta_{\mathbf{G}_{\parallel},\mathbf{0}} + \frac{2\pi}{a^2}\sum_{n=1}^{\infty}\frac{(i\gamma)^n}{n!}\int_0^{\rho_0} dx_{\parallel}\; x_{\parallel}J_0(G_{\parallel}x_{\parallel})\,\zeta^n(x_{\parallel}),\end{aligned} \tag{130}$$

where Eq. (123) and a Taylor series expansion of $\exp\left[-i\gamma\zeta(x_{\parallel})\right]$ have been used in the first and last transmission, respectively. The integrals present in Eq. (130) have to be calculated numerically, and sufficiently many terms to reach were included to reach convergence.

6.1.2 Efficiencies of the diffracted Bragg beams

From the knowledge of the reflection amplitudes the diffraction efficiencies of the scattered beam can be calculated. They are measurable quantities and in this section we will derive expressions for them.

To this end, we start by calculating the power flux that is incident and scattered by the surface. The magnitude of the total time-averaged power flux incident on the surface is defined as

$$P_{\mathrm{inc}} = -\,\mathrm{Re}\int d^2x_{\parallel}\;\mathbf{S}^c_{\mathrm{inc}}\cdot\widehat{\mathbf{x}}_3, \tag{131}$$

where $\mathbf{S}^c_{\mathrm{inc}}$ denotes the complex Poynting's vector of the incident electromagnetic field. This vector is defined as $\mathbf{S}^c = (c/4\pi)\mathbf{E}\times\mathbf{H}^*$ where the asterisk means complex conjugate (Jackson, 2007). The minus sign that appears on the right-hand side of Eq. (131) compensates for the fact that the 3-component of the incident flux is negative. With the forms of the incident electric and magnetic fields from Eqs. (95a) and (97a) and the use of

the vector identity $\mathbf{a}\times(\mathbf{b}\times\mathbf{c}) = (\mathbf{a}\cdot\mathbf{c})\,\mathbf{b} - (\mathbf{a}\cdot\mathbf{b})\,\mathbf{c}$, it is readily demonstrated that

$$P_{inc} = \frac{c^2 A}{8\pi\omega}\alpha_0(k_\parallel)\left[\left|E_{0p}\left(\mathbf{k}_\parallel\right)\right|^2 + \left|E_{0s}\left(\mathbf{k}_\parallel\right)\right|^2\right], \tag{132}$$

where A denotes the area of the plane $x_3 = 0$ illuminated by the incident light.

Similarly, the magnitude of the total time-averaged scattered flux follows from

$$P_{\rm sc} = \mathrm{Re}\int d^2x_\parallel\, \mathbf{S}^c_{\rm sc}\cdot\widehat{\mathbf{x}}_3. \tag{133}$$

From the expressions for the scattered fields, Eqs. (95b) and (97b), one finds after what is a lengthy but straight forward calculation [see (Hetland *et al.*, 2016) for details]

$$P_{\rm sc} = \frac{c^2}{32\pi^3\omega}\int\limits_{q_\parallel<\omega/c} d^2q_\parallel\;\alpha_0(q_\parallel)\left[\left|A_p(\mathbf{q}_\parallel)\right|^2 + \left|A_s(\mathbf{q}_\parallel)\right|^2\right]. \tag{134}$$

The reason that the $q_\parallel$-integration that appears in this expression is limited to the domain $q_\parallel < \omega/c$ is a direct consequence of the real value that is taken in Eq. (133). When $q_\parallel > \omega/c$, we are evanescent in vacuum and $\alpha_0(q_\parallel)$ is purely imaginary. When this happens, the integrand in Eq. (134) is also purley imaginary and will therefore not contribute to $P_{\rm sc}$.

The periodicity of the surface profile function $\zeta(\mathbf{x}_\parallel)$ is taken into account via the relations in Eq. (108). From these expressions one obtains the relation

$$\begin{aligned}\left|A_\nu(\mathbf{q}_\parallel)\right|^2 &= \sum_{\mathbf{G}_\parallel}\left[(2\pi)^2\delta\left(\mathbf{q}_\parallel - \mathbf{k}_\parallel - \mathbf{G}_\parallel\right)\right]^2\left|a_\nu(\mathbf{k}_\parallel + \mathbf{G}_\parallel)\right|^2 \\ &= \sum_{\mathbf{G}_\parallel}(2\pi)^2\delta\left(\mathbf{0}\right)(2\pi)^2\delta\left(\mathbf{q}_\parallel - \mathbf{k}_\parallel - \mathbf{G}_\parallel\right)\left|a_\nu(\mathbf{k}_\parallel + \mathbf{G}_\parallel)\right|^2,\end{aligned} \tag{135}$$

which when combined with Eq. (134), gives

$$P_{\rm sc} = \frac{c^2 A}{8\pi\omega}\sum_{\mathbf{G}_\parallel}{}'\,\alpha_0(|\mathbf{k}_\parallel + \mathbf{G}_\parallel|)\left[\left|a_p(\mathbf{k}_\parallel + \mathbf{G}_\parallel)\right|^2 + \left|a_s(\mathbf{k}_\parallel + \mathbf{G}_\parallel)\right|^2\right]. \tag{136}$$

Here we have used a prime on the summation symbol to indicate that the sum over $\mathbf{G}_\parallel$ only runs over values for which $|\mathbf{k}_\parallel + \mathbf{G}_\parallel| < \omega/c$. Equation (136) demonstrates that each

diffracted beam contributes independently to the scattered flux.

When the incident field is β polarized [$\beta = p, s$], the incident power is

$$P_{\text{inc}}^{(\beta)} = \frac{c^2 A}{8\pi\omega}\alpha_0(k_\parallel)\left|E_{0\beta}(\mathbf{k}_\parallel)\right|^2 \qquad \beta = p, s \tag{137}$$

and, after using Eq. (117), the corresponding scattered power can be expressed in the form

$$P_{\text{sc}}^{(\beta)} = \frac{c^2 A}{8\pi\omega}\sum_{\mathbf{G}_\parallel}{}' \alpha_0(|\mathbf{k}_\parallel + \mathbf{G}_\parallel|)\sum_{\alpha=p,s}\left|R_{\alpha\beta}(\mathbf{k}_\parallel + \mathbf{G}_\parallel|\mathbf{k}_\parallel)\right|^2\left|E_{0\beta}(\mathbf{k}_\parallel)\right|^2. \tag{138}$$

When the scattered power is normalized by the power of the incident light $P_{\text{inc}}^{(\beta)}$ one gets

$$\frac{P_{\text{sc}}^{(\beta)}}{P_{\text{inc}}^{(\beta)}} = \sum_{\mathbf{G}_\parallel}{}' \sum_{\alpha=p,s} e_{\alpha\beta}\left(\mathbf{k}_\parallel + \mathbf{G}_\parallel|\mathbf{k}_\parallel\right), \tag{139}$$

where

$$e_{\alpha\beta}\left(\mathbf{k}_\parallel + \mathbf{G}_\parallel|\mathbf{k}_\parallel\right) = \frac{\alpha_0(|\mathbf{k}_\parallel + \mathbf{G}_\parallel|)}{\alpha_0(k_\parallel)}\left|R_{\alpha\beta}(\mathbf{k}_\parallel + \mathbf{G}_\parallel|\mathbf{k}_\parallel)\right|^2. \tag{140}$$

The quantity $e_{\alpha\beta}\left(\mathbf{k}_\parallel + \mathbf{G}_\parallel|\mathbf{k}_\parallel\right)$ is the *diffraction efficiency* of incident light of β polarization into the $\mathbf{G}_\parallel$th Bragg beam of α polarization. This quantity only has a physical meaning for those values of $\mathbf{G}_\parallel$ for which $|\mathbf{k}_\parallel + \mathbf{G}_\parallel| < \omega/c$; this situation is often referred to as *open diffraction channels*.

The reflectivity of the periodic structure is obtained from the diffraction efficiency when $\alpha = \beta$ and $\mathbf{G}_\parallel = \mathbf{0}$;

$$R_\alpha(\mathbf{k}_\parallel) = e_{\alpha\alpha}(\mathbf{k}_\parallel|\mathbf{k}_\parallel) \qquad \alpha = p, s. \tag{141}$$

6.1.3 Numerical solution of the RRE

A challenge faced when performing a direct numerical solution of the RRE for the scattering of light from two-dimensional surfaces is the numerical complexity. In this section we discuss the aspects worth mentioning.

In order to obtain a numerical solution of the RRE for a periodic surface profile function, Eq. (118), we start by restricting the indices h_1 and h_2 that appear in the wave vector $\mathbf{G}'_{\parallel}$ (see Eq. (105)) to the intervals $-H \leq h_i \leq H$, $(i = 1, 2)$, where H is a positive integer. This implies that the number of terms in the summation in Eq. (118) is reduced from an infinite number to a finite number. Therefore we only have a finite set of unknow scattering amplitudes $R_{\alpha\beta}\left(\mathbf{k}_{\parallel} + \mathbf{G}'_{\parallel} \mid \mathbf{k}_{\parallel}\right)$ to solve for. To numerically calculate these scattering amplitudes, the RRE (118) is converted into a linear system of equations. To this end, $R_{\alpha\beta}\left(\mathbf{k}_{\parallel} + \mathbf{G}'_{\parallel} \mid \mathbf{k}_{\parallel}\right)$ is mapped into a vector by adapting a certain storage convention for its elements that depends on both vector and polarization indices. It should be noticed that the value of the index β appearing in the scattering amplitudes is given by the polarization of the incident field. The scattering amplitudes for the two possible values of this index are obtain by solving the RRE under the assumption of an incident field of either p- or s-polarization, i.e. $\beta = p$ or $\beta = s$. From Eq. (118), one observes that the polarization of the incident field only enters on the right-hand-side of the RRE, so that the matrix on the left-hand-side remain unchanged by the change of the polarization of the incident field. With the storage convention assumed, the elements $\mathbf{M}(\mathbf{K}_{\parallel}|\mathbf{K}'_{\parallel})$ times the prefactor appearing in the RRE that depend on the two polarization indices and two wave vector indices, are mapped onto a matrix that forms the left-hand-side of the linear system. A detail account of this procedure is given in Apendix A. The linear system obtained in this way is then solved by standard routines from LAPACK (Anderson *et al.*, 1999; Barker *et al.*, 2001). The solution vector is then mapped back onto $R_{\alpha\beta}\left(\mathbf{k}_{\parallel} + \mathbf{G}'_{\parallel} \mid \mathbf{k}_{\parallel}\right)$, which are the quantities that we search, and from which physically observable like diffracted efficiencies can be calculated.

In order to obtain accurate simulation results, the value of H used in the calculations has to be sufficiently high so that the maximum wave number resolved in the simulations is well into the evanescent regime. For instance, for light of wavelength $\lambda = 1550$ nm (in

vacuum) incident on a square periodic structure characterized by a period of a = 450 nm the value H = 5 was used. It was found that increasing H above this value did not change the obtained results in any significant way.

A better way of evaluating the quality of the obtained results is to check that the simulations respect energy conservation when applided to a scattering system where none of the media involved have aborption. In order to be able to do that, one also needs to calculate the transmittance. This requires to solve the RRE for transmission, in addition to the corresponding equation for reflection given by (118). The transmission equation is simpler than the one for diffraction because the inhomogeneous term is simply proportional to a Kronecker symbol: there is no $\widehat{I}$ integral in it. The $\widehat{I}$ integral is the same as for the diffraction problem, and the **M** matrix elements are close to those arising in the diffraction problem. For the parameters used in this work, energy was conserved to within 0.03%.

6.2 The Fourier modal method

To model the reflectivity of the studied samples, we adapted the *Fourier modal method* (FMM) also known as the *rigorous coupled wave analysis* (RCWA) (Moharam *et al.*, 1995; Li, 1996; Liu and Fan, 2012). This (Fourier-space) simulation method assumes that the geometry is *periodic* and it is particularly well suited for the study of dielectric systems. It is also assumed that the geometry is piece wise invariant in the vertical direction (the x_3 direction); if this is not the case, a staircase approximation is adopted so that a curved geometry is divided into a set of layers each of which is uniform in the vertical direction (Fig. 41). The electromagnetic fields within each layer are expanded in Bloch waves

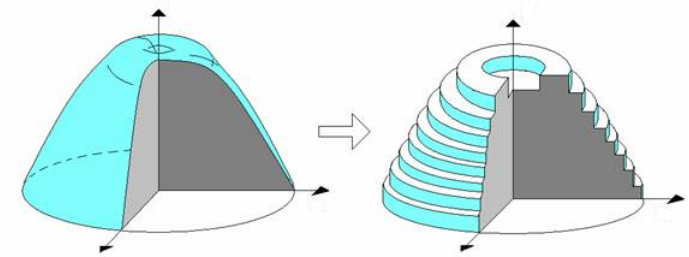

Figure 41: Schematic of the staircase approximation adopted in the FMM.

(Floquet functions) so that the desired periodicity of the fields is guaranteed. The full electromagnetic field is obtained by satisfying the boundary conditions at each of the interfaces between the layers. In this way the Maxwell's equations are converted into an infinitely large set of algebraic equations. To be able to solve it on the computer, this set is truncated at a large but finite Fourier order.

Coupled wave analysis was first used to study grating diffraction problems for holograms, mostly involving a sinusoidally varying dielectric function in a single layer. These core principles were summarized by Moharam and Gaylord (1995) detailing the original RCWA formulation, and subsequently reformulated into a numerically stable method. The extension to crossed gratings and general two-dimensionally periodic structures occurred later with improved computational power and numerical algorithms.

6.2.1 Derivation of the FMM

We will now present a general derivation of the FMM, for more details see (Liu and Fan, 2012). The starting point of the derivation is Maxwell's equations in time-harmonic form, assuming an $\exp(-i\omega t)$ time dependence:

$$\nabla \times \mathbf{H} = -i\omega\epsilon_0\epsilon\mathbf{E}, \tag{142a}$$

$$\nabla \times \mathbf{E} = -i\omega\mu_0\mathbf{H}. \tag{142b}$$

The next step is to take the spatial Fourier transform in the xy-plane. Because of the periodicity and separability of the z-axis the fields must have the form

$$\mathbf{H}(\mathbf{r},z) = \sum_{\mathbf{G}} \mathbf{H}_{\mathbf{G}}(z) \exp\left[i(\mathbf{k}+\mathbf{G})\cdot\mathbf{r}\right], \tag{143}$$

where $\mathbf{k}$ is the in-plane component of the k-vector set by the excitation, and $\mathbf{G}$ is a reciprocal lattice vector. A similar equation holds for $\mathbf{E}$.

After several assumptions, the Fourier transform of each field component can be ex-

pressed as

$$i\widehat{k}_y h_z(z) - h'_y(z) = -i\omega d_x(z) \tag{144a}$$

$$h'_x(z) - i\widehat{k}_x h_z(z) = -i\omega d_y(z) \tag{144b}$$

$$i\widehat{k}_x h_y(z) - i\widehat{k}_y h_x(z) = -i\omega\widehat{\epsilon}_z e_z(z) \tag{144c}$$

$$i\widehat{k}_y e_z(z) - e'_y(z) = i\omega h_x(z) \tag{144d}$$

$$e'_x(z) - i\widehat{k}_x e_z(z) = i\omega h_y(z) \tag{144e}$$

$$i\widehat{k}_x e_y(z) - i\widehat{k}_y e_x(z) = i\omega h_z(z) \tag{144f}$$

where the primes denote differentiation with respect to z, and $\widehat{k}_x$ is a diagonal matrix with entries $(k_x + G_{1x}, k_x + G_{2x}, ...)$ and analogously for $\widehat{k}_y$. The last two equations contain dx and d_y which are the Fourier coefficients of the displacement field **D**. We assume then that there exists a matrix ε such that

$$\begin{bmatrix} -d_y(z) \\ d_x(z) \end{bmatrix} = \varepsilon \begin{bmatrix} -e_y(z) \\ e_x(z) \end{bmatrix}. \tag{145}$$

Eliminating the z in Eqs.(144c),(144d) and (144e), they can be written in a matrix form as

$$\left(\omega^2 I - K\right) \begin{bmatrix} h_x(z) \\ h_y(z) \end{bmatrix} = -i\omega \begin{bmatrix} -e'_y(z) \\ e'_x(z) \end{bmatrix} \tag{146}$$

and

$$K = \begin{bmatrix} \widehat{k}_y\widehat{\epsilon}_z^{-1}\widehat{k}_y & -\widehat{k}_y\widehat{\epsilon}_z^{-1}\widehat{k}_x \\ -\widehat{k}_x\widehat{\epsilon}_z^{-1}\widehat{k}_y & \widehat{k}_x\widehat{\epsilon}_z^{-1}\widehat{k}_x \end{bmatrix} \tag{147}$$

where I is the identity matrix of the proper dimensions. Similarly, for Eqs.(144f), (144a) and (144b), we can write the matrix expression

$$\left(\omega^2\varepsilon - K\right) \begin{bmatrix} -e_y(z) \\ e_x(z) \end{bmatrix} = -i\omega \begin{bmatrix} -h'_x(z) \\ h'_y(z) \end{bmatrix} \tag{148}$$

and

$$K = \begin{bmatrix} \widehat{k}_x\widehat{k}_x & \widehat{k}_x\widehat{k}_y \\ \widehat{k}_y\widehat{k}_x & \widehat{k}_y\widehat{k}_y \end{bmatrix} \tag{149}$$

Therefore, the original Maxwell's equation are reduced to (146) and (148).

The basic idea behind the FMM is to expand the fields within a layer into eigenmodes which have a simple $\exp(iqz)$ dependence for some complex number q. We assume that the form of the magnetic field eigenmode is

$$\mathbf{H}(z) = \sum_{\mathbf{G}} \left[\phi_{\mathbf{G},x}\mathbf{x} + \phi_{\mathbf{G},y}\mathbf{y} - \frac{(k_x + G_x)\,\phi_{G,x} + \left(k_y + G_y\right)\phi_{G,y}}{q} \right] \exp\left[i\left(\mathbf{k} + \mathbf{G}\right)\cdot\mathbf{r} + iqz\right] \tag{150}$$

where **x**, **y**, and **z** are the Cartesian unit vectors and $\phi_{G,x}$ and $\phi_{G,y}$ are expansion coefficients that may be written as vectors in the form

$$\phi_x = \left[\phi_{G_1,x}, \phi_{G_2,x}, ...\right]^T \tag{151}$$

and analogously for ϕ_y. We then have

$$h(z) = \left[\phi_x\mathbf{x} + \phi_y\mathbf{y} - q^{-1}\left(\widehat{k}_x\phi_x + \widehat{k}_y\phi_y\right)\mathbf{z}\right]\exp(iqz) \tag{152}$$

where $h(z)$ is a column vector whose elements correspond to **G** vectors. Using these expressions in Eqs.(146) and (148), they become

$$\left(\omega^2 I - K\right)\begin{bmatrix}\phi_x \\ \phi_y\end{bmatrix} = \omega q \begin{bmatrix} -e_y \\ e_x \end{bmatrix} \tag{153}$$

and

$$\omega q \begin{bmatrix}\phi_x \\ \phi_y\end{bmatrix} = \left(\omega^2\varepsilon - K\right)\begin{bmatrix} -e_y \\ e_x \end{bmatrix} \tag{154}$$

where we have dropped the z dependence on e_x and e_y to represent a fixed mode with

$\exp(iqz)$ variation. Eliminating the electric field and using the fact that $KK = 0$,

$$\left(\varepsilon\left(\omega^2 - K\right) - K\right)\phi = \phi q^2, \tag{155a}$$

$$\phi = \begin{bmatrix} \phi_x \\ \phi_y \end{bmatrix}. \tag{155b}$$

where q^2 is the diagonal matrix whose diagonal elements are the eigenvalues q_n^2. The columns of the square matrix ϕ are $\left[\phi_{x,n}, \phi_{y,n}\right]^T$, the Fourier coefficients of the eigenmodes.

The solution of the eigenvalue equation forms the bulk of the computing time and is solved using LAPACK (Anderson *et al.*, 1999; Barker *et al.*, 2001). One can see directly that the size of the eigenvalue problem scales as N, the number of **G**. Thus the storage requirements for an entire simulation scale as $O\left(MN^2\right)$ where M is the number of layers.

After solving Eq. (155b), the transverse magnetic field in layer i may be represented as

$$\begin{bmatrix} h_x(z) \\ h_y(z) \end{bmatrix} = \sum_n \begin{bmatrix} \phi_{x,n} \\ \phi_{y,n} \end{bmatrix} \left(a_n \exp(iq_n z) + b_n \exp(iq_n(d_i - z))\right), \tag{156}$$

where n indexes the eigenmodes, a_n is the coefficient of a forward propagationg wave at $z = z_i$, and b_n is the coefficient of a backward propagating wave at $z = z_i + d_i$. For q there are two choices depending on the sign chosen, but for numerically stability $\operatorname{Im} q \geq 0$. Defining now a diagonal matrix operator $f(z)$ with entries

$$f(z)_{nn} = \exp(iq_n z). \tag{157}$$

We also define the transverse field component vectors in the Fourier basis as

$$h_t(z) = \left[h_x(z), h_y(z)\right]^T, \tag{158a}$$

$$e_t(z) = \left[-e_y(z), e_x(z)\right]^T, \tag{158b}$$

as well as mode amplitude vectors for forward and backward waves

$$a = [a_1, a_2, ...]^T , \tag{159a}$$

$$b = [b_1, b_2, ...]^T . \tag{159b}$$

Using these definitions, we can now relate the mode amplitudes to the physical fields by means of the expression

$$\begin{bmatrix} e_t(z) \\ h_t(z) \end{bmatrix} = \begin{bmatrix} \left(\omega^2 I - K\right)\phi q^{-1} & -\left(\omega^2 I - K\right)\phi q^{-1} \\ \phi & \phi \end{bmatrix} \times \begin{bmatrix} f(z)\, a \\ f(d-z)\, b \end{bmatrix} \tag{160}$$

The next stages of solution involve forming the layer matrix. For further details see (Liu and Fan, 2012).

6.2.2 Numerical implementation of the FMM

The FMM is a highly accurate method for calculating the reflectivity of a periodic structure. However, there are several reasons why it may lead to poor performance. First, FMM computations involve solving eigenvalue systems, which are computationally expensive to solve. Second, when many layers are used to discretize a given geometry, boundary conditions must be enforced at the interfaces between layers, resulting in a large linear system (van der Aa and Mattheij, 2007).

Also, being a Fourier-space method it suffers several drawbacks. The main one is its slow convergence compared to other methods like the RRE method presented here. In the presence of materials with a high dielectric contrast, the Gibbs phenomenon (Arfken and Weber, 2005) to which it gives rise is particularly severe. The same Gibbs phenomenon introduces ringing in the real space reconstruction of a function. The amplitude of the Gibbs ringing is a problem independent of the number of Fourier components.

In this work, we use the publicly available FMM code called S^4 (*Stanford Stratified Structure Solver*) (Liu and Fan, 2012), a frequency-domain computational electromagnetics tool that can compute reflection, transmission, or absorption spectra of periodic

structures composed of layers invariant in the direction normal to the periodicity. The electromagnetic fields throughout the structure can also be obtained. The S^4-package also provides a set of FMM formulations. This is beneficial since different formulations can have different convergence rates and therefore can produce better results in shorter amounts of computation time. Here we provide a summary of the various formulations of the FMM (Liu and Fan, 2012):

Closed: This corresponds to the earliest FMM formulations. This model works for problems in which the dielectric constant profile in each layer can be specified in a non-discretized way, by means of simple geometric shapes in which the dielectric constant is assumed constant.

FFT: Instead of using closed form Fourier transforms, in this model the dielectric constant is discretized onto a grid and the fast Fourier transform (FFT) is applied to approximate the Fourier series of epsilon.

Subpixel: This method computes an average of the dielectric function over a discretized unit cell, and then the FFT is used.

Vector-field-based formulations: Both, the Jones and the Pol formulations use a vector field that is generated on the discretized unit cell and uniformly scale so its maximum length is unity. These formulations achieve significantly faster convergence than the other methods, being the Pol method the one that shows slightly faster and more stable convergence behavior.

An important aspect of the S4 code is that among its implementations, a proper Fourier factorization is used to achieve better convergence compare to other formulations (Liu and Fan, 2012). Its use has being widely reported in the literature and validated against published FMM results, and to results obtained by other simulation methods.

Chapter 7 EMT in silicon photonics

In this Chapter, we present and discuss the numerical results obtained with the methods of calculation described in Chapt. 6, and contrast them with the experimental results for the reflectivity of our samples, and with the results based on EMTs. For this, we have considered the classical approaches of Maxwell Garnett (1904) and Bruggeman (1935) in their 3D and 2D versions.

In the calculations we considered two circularly symmetric profile forms for the supported silicon pillars. The first one consists of *truncated cones* characterized by their top and base radii ρ_t and ρ_b (see Fig. 40), and defined mathematically by Eq. (121). The model is simple and fairly realistic, as attested by the electron microscope images presented in Fig. 34. The values used in the calculations for the base and top radii were the experimentally determined ones, namely, ρ_t = 85 nm and ρ_b = 105 nm. For the pillar heights ζ_0 achieved experimentally the surface slopes can be quite large, and this poses a problem for the method based on the Rayleigh hypothesis.

To circumvent this problem in the calculations based on the RRE, we considered profiles in the form of a *cosine*, defined mathematically in Eq. (129). The base radius of the cosine profile was chosen in such a way that, for the same height, its volume is the same as that of the truncated cone. With our experimental parameters, this resulted in a value of ρ_0 = 140 nm. It is important to point out that, although a cosine does not represent a good fit to the experimental shape of the pillars, the adoption of this shape does not change the volume fraction of the inclusions in the structured region and permits calculations based on the RRE with larger height values.

Figure 42 presents FMM calculated results for the reflectivity $R(\zeta_0)$ (solid lines) of the truncated cones as a function of their height ζ_0 obtained using the S^4-software package (Liu and Fan, 2012). The period of the square lattice was a = 450 nm, and we assumed normally incident illumination with linearly polarized light of wavelength λ = 1550 nm. At this wavelength the dielectric constant of silicon is ϵ = 12.25. In obtaining these results N = 600 in-plane Fourier components were retained in the calculations (the number of reciprocal lattice vectors inside a circular domain), and the height of the truncated cones,

ζ_0, was divided into L = 10 layers of equal thickness. It was found that increasing N and L above these values did not result in any noticeable change in the simulation results; at least, this was the case for the geometrical parameters that we considered. The radius of the disc approximating the cone inside each layer was taken as the cone's radius at the center-height of the layer.

It is observed from Fig. 42, where we present the reflectivity as function of the height of the truncated cones or cosine shaped silicon particles supported by a planar silicon substrate, that the FMM calculated reflectivity values agree rather well with the reflectivity values measured for Sample A and B (red filled circles). Moreover, as we have already mentioned, the values of the geometrical parameters assumed in performing the FMM calculations are in good agreement with the values of the corresponding geometrical parameters obtained by analyzing the SEM images of the same samples (Figs. 34 and 35).

It is recalled that Sample A is periodic, which is what is assumed in FMM calculations, while Sample B is random but with the same (surface) density of nanopillars as Sample A. The fact that the results of the FMM calculations also agree well for Sample B is considered as an indication that it is the density of pillars that is the key parameter in determining

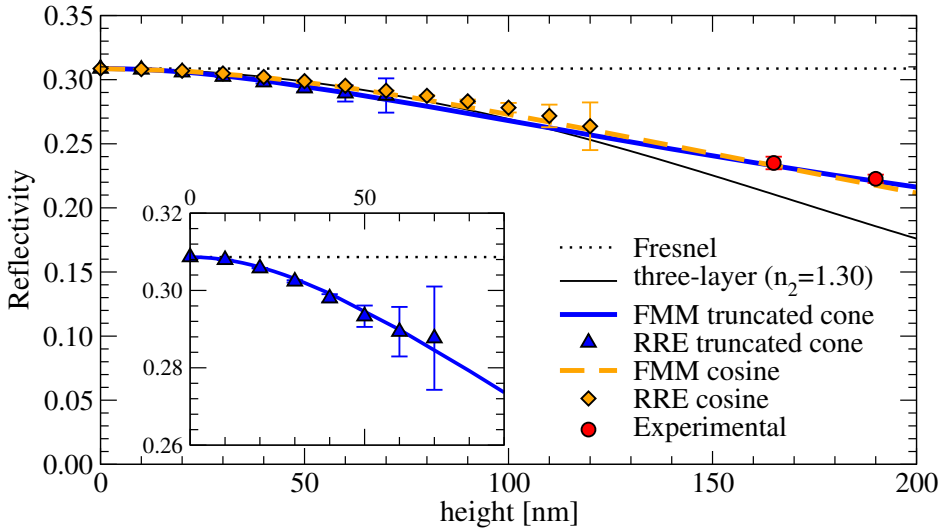

Figure 42: The reflectivity $R(\zeta_0)$ as function of the height ζ_0 of the truncated cones or cosine shaped silicon particles supported by a planar silicon substrate. The horizontal dotted lines indicate the Fresnel reflectivity of the corresponding planar silicon surface. The thin solid black line represents the reflectivity of a three-layer model, Eq. (94), that fits the RRE (and FMM) simulation results in the low-height limit. The layer assumed in this model was characterized by the thickness ζ_0 and refractive index n_2 = 1.30.

the reflectivity of the sample and not the periodicity; at least, this is the case for for the wavelength that was used in the measurements and calculations. It is speculated that this agreement will no longer hold true when the wavelength is reduced so that more than one diffraction channel is open.

For the FMM calculations reported in Fig. 42, we used the formulation termed $\mathrm{PolarizationBasis}$ (or "Pol") in Ref. (Liu and Fan, 2012). This formulation is original to the code S^4, and it gave the fastest convergence, at least, for the geometrical parameters that we assumed. Some of the other FMM formulations available in S^4 (and other FMM software packages) converged more slowly; this we attribute to the high value of the dielectric constant of silicon (ϵ = 12.25) (Liu and Fan, 2012).

An inspection of the SEM images of the structures (Fig. 34) seems to reveal that the cross section of the structures are elliptical instead of having the circular shape assumed in performing the above calculations. An elliptical cross section will lead to a difference in the reflectivity for an electric field oriented along the long or short axis of the ellipse even at normal incidence. To investigate what effect this elongated shape will have on the reflectivity, we took the two semi-axes of the base to be $(1.00 \pm 0.05)\rho_b$, and similarly for the top semi-axis $(1.00 \pm 0.05)\rho_t$. With these values the reflectivity of unpolarized light at normal incidence departed only a few percent from what was obtained for the reflectivity of the corresponding truncated cones of a circular cross section defined by the radii ρ_b and ρ_t (and the same height ζ_0).

The FMM calculations presented in Fig. 42 are computationally intensive. It is therefore of interest to explore alternative computational approaches and we will here use the RRE approach introduced in Chapt. 6 In the first set of RRE calculations the truncated cones assumed in the FMM calculations were considered. The results of such calculations are presented in Fig. 42 as filled blue triangles. Here the error bars indicate $\pm|1 - R_\alpha - T_\alpha|$ where T_α denotes the transmissivity for incident light of polarization α [see Soubret et al., (2001); Hetland et al., (2016)]. From Fig. 42 it is observed that the results of the FMM and RRE calculations agree rather well. However, from the inset to Fig. 42 it is apparent that the RRE results for the truncated cones of height $\zeta_0 > 60\,\mathrm{nm}$ can not be trusted due to the lack of energy conservation. It is speculated that the poorer convergence property

seen for the RRE approach when applied to the truncated cone is due to the steep slopes and the sharp corners around the top radius ρ_t (Banon and Simonsen, 2016). Therefore, the next set of calculations were performed with the RRE approach for pillars of a cosine form characterized by a base radius ρ_0 = 140 nm. As we have mentioned, this radius was chosen so that the volumes of the cosine particles and the truncate cones are the same for structures of the same height. The reflectivity values calculated by the RRE method for the cosine profile are presented in Fig. 42 as filled orange diamonds. For comparison we also performed calculations of the reflectivity by the FMM for the same profile, and the results were found to agree well with what was obtained by the RRE approach (dashed orange line in Fig. 42). Such good agreement hints towards the correctness of the obtained results. The deviation between the RRE and FMM calculated reflectivities for a cosine form is less than two percent at height ζ_0 = 100 nm.

The reflectivity values obtained by the FMM and RRE approaches are observed to be slightly larger for the cosine form than those obtained for the truncated cones of the same volume. The fact that the reflectivity values are so similar for the two particle forms we take as an indication that the particle volume is one of the critical parameters for determining the reflectivity of the surface.

It should be mentioned that the computational time required to produce the the FMM and RRE simulation results presented in Fig. 42 are rather different. For instance to check for convergence, we performed FMM calculations with N = 1000 which took several days on a modern desktop computer when it was run in sequential mode. Reflectivity calculations for the same particle form using the RRE approach required only a few seconds on the same computer. Even if this latter approach is not able to handle the largest pillar heights, it is still useful due to its much better computational performance.

On the basis of the low-height RRE simulation results for the cosine form presented in Fig. 42 the three-layer model of thickness ζ_0 was fitted for the refractive index n_2 of the layer. In this way we obtained the effective refractive index n_2 = 1.30 for the layer. The corresponding dependence of the reflectivity with the height ζ_0 of the layer that is predicted by Eq. (94) is presented in Fig. 42 as a thin black line. These results demonstrate that a three-layer model of a fixed value of n_2 is inadequate to accurately describe the

reflectivity variations predicted by the solution of the RRE and the FMM. The three-layer model reflectivity drops off too fast and for larger heights of the pillars the discrepancy is significant.

Figure 43 presents the results for $R(\zeta_0)$ calculated from the Maxwell Garnett (blue lines) and Bruggeman effective medium theories (orange lines). These results are summarized in Table 1. Note that the since the truncated cone and the cosine bump both have the same volume, the filling fractions are the same for both particle forms. Therefore, the EMT reflectivities are identical for these two particle forms. The filled/open symbols in this figure represent the 2D/3D versions of there EMTs. It is observed from Fig. 43 that all the reflectivities obtained from the EMTs are significantly higher then those obtained from FMM (or RRE) simulations or the values measured for Samples A and B. The 2D versions of the considered EMTs produce results that are the closest to the simulation results, and the 2D Bruggeman result is better than the results obtained on the basis of the 2D Maxwell Garnett EMT (for the 3D EMTs it is the opposite). Even if the numerical values predicted by the EMTs depart substantially from the measured (and simulated) values, it is still noted that the slopes of the reflectivity curves $R(\zeta_0)$ are more realistic for the EMTs than for the three-layer model.

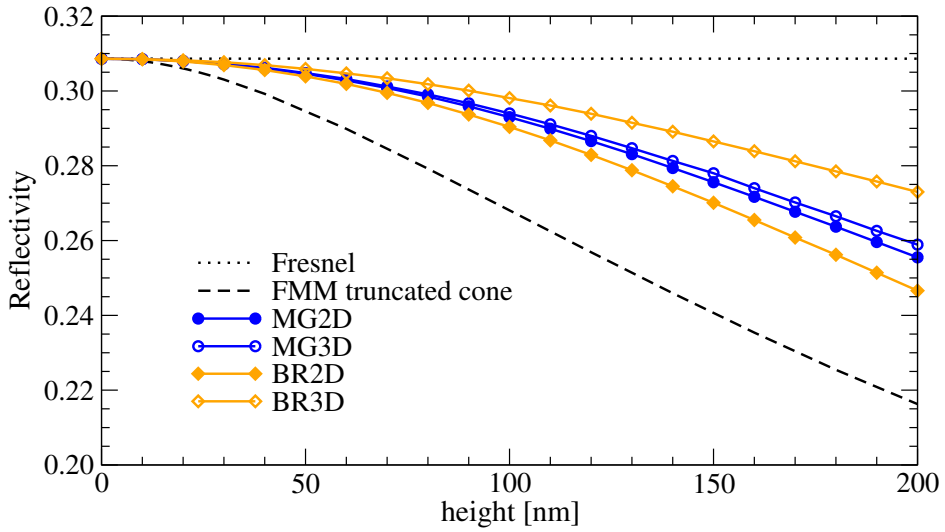

Figure 43: The same as Fig. 42 but now the 2D and 3D Maxwell Garnett (MG) and Bruggeman (BR) effective medium theories are used to calculate the reflectivity at normal incidence for pillars of a given height. For comparison the FMM calculated and Fresnel reflectivities are given.

Table 1: Summary of the calculated reflectivities by means of EMTs for the nanostructured silicon samples.

Sample	Experimental	MG 2D	MG 3D	BR 2D	BR 3D
Periodic	0.2227 ± 0.0032	0.2596	0.2626	0.2514	0.2758
Non-periodic	0.2350 ± 0.0049	0.2717	0.2721	0.2631	0.2825

On the basis of the results presented in Fig. 43 and Table 1 it is concluded that both the (2D and 3D) Maxwell Garnett and Bruggeman EMTs fail to predict accurately the reflectivity of the silicon system under study. The reason that the EMTs fail to predict the reflectivity we speculate is due to the high value of the dielectric constant of silicon.

To test this idea, we have carried out the same kind of calculations but with glass, rather than silicon. The results are presented in Fig. 44 In this case, the pillars and the substrate are made from glass (ϵ = 2.25). We observe that the 2D Maxwell Garnett and 2D Bruggeman EMTs produce virtually identical reflectivity values; they only deviate from the FMM calculated reflectivity by 0.5%, or less, over the entire interval $0 \leq \zeta_0 \leq 200\,\text{nm}$ of pillar heights.

From the results presented in this Chapter we see that our attempts to reproduce the experimental measurements of the reflectivity using simple EMTs and a three-layer model

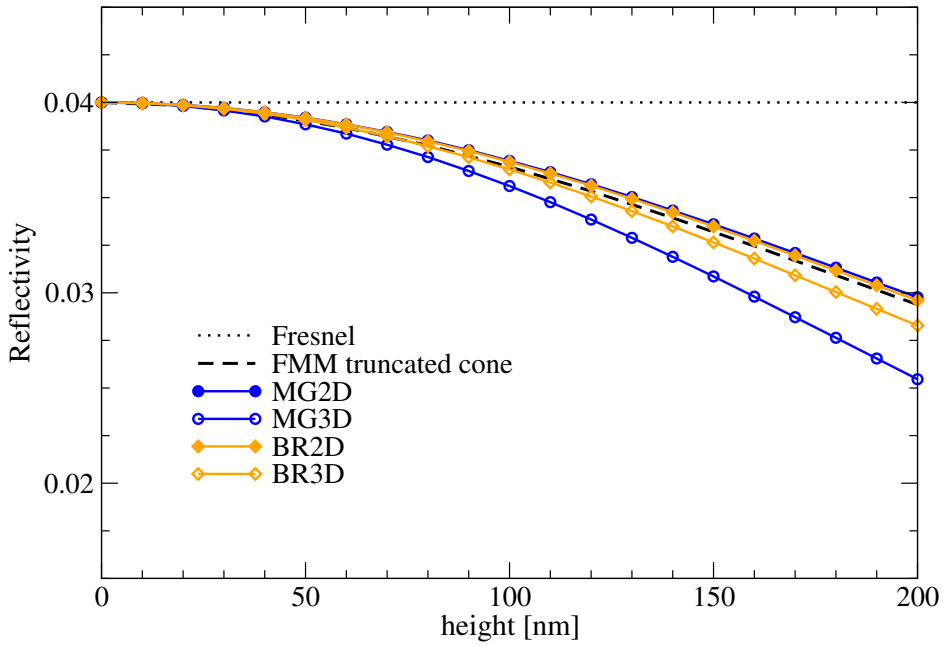

Figure 44: The same as Fig. 43 but now for glass.

have failed. The rigorous results based on the FMM for the reflectivity as a function of pillar height indicate that it is not possible to model the problem as a three-media system, and that the structured layer needs to be modeled as an inhomogeneous layer.

Chapter 8 Conclusions

In this chapter, we present an overview of the work carried out in this thesis. We discuss, in comparative terms the results obtained with the experimental and numerical approaches, in addition to the main conclusions drawn from those results.

We have presented a literature review of works in which transformation optics concepts are employed in silicon photonics. The central idea is to design structures in which the spatially dependent refractive index is controlled through the density of silicon nano-pillars. On such a basis, we have presented the design of an expander/compressor to couple light from a monomode glass waveguide into a high index silicon waveguide.

We have also tested the accuracy of effective medium theories (EMTs) in silicon structures at telecommunication wavelengths. To fabricate these samples at the University of Technology of Troyes, we have explored a technique that has not been used for this purpose before. Several tests were carried out in order to gain expertise in the fabrication method. With this technique, by selectively etching silicon wafers we fabricated structured surfaces that consisted of sub wavelength silicon pillars with a truncated-cone shape, on an otherwise flat silicon substrate.

Using effective medium concepts, we have tried to model the structured region of our samples as a flat homogeneous layer over a flat silicon substrate. However, our attempts to reproduce the experimental measurements of the reflectivity using simple EMTs and this three-layer model have failed. The EMTs we have considered are the 2D (cylindrical inclusions) and 3D (spherical inclusions) versions of the Maxwell Garnett theory, as well as the Bruggeman approach.

Given the failure of the EMTs to model the physical situation, we have carried out more rigorous numerical calculations based on the Fourier modal method (FMM) and the reduced Rayleigh equation (RRE). The former is often employed to model periodic structures in nanophotonics, and the simulations with this method were performed using a publicly available code. The latter approach is typically employed in rough surface scattering problems, and to perform the simulations with this method, we used a specially developed code.

The two numerical approaches produce results that are in good agreement with each other and with the experimental results. The FMM is computationally intensive, while the Rayleigh method is faster but cannot deal with surfaces that have large slopes. Although with this approach we were unable to reach the pillar heights of our samples, the method can be useful when the concept of a homogeneous layer is valid, as in that case the effective refractive index of the layer does not depend on the height of the pillars.

The rigorous results based on the FMM for the reflectivity as a function of pillar height indicate that it is not possible to model the problem as a three-media system, and that the structured layer needs to be modeled as an inhomogeneous layer.

We believe that the failure of the EMTs and the three-layer media model to describe adequately the physical situation is due to the large dielectric contrast between silicon and air. This idea is supported by the good numerical agreement between experiment and theory we have found for similar structures made in glass, rather than silicon.

List of references

Anderson, E., Bai, Z., Bischof, C., Blackford, S., Demmel, J., Dongarra, J., Du Croz, J., Greenbaum, A., Hammerling, S., McKenney, A., *et al.* (1999). *LAPACK Users' Guide: Third Edition*. Software, Environments, and Tools. Society for Industrial and Applied Mathematics.

Arfken, G. B. and Weber, H. J. (2005). Mathematical methods for physicists. **6**: 910–914.

Aubry, A., Lei, D. Y., Fernandez-Dominguez, A. I., Sonnefraud, Y., Maier, S. A., and Pendry, J. B. (2010). Plasmonic light-harvesting devices over the whole visible spectrum. *Nano Lett.*, **10**(7): 2574–2579.

Banon, J.-P. and Simonsen, I. (2016). Notes on fmm. *unpublished*.

Baoquan, S., Mingwang, S., and Shuitong, L. (2016). Nanostructured silicon used for flexible and mobile electricity generation. *Advanced Materials*, **28**(47): 10539—-10547.

Barker, V., Blackford, L., Dongarra, J., Du Croz, J., Hammarling, S., Marinova, M., Waniewski, J., and Yalamov, P. (2001). *LAPACK95 Users' Guide*. Software, Environments, and Tools. Society for Industrial and Applied Mathematics.

Bergman, D. J. (1978). The dielectric constant of a composite material - a problem in classical physics. *Phys. Rep.*, **43**(9): 377–407.

Born, M. and Wolf, E. (1970). Principles of optics. **4**.

Brown, G., Celli, V., Coopersmith, M., and Haller, M. (1983). Unitary and reciprocal expansions in the theory of light scattering from a grating. *Surface Science*, **129**(2): 507 – 515.

Brown, G., Celli, V., Haller, M., and Marvin, A. (1984). Vector theory of light scattering from a rough surface: Unitary and re ciprocal expansions. *Surf. Sci.*, **136**(2): 381 – 397.

Bruggeman, D. A. G. (1935). Dielektrizitatskonstanten und leitfahigkeiten der mishkorper aus isotropen substanzen. *Ann. Phys.*, **416**(7): 636–664.

Choy, T. C. (1999). Effective medium theory: Principles and applications. pp. 181–187.

Delacour, C., Blaize, S., Grosse, P., Fedeli, J.M. amd Bruyant, A., Salas-Montiel, R., Lerondel, G., and Chelnokov, A. (2010). Efficient directional coupling between silicon and copper plasmonic nanoslot waveguides: toward metal-oxide-silicon nanophotonics. *Nano Lett.*, **10**(8): 2922—-2926.

Depine, R. A. and Simón, J. M. (1982). Diffraction grating efficiencies: Conformal mapping method for a good real conductor. *Opt. Acta*, **29**(11): 1459–1473.

Etrich, C., Fahr, S., Hedayati, M. K., Faupel, F., Elbahri, M., and Rockstuhl, C. (2014). Effective optical properties of plasmonic nanocomposites. *Materials*, **7**(2): 727–741.

Fang, Z. and Zhao, C. (2012). Recent progress in silicon photonics: A review. *ISRN Optics*, **2012**: 428690.

Floyd, R. and Steinberg, L. (1976). An adaptive algorithm for spatial grayscale. *Proceedings for the Society for Information Display*, **17**: 75–77.

Gabrielli, L. H. and Lipson, M. (2011). Transformation optics on a silicon platform. *J. Opt.*, **13**(2): 024010.

Gabrielli, L. H., Cardenas, J., Poitras, C. B., and Lipson, M. (2009). Silicon nanostructure cloak operating at optical frequencies. *Nature photonics Letters*, **10**(1038): 461–463.

García-Meca, C., Tung, M. M., Galán, J. V., Ortuño, R., Rodríguez-Fortuño, F. G., Martí, J., and Martínez, A. (2011). Squeezing and expanding light without reflections via transformation optics. *Optics Express*, **19**(4): 3562.

Glass, N. E., Maradudin, A. A., and Celli, V. (1983). Theory of surface-polariton resonances and field enhancements in light scattering from bigratings. *J. Opt. Soc. Am.*, **73**(10): 1240–1248.

Gradshteyn, I. S. and Ryzhik, I. M. (2007). *Tables of Integrals, Series, and Products*. Academic Press. Burlington, MA.

Griesmann, U. (2013). Gds ii for the rest of us. *Public Domain Tutorial for the MATLAB/Octave Toolbox for GDS II Libraries*, pp. 1–16.

Heine, G. W. I. (2004). The prehistory of conformal mapping. *Proceedings of the 2004 ESRI User Conference*.

Hetland, O. S., Maradudin, A. A., Nordam, T., Letnes, P. A., and Simonsen, I. (2016). Numerical studies of the transmission of light through a two-dimensional randomly rough interface. *unpublished*.

Hill, N. R. and Celli, V. (1978). Limits of convergence of the rayleigh method for surface scattering. *Phys. Rev. B*, **17**: 2478–2481.

Huang, Y., Miroshnichenko, A. E., and Gao, L. (2016). Low-threshold optical bistability of graphene-wrapped dielectric composite. *Scientific Reports*, **6**: 23354.

Jackson, J. (2007). *Classical Electrodynamics*. John Wiley & Sons, tercera edición. New York.

Jaffer, A. (2015). The freesnell thin-film optical simulator. *Free Software*, **1c2**.

Kirchner, A., Busch, K., and Soukoulis, C. M. (1998). Transport properties of random arrays of dielectric cylinders. *Phys. Rev. B*, **57**(1): 277–288.

Kong, J. (2005). *Electromagnetic Wave Theory*. EMW Publishing.

Lalanne, P. and Lemercier-Lalanne, D. (1997). Depth dependence of the effective properties of subwavelength gratings. *J. Opt. Soc. Am. A*, **14**(2): 450–458.

Lenz, G., Talanina, I., and Sterke, C. M. (1999). Bloch oscillations in an array of curved optical waveguides. *Physical Review Letters*, **83**(5): 963–969.

Leonhardt, U. (2006). Optical conformal mapping. *Science*, **312**(5781): 1777–1780.

Leonhardt, U. and Philbin, T. (2010). Geometry and light: The science of invisibility. pp. 70–148.

Leonhardt, U. and Philbin, T. G. (2009). Transformation optics and the geometry of light. *Progress in Optics.*, pp. 69—-152.

Li, J. and Pendry, J. B. (2008). Hiding under the carpet: a new strategy for cloaking. *Phys. Rev. Lett.*, **101**(20): 203901.

Li, L. (1996). Use of fourier series in the analysis of discontinuous periodic structures. *J. Opt. Soc. Am. A*, **13**(9): 1870–1876.

Liu, V. and Fan, S. (2012). S4: A free electromagnetic solver for layered periodic structures. *Comput. Phys. Commun.*, **183**(10): 2233–2244.

Lorentz, H. (2011). *The Theory of Electrons*. John Wiley & Sons, segunda edición. New York.

Luo Y., Aubry A., P. J. B. (2011). Electromagnetic contribution to surface enhanced raman scattering from rough metal surfaces: A transformation optics approach. *Physical Review B*, **83**(15): 155422.

Maradudin, A. A. (2007). Light scattering and nanoscale surface roughness. (1): 93–105.

Marte, M. A. M. and Stenholm, S. (1997). Paraxial light and atom optics: The optical schrodinger equation and beyond. *Physical Review A*, **56**(4): 2940–2953.

Maxwell Garnett, J. C. (1904). Colours in metal glasses and in metallic films. *Philosophical Transactions of the Royal Society of London, Ser. A*, **203**(488–496): 385–420.

Meinke, H., Lange, K., and Ruger, J. (1963). Te and tm waves in waveguides of very general cross section. *Procc. IEEE*, **51**(11): 1436–1443.

Millar, R. (1969). On the rayleigh assumption in scattering by a periodic surface,. *Proc. Camb. Philos. Soc.*, **65**: 773–791.

Millar, R. F. (1971). On the Rayleigh assumption in scattering by a periodic surface. ii. *Math. Proc. Cambridge*, **69**: 217–225.

Moharam, M. G., Grann, E. B., Pommet, D. A., and Gaylord, T. K. (1995). Formulation for stable and efficient implementation of the rigorous coupled-wave analysis of binary gratings. *J. Opt. Soc. Am. A*, **12**(5): 1068–1076.

Nakamura, T., Shimizu, M., Kimura, H., and Sato, R. (2004). Effective permittivity of amorphous mixed materials. *Electronics and Communications in Japan*, **88**(10): 1951—-1958.

Neviere, M., Cerutti-Maori, G., and Cadilhac, M. (1971). Sur une nouvelle médiffraction d'une on de plane par un réseau infiniment conducteur. *Opt. Commun.*, **3**(1): 48–52.

Nevière, M., Cadilhac, M., and Petit, R. (1973). Applications of conformal mappings to the diffraction of electromagnetic waves by a grating. *IEEE Trans. Antennas Propag.*, **21**(1): 37–46.

Niklasson, G. A., Granqvist, C. G., and Hunderi, O. (1981). Effective medium models for the optical properties of inhomogeneous materials. *Applied Optics*, **20**(1): 27–30.

Nordam, T., Letnes, P., and Simonsen, I. (2013). Numerical simulations of scattering of light from two-dimensional surfaces using the reduced rayleigh equation. *Front. Phys.*, **1**: 8.

Nordam, T., Letnes, P. A., Simonsen, I., and Maradudin, A. A. (2014). Numerical solutions of the rayleigh equations for the scattering of light from a two-dimensional randomly rough perfectly conducting surface. *J. Opt. Soc. Am. A*, **31**(11): 1126–1134.

Olver, F. W. J., Lozier, D. W., Boisvert, R. F., and Clark, C. W., (eds.) (2010). *NIST Handbook of Mathematical Functions*. Cambridge University Press. New York, NY, USA. This book reprsesents a complete revision of Abramowitz and Stegun's Handbook of Mathematical Functions with Formulas, Graphs, and Mathematical Tables, published in 1964.

Pavesi, L., Gaburro, Z., Dal Negro, L., Bettotti, P., Vijaya Prakash, G., Cazzanelli, M., and Oton, C. (2003). Nanostructured silicon as a photonic material. *Optics and Lasers in Engineering*, **39**(3): 345—-368.

Pendry, J., Schurig, D., and Smith, D. (2006). Controlling electromagnetic fields. *Science*, **312**(5781): 1780–1782.

Porter, R. M. (2005). History and recent developments in techniques for numerical conformal mapping. *Proceedings of IWQCMA*, pp. 207–238.

Rahm, M., Schurig, D., Roberts, D., Cummer, S., Smith, D., and Pendry, J. (2008). Design of electromagnetic cloaks and concentrators using form-invariant coordinate transformations of maxwell's equations. *Photon. Nanostr.*, **6**(87): 87–95.

Rayleigh, L. (1907). On the dynamical theory of gratings. *Proc. R. Soc. Lon. Ser. A*, **79**: 399—-416.

Renault, M., Hadjar, Y., Blaize, S., Bruyant, A., Arnaud, L., Lerondel, G., and Royer, P. (2010). Bidimensional near-field sampling spectrometry. *Optics Letters*, **35**(19): 3303–3306.

Russell, P. S. J. (1985). Optics of floquet-bloch waves in dielectric gratings. *Applied Physics B*, **39**(4): 231—-246.

Sadeghi, M., Li, S., Xu, L., Hou, B., and Chen, H. Y. (2015). Transformation optics with fabry-pérot resonances. *Sci. Rep.*, **5**: 8680.

Schinzinger, R. and Laura, P. A. A. (2003). Conformal mapping methods and applications. pp. 266–269.

Schurig, D., Mock, J., Justice, B., Cummer, S., Pendry, J., Starr, A., and Smith, D. (2006). Metamaterial electromagnetic cloak at microwave frequencies. *Science*, **314**(5801): 977–980.

Simonsen, I. (2010). Optics of surface disordered systems: A random walk through rough surface scattering phenomena. *Eur. Phys. J. Special Topics*, **181**: 1.

Soubret, A., Berginc, G., and Bourrely, C. (2001). Application of reduced rayleigh equations to electromagnetic wave scattering by two-dimensional randomly rough surfaces. *Phys. Rev. B*, **63**(24): 245411.

Spadoti, D. H., Gabrielli, L. H., Poitras, C. B., and Lipson, M. (2010). Focusing light in a curved-space. *Optics Express*, **18**(3): 3181.

Takakura, Y. (1995). Rigorous integral approach to the problem of scattering from a modulated periodic medium obtained through conformal mapping. *J. Opt. Soc. Am. A*, **12**(6): 1283–1289.

van der Aa, N. P. and Mattheij, R. M. (2007). Computing shape parameter sensitivity of the field of one-dimensional surface-relief gratings by using an analytical approach based on rcwa. *J. Opt. Soc. Am. A*, **24**(9): 2692–2700.

Wolfang, T. (1993). The use of effective medium theories in optical spectroscopy. *Advances in Solid State Physics (Book series)*, **33**: 149–176.

Wu, Y., Li, J., Zhang, Z. Q., and Chan, C. T. (2006). Effective medium theory for magnetodielectric composites: Beyond the long-wavelength limit. *Phys. Rev. B*, **74**(8): 085111.

Xiaofei, X., Yijun, F., Yu, H., Juming, Z., and Tian, J. (2009). Infrared carpet cloak designed with uniform silicon grating structure. *Applied Physics Lett.*, **95**(18): 4248.

Zhang, D. (2007). Inverse electromagnetic problem for microstructured media.

Zhang, X. and Wu, Y. (2015). Effective medium theory for anisotropic metamaterials. *Scientific Reports*, **5**: 7892.